

REPORT DOCUMENTATION PAGE			Form Approved OMB No. 0704-0188	
<small>Public reporting burden for this collection of information is estimated to average 1 hour per response, including the time for reviewing instructions, searching existing data sources, gathering and maintaining the data needed, and completing and reviewing the collection of information. Send comments regarding this burden estimate or any other aspect of this collection of information, including suggestions for reducing this burden, to Washington Headquarters Services, Directorate for Information Operations and Reports, 1215 Jefferson Davis Highway, Suite 1204, Arlington, VA 22202-4302, and to the Office of Management and Budget, Paperwork Reduction Project (0704-0188), Washington, DC 20503.</small>				
1. AGENCY USE ONLY (Leave blank)		2. REPORT DATE		3. REPORT TYPE AND DATES COVERED
				Final 15 Jan 95 to 31 May 98
4. TITLE AND SUBTITLE Performance Enhancement in Optical Computing			5. FUNDING NUMBERS 61102F 2305/DS	
6. AUTHOR(S) Dr Walkup				
7. PERFORMING ORGANIZATION NAME(S) AND ADDRESS(ES) Texas Tech University P O Box 4439 Lubbock TX 79409-4439			8. PERFORMING ORGANIZATION REPORT NUMBER	
9. SPONSORING/MONITORING AGENCY NAME(S) AND ADDRESS(ES) AFOSR/NE 110 Duncan Ave RMB115 Bolling AFB DC 20332-8050			10. SPONSORING/MONITORING AGENCY REPORT NUMBER F49620-95-1-0140	
11. SUPPLEMENTARY NOTES				
12a. DISTRIBUTION/AVAILABILITY STATEMENT APPROVAL FOR PUBLIC RELEASE: DISTRIBUTION UNLIMITED			12b. DISTRIBUTION CODE	
13. ABSTRACT (Maximum 200 words) The major objectives of this research effort were (1) to develop mult-level, multi-error-correcting codes suitable for both the binary and non-binary operation of optical matrix-vector multipliers, including efficient decoding techniques, and (2) to investigate accuracy issues associated with optical memory technologies, including photon echoes, and multiplexed holography.				
14. SUBJECT TERMS			15. NUMBER OF PAGES	
			16. PRICE CODE	
17. SECURITY CLASSIFICATION OF REPORT UNCLASSIFIED		18. SECURITY CLASSIFICATION OF THIS PAGE UNCLASSIFIED	19. SECURITY CLASSIFICATION OF ABSTRACT UNCLASSIFIED	20. LIMITATION OF ABSTRACT UL

NSN 7540-01-280-5500

Standard Form 298 (Rev. 7-89)
Prescribed by ANSI Std. Z39-18

19980630 042

0506

Performance Enhancement in Optical Computing

Final Technical Report

on

AFOSR Grant F49620-95-1-0140

Co-Principal Investigators: John F. Walkup and Thomas F. Krile

Submitted to

AFOSR/NE
110 Duncan Ave., Suite B115
Bolling AFB, DC 20332-0001
Attn: Dr. Alan E. Craig

by the

Optical Systems Laboratory
Department of Electrical Engineering
Texas Tech University
Lubbock, TX 79409-3102

Period Covered: January 15, 1995 to May 31, 1998

Date Submitted: June, 1998

Introduction:

This is the final technical report on AFOSR Grant F49620-95-1-0140 (January 15, 1995 through May 31, 1998, \$418,671). There was a companion AASERT Grant F49620-95-1-0402 (June 1, 1995 through May 31, 1998, \$116,936) entitled "Noise Characterization of Devices for Optical Computing" under the direction of the same Co-Principal Investigators plus Dr. David J. Mehrl. The final report on the AASERT grant is being submitted separately.

Objectives:

The major objectives of this research effort were (1) to develop multi-level, multi-error-correcting codes suitable for both the binary and non-binary operation of optical matrix-vector multipliers, including efficient decoding techniques, and (2) to investigate accuracy issues associated with optical memory technologies, including photon echoes, and multiplexed holography. Another objective in the original proposal, to investigate the noise characteristics of advanced optical sources, spatial light modulators, and other devices which are candidates for application in optical computers, was shifted to the companion AASERT Grant, F49620-95-1-0402, "Noise Characterization of Devices for Optical Computing," running from June 1, 1995 to May 31, 1998.

Summary of Effort:

We achieved significant results in two areas: (1) multiple error correction codes for optical matrix-vector multipliers and (2) analytical, computer, and experimental investigations on noise modelling for photon echo memories. In the latter work we collaborated closely with Dr. Ravinder Kachru's group at SRI

International. This collaboration resulted in both noise modelling and analytical calculations by Ph.D. candidate Jin Y. Choi, and experimental investigations, at SRI International, undertaken by Mr. Choi and by Dr. X.A. Shen of SRI. The results of this work and the earlier work on error coding for OMVM's have been submitted for publication. Two papers related to the photon echo memory noise modelling project are included in the Appendix to this report. Also attached is a reprint related to research on the technology of multiplexed holographic storage in Bacteriorhodopsin supported by NASA Ames Research Center and performed by Dr. Arkady S. Bablumian, a Research Associate in our group. Dr. Bablumian is an expert on holographic storage techniques, particularly as they relate to optical security issues.

Details of Accomplishments/New Findings:

See the following summary, written by Dr. J.Y. Choi, for an overview of the accomplishments on the photon echo noise modelling project. We have reported earlier on our results relating to multiple error correction codes for use in optical matrix-vector multipliers. Preprints of papers relating to both projects are presented in the appendix to this report.

Overview: Noise Effects in Photon Echo Memories

A photon echo memory¹, also known as Time Domain Optical Storage (TDOS)², offers the potential of ultrahigh storage density and ultrahigh data throughput rates³. A photon echo memory stores information in the spectral domain of an inhomogeneously broadened absorbing material in addition to

the spatial addresses used in conventional two-dimensional optical memories. In a photon echo memory, the temporal Fourier transform of the input data sequence from a light source emitting at a fixed frequency is written into the inhomogeneous absorption profile. To store and to recall the input data faithfully, the bandwidth of the input data sequence must, therefore, be narrower than the inhomogeneous bandwidth. This requirement on the Fourier transform of the input data sequence sets an upper limit for the TDOS read-write data rate that essentially equals the inhomogeneous bandwidth of the material.

In reality, however, the data storage density and data transfer rates are further limited by the several kinds of imperfections in the storing and recovering processes. For example, the laser, which is used as the light source for a photon echo process, has imperfections like the fluctuations in the spectral linewidth and intensity, and these provide a noise background which results in degradation of the recovered signal. Also, in the photon echo process, we have assumed that the atom population and the inhomogeneous absorption profile are constant over the entire spectral range. Real materials, however, have a variation in local environments due to strains, impurities, dislocations, and other imperfections. In these physically realizable situations the atom population at each frequency will fluctuate, and this fluctuation will result in noise in the recovered signal. Finally, the noise generated by the detector is unavoidable.

During the period of this grant, we have investigated the noise characteristics of a photon echo memory system⁴. We divided the noise sources into three groups. One is the noise which is generated by equipment imperfections or current technology limitations. One of the most important noise sources in the photon echo memory is the frequency drift of lasers combined

with the bandwidth limitations of the system. If the bandwidth of the system is infinite, then even with frequency drift in the laser, the output will be an exact copy of the original signal. For an infinite bandwidth, however, the write/read pulses must be delta functions which is impossible in a real experimental situation. Therefore, researchers employ several techniques to broaden bandwidth as much as possible with limited laser power. For example, a frequency chirping technique may be applied to the write/read pulses to broaden their bandwidth. Our analysis⁵ showed that when write/read pulses with frequency chirping were used, the system behaves like an ideal bandpass filter. We know that other techniques (e.g. phase modulation, data encoding, etc.) also introduce bandwidth limitations into the system. These bandwidth limitations distort the output of the system. When a laser frequency drift also exists, the output becomes even more distorted. According to the analysis⁶, the frequency drift, combined with the bandpass filter effect generates three peaks for each kind of data ("0" and "1") in the integrated intensity. Furthermore, these peak values depend on the amount of frequency drift of the laser and the system bandwidth.

In practice, the integrated intensity of the output is not an observable quantity, because in reality what we can see is the detector output and this output is at least contaminated by shot noise. Therefore, we can't always observe the distribution of the integrated intensity directly. Analysis of the shot noise shows that when the output signal is weak, detector output is smoothed by the shot noise. In this case we cannot see any resemblance between the integrated intensity and the detector output. When the output echo is strong enough to ignore the shot noise effect, then we can see the resemblance

between the integrated intensity and the detector output. That makes sense because we know that if the signal is strong, then the output becomes free from shot noise influence. Therefore, we can observe the distribution of the integrated intensity indirectly at the detector output if the signal is large enough that we can ignore the effects of shot noise.

Thermal noise is another important factor in the measurement of weak signals in the photon echo memory system. As we know, thermal noise is Gaussian distributed, and the effect of thermal noise is to make the overall noise characteristics Gaussian. That is, if thermal noise is dominant, then the output noise is also Gaussian distributed regardless of the characteristics of the shot noise. It means that if the thermal noise becomes dominant, the distribution of the data also tends to be Gaussian. Our analysis showed that even when the output signal is large (i.e., when the shot noise does not affect the output distribution), if the thermal noise is strong, then the combined noise has a Gaussian distribution for both data "0" and data "1" cases. On the other hand, if the thermal noise is weaker than the shot noise, the combined noise possesses shot noise characteristics. Generally, the shot noise PDF is close in shape to a Poisson distribution for data "0" and to a Gaussian distribution for data "1". Therefore, if we measure the output characteristics, we can estimate which noise is the dominant noise in the system.

Atom fluctuations⁷, which we refer to here as frequency domain noise, are not significant in the real experimental environment because other noise sources (like laser frequency drift, shot noise, thermal noise, etc.) are much more dominant than the noise caused by atom fluctuations. One might ask why we analyze it? Because, like shot noise and thermal noise, it is also an

unavoidable noise source in the photon echo memory in the absence of a perfect crystal. Of course, perfect crystal do not exist, and real crystals have a distribution of local environments due to strains, impurities, dislocations, and other imperfections. Consequently, the number of atoms at each frequency in the material will be different and will follow a statistical distribution. This random distribution affects the echo output from the photon echo memory system and we performed our analysis to determine its effect on the echo output.

For our analysis, we first needed to know the characteristics of the atom fluctuations. However, analyzing the characteristics of the atom fluctuations is not easy and, until now (as far as we know), no one has ever analyzed its characteristics. We analyzed the cases where the distributions of the atom fluctuation were Gaussian, uniform and Poisson distributed. We also considered whether the noise is signal-independent and signal-dependent. The noise characteristics are also dependent on the properties of the write/read and data pulse combinations. We divided each case into three situations: (1) the write and read pulses are delta functions; (2) the write pulse is a non-delta function but the read pulse is a delta function; and (3) the write and read pulses are both non-delta functions. Because there is a Fourier transform relationship between the atom fluctuations and the output signal, we first needed to know the relationship between the probability density function (PDF) of the atom fluctuation and the PDF of the output signal in time. We derived the relationship between these two PDFs analytically and also performed computer simulations. Based on this relationship, we derived the PDF and the mean and variance of the output instantaneous intensity for each special case.

To find the shot noise effect, we needed to know the PDF of the integrated intensity. The integrated intensity is the integral of the instantaneous intensity over the pulse time interval. As a numerical approach, we used a simulation method to find the relationship between the instantaneous power and the integrated power depending upon pulse width for each model. What we did in the simulation is as follows: (1) based on the PDF of the instantaneous power, we generated the random instantaneous power; (2) we integrated the instantaneous power using pulse width; (3) we found the PDF of the integrated intensity. The thermal noise was added after the recovered signal went through the detector. Since the shot noise is generated at the detector, we can think of the thermal noise as being added to the shot noise. Therefore, modeling the shot noise and thermal noise together as a sum of two random process, we can find the PDF of the output signal from the PDF of two random noises by convolving their individual density functions. From the shot noise analysis, we found the PDF of the shot noise, and since the thermal noise was assumed to be Gaussian distributed, we were able to find the PDF of the echo output quite easily. What we need to know for convolution is the thermal noise characteristics, that is mean and variance of the thermal noise. The mean is generally assumed as zero, so what we don't know is the variance of the thermal noise. We assumed several variances for the thermal noise. By finding the output noise characteristics for each variance, we showed how thermal noise impacts the output noise characteristics for each case.

The bit error rate analysis⁵ for the bandwidth showed that the BER decreases rapidly when we increase the bandwidth from $1/t$ to $4/t$, where t is the data pulse width, however, increasing the bandwidth beyond that does not give

much benefit in terms of bit error rate. Therefore, in terms of the bit error rate, we conclude that a bandwidth of $4/t$ is sufficient for accurate echo signal recovery. The analysis for the frequency drift⁶ showed that the frequency drift affects the BER greatly when the system bandwidth is comparable to the data pulse bandwidth. However, when the system bandwidth is much bigger than the data pulse bandwidth, the frequency drift is not a important factor in terms of bit error rate. The analysis also showed that when we increase the echo efficiency, the means for both data cases increase exactly at the same rate, but the standard deviations increase more slowly. That means that if we have a high echo efficiency system, we can obtain an improved system performance over the low echo efficiency system in terms of the bit error rate.

References

1. T. W. Mossberg, " Time-domain frequency-selective optical data storage", Optics Letters, Vol.7, No. 2, 1982, 77-79.
2. W. E. Moerner, Persistent Spectral Hole-Burning: Science and Applications, Springer-Verlag, 1988.
3. Y. S. Bai, and R. Kachru, " Coherent time-domain data storage with a spread spectrum generated by random biphase shifting", ", Optics Letters, Vol.18, No. 14, 1993, 1189-1191.
4. J. Y. Choi, Noise Modeling of a Photon Echo Memory (Ph. D. dissertation, Texas Tech University, 1997).
5. J. Y. Choi, J. F. Walkup, T. F. Krile, and D. J. Mehrl, "Relationship between bandwidth and bit error rate for a photon echo memory with chirped write/read pulses", Submitted to Applied Optics, 1998.
6. J. Y. Choi, J. F. Walkup, T. F. Krile, and D. J. Mehrl, " Relationship of laser frequency drift to bit error rate for a photon echo memory", Submitted to Applied Optics, 1998.

7. W. E. Moerner and T. P. Carter, "Statistical fine structure of inhomogeneously broadened absorption lines," Physical review letters, Vol. 59, No.23, 1987, 2705-2708.

Personnel supported during the grant:

1. Faculty:

Dr. J.F. Walkup, Co-Principal Investigator, P.W. Horn Professor

Dr. T.F. Krile, Co-Principal Investigator, Professor

Dr. D.J. Mehrl, Co-Investigator, Associate Professor

2. Research Associates and Graduate Students:

Dr. Arkady S. Bablumian, Research Associate

Tankut Caglar, MS student

Jin-Youb Choi, Ph.D. student

Note: S. Mark Storrs, a Ph.D. candidate (graduation expected August, 1998) and U.S. citizen, was supported by the companion AASERT grant.

3. Secretary:

E. Gonzales

Publications:

Journal Publications:

Papers Published:

S.A. Ellett, T.F. Krile and J.F. Walkup, "Throughput Analysis of Digital Partitioning with Error-Correcting Codes for Optical Matrix-Vector Processors," Appl.Opt. **34**, 6744-6751(1995).

M. Storrs, D.J. Mehrl and J.F. Walkup, "Programmable spatial filtering with Bacteriorhodopsin," Appl. Optics, **35**, 4362-4636 (1995).

Papers in Press

D.A. Timucin, J.F. Walkup and T.F. Krile, "Accuracy in Analog Optical Processors: Statistical Modeling (in press for J.Opt. Soc. Am. A).

Papers Submitted

A.T. Caglar, T.F. Krile and J.F. Walkup, "Multiple Error-correction Coding for Optical Matrix-vector Multipliers," submitted to Applied Optics-Information Processing, August, 1997 (currently under revision).

J.Y. Choi, X.A. Shen, J.F. Walkup and T.F. Krile, "The relationship between bandwidth and bit error rate for a photon echo memory with chirped write/read pulses," submitted to Applied Optics-Information Processing, January, 1998.

J.Y. Choi, J.F. Walkup, T.F. Krile and D.J. Mehrl, "Relationship of laser frequency drift to bit error rate for a photon echo memory,"(submitted to Appl.Optics-Information Processing, April, 1998).

A.S. Bablumian, T.F. Krile, D.J. Mehrl and J.F. Walkup, "M-type Thick Holograms in Bacteriorhodopsin Films with a High-Divergence Reference Beam," Appl.Optics-IP, 37, 1350-1355 (1998) (related research supported by NASA Ames grant).

Paper in Preparation(to be submitted to J. Opt. Soc. Am. A in 1998 based on research completed under AFOSR Grant 91-0192):

"Accuracy in analog optical processors: limitations and enhancement" (D.A. Timucin, J.F. Walkup and T.F. Krile).

Interactions/Transitions:

Conferences/Seminars/Briefings

1. Presented invited colloquium entitled "Performance Enhancement in Optical Computing", Penn State University, State College, PA, September, 1995 (J.F. Walkup).
2. Participated in Phoenix, AZ Workshop(March 27-28, 1996) on Data-Encoding for Page-Oriented Optical Memories (Drs. Walkup, Krile, and graduate student Jin Choi). Dogan Timucin (NASA Ames) presented a paper based on previous Texas Tech AFOSR-funded work relating to statistical models for optical 3-plane processors.
3. Attended SPIE Aerosense '96, Orlando, FL, and presented paper entitled "Holographic data storage in bacteriorhodopsin using phase-encoded multiplexing and spectrum spreading techniques", April, 1996 (T.F. Krile and J.Y. Choi).
4. Attended SPIE Aerosense '96. Orlando, FL, and presented paper entitled "Application of Multiple Error Correcting Binary BCH Codes to Optical Matrix-Vector Multipliers" (T.F. Krile).

5. Attended SPIE Annual Meeting, Denver, CO and presented paper entitled "Multiport Model of a Liquid Crystal Light Valve", August, 1996 (J.F. Walkup and M. Storrs).
6. Participated in panel discussion on Future Directions for Optical Signal Processing and Computing, SPIE Annual Meeting, Denver, CO, August, 1996 (J.F. Walkup).
7. Presented paper entitled "Noise Modeling of a Photon Echo Memory in the Frequency Domain" at the 1996 LEOS meeting in Boston, MA, Nov. 1996 (Jin Choi).
8. Presented poster paper entitled "Laser Noise Analysis for a Photon Echo Memory" at 1997 Gordon Research Conference on Optical Information Processing and Holography in Meriden, NH, June, 1997 (J.F. Walkup).
9. Attended 1997 SPIE Technical Symposium, San Diego, July 1997 (T.F. Krile and J.F. Walkup). J.F. Walkup chaired session, received SPIE Fellow award.
10. Presented paper "Hologram Multiplexing in Bacteriorhodopsin," OSA Annual Meeting, Long Beach, CA, October 1997 (A.S. Bablumian, T.F. Krile, D.J. Mehrl, J.F. Walkup).
11. Presented paper "Noise Characteristics of a Photon Echo Memory," OSA Annual Meeting, Long Beach, CA, October 1997 (J.Y. Choi, J.F. Walkup, T.F. Krile, and D.J. Mehrl).
12. Presented paper "Applications of Bacteriorhodopsin for Optical Data Storage and Processing," (invited), LEOS '97, San Francisco, CA, November 1997 (A. S. Bablumian, D.J. Mehrl, T.F. Krile, J.F. Walkup).
13. Plan to present paper "Holographic Multiplexing in a Multilayer Recording Medium", SPIE Vol. 3468, SPIE Annual Meeting, San Diego, CA, July, 1998 (A.S. Bablumian, T.F. Krile, D.J. Mehrl and J.F. Walkup).
14. Plan to present paper "Bit Error Rates for a Photon-echo Memory," SPIE Vol. 3468, SPIE Annual Meeting, San Diego, CA, July, 1998 (J.Y. Choi, J.F. Walkup, T.F. Krile and D.J. Mehrl).
15. Plan to present paper " Holographic Properties of Bacteriorhodopsin ", OSA Annual Meeting, Baltimore, MD, Oct. 1998 (A.S. Bablumian, J.F. Walkup, T.F. Krile and D.J. Mehrl).

Lab Visits and Other Interaction:

1. Patent awarded: "Optical Pattern Recognition System and Method for Verifying the Authenticity of a Person, Product, or Thing," (US Patent No. 5,485,312; Jan. 16, 1996; J.L. Horner, B. Javidi and J.F. Walkup).

2. Lab visits (by Dr. R. Kachru to Texas Tech and Dr. J.F. Walkup to SRI) to establish a working relationship with SRI International researchers working on systems analysis/optimization of photon echo memories.
3. Interacted with Drs. Charles Gary, John Downie and Dogan Timucin(Texas Tech Ph.D., 1995) of NASA Ames, and Dr. Dan Smithey of Bend Research on holographic data storage in Bacteriorhodopsin films (Drs. Walkup, David Mehrl, Ph.D. candidate Jin Choi and Research Associate Dr. Arkady Bablumian).
4. Visited SRI International and participated in experiments designed to characterize laser noise processes associated with photon echo data storage, March, 1997, June-July, 1997 (Jin Choi). Preprint of paper resulting from experiments in Appendix.

Transitions

Dr. X.A. Shen and Dr. Ravinder Kachru from SRI International worked with us to optimize the systems aspects of photon echo memories. We suggested experiments which were performed at SRI for the purpose of modelling the noise properties of photon echo memories. Dr. Dan Smithey from Bend Research interacted with us for the purpose of improving BR films for holographic data storage. We also interacted with Drs Charles Gary, John Downie and Dogan Timucin at NASA Ames Research Center to share data on BR recording techniques. We have also interacted with Dr. Henryk Temkin from Texas Tech on measurements of the noise characteristics of optical devices. In summary we have had a significant number of researchers interested in our research projects under the AFOSR grant and the companion AASERT grant.

New Discoveries, Inventions or Patents: No inventions or patents during this funding period on material directly related to this project.

Honors/Awards:

John F. Walkup: Fellow of IEEE , OSA and SPIE, P.W. Horn Professor of Electrical Engineering at Texas Tech University.

Thomas F. Krile: Fellow of Optical Soc. of America.

In addition, Drs. Walkup, Krile, and Mehrl have each won a significant number of research and teaching awards at Texas Tech University.

APPENDIX

(Selected reprints and preprints)

1. A.T. Caglar et al., "Multiple error-correction coding for optical matrix-vector multipliers," submitted to Applied Optics-Information Processing, August, 1997.
2. J.Y. Choi et al., "The relationship between bandwidth and bit error rate for a photon echo memory with chirped write/read pulses," submitted to Applied Optics-Information Processing, January, 1998.
3. J.Y. Choi et al., "Relationship of laser frequency drift to bit error rate for a photon echo memory", submitted to Applied Optics-Information Processing, April, 1998.
4. J.Y. Choi et al., "Bit error rates for a photon echo memory," SPIE Proceedings, vol. 3468, paper to be presented at SPIE Annual Meeting, San Diego, CA, July, 1998.
5. A.S. Bablumian et al., "M-type thick holograms in bacteriorhodopsin films with a high-divergence reference beam," Applied Optics-Information Processing, 37, 1350-1355 (1998).

Multiple error-correction coding for optical matrix-vector multipliers

A. Tankut Çağlar, Thomas F. Krile, and John F. Walkup

Abstract

Application of multiple-error-correction codes to optical matrix-vector multipliers (OMVM's) can improve the accuracy of these processors. Two different error-correcting codes are examined; binary, multiple-error-correcting Bose-Chaudhuri-Hocquemghen (BCH) codes and non-binary, multiple-error-correcting Reed-Solomon codes. The advantages and disadvantages of using binary BCH codes versus non-binary Reed-Solomon codes are investigated. Based on the results obtained from the simulations, the conditions under which the use of error-correction coding is feasible in optical matrix-vector multipliers are discussed.

Key words: Optical computing, error-correcting codes, accuracy enhancement

1. Introduction

An optical matrix-vector multiplier (OMVM) is one specific type of optical linear algebra processor (OLAP) that is capable of performing matrix-vector multiplications.¹ During matrix-vector operations, vast amounts of data are manipulated in these processors; consequently, even a small amount of error may cause a large inaccuracy in the end result. When the low accuracy level of OLAPs is also considered, it becomes important to apply some type of error detection/correction technique to optical processors

in order to increase their reliability. A number of researchers^{2,3,4,5} have investigated the application of error detection/correction codes, normally used for information transmission and data storage, to various types of optical computational systems, including OMVMs.

Single-error-correction codes have been previously applied to these structures by Ellett et al. and results demonstrating the improvement gained in the process have been summarized in several related papers.^{6,7,8} Little effort, however, has been spent on the application of multiple-error-correcting codes to these multipliers⁹. Single-error-correcting codes improved the performance of these structures to some extent and multiple-error-correction techniques hold the promise of providing even more improvement. An overview of the model used for applying error coding to noisy computational systems is given in Section 2.

In a previous paper, the application of binary, multiple-error-correcting BCH codes to modulo-2 OMVM's was investigated.⁹ A two-error-correcting (15,7) BCH code was applied, and the results obtained were then compared to the three-error-correcting (15,5) binary BCH code. Simulations were performed both for signal-independent and signal-dependent noise in either the matrix A or the vector x of the computation $y = Ax$. Also the limitations in applying this code were pointed out in order to build the background necessary for choosing a new, improved code. Summary results of that paper will be shown in Section 3 for comparison purposes.

In this paper, the error-correction code applied to modulo-m OMVMs is the non-binary multiple-error-correcting Reed-Solomon (RS) code. Reed-Solomon codes are shown to correct more errors for a fixed message and code word length than the binary

BCH codes. This enhancement is purchased at the cost of the non-binary arithmetic involved in the encoding and decoding algorithms. However, these operations can be easily implemented with various electronic structures. In this case again, two different RS codes were simulated; the first being a four-error-correcting (15,7) RS code and the second being a five-error-correcting (15,5) RS code. The lengths of the code word vector and the message vector were chosen to be the same as those used for the BCH codes in order to be able to make a better and more appropriate comparison between them. The improvement that these codes supplied is presented with detailed discussions and figures in Section 4.

2. Error-Correction In Optical Matrix-Vector Multipliers

Application of error-correction codes to optical linear algebra processors is one technique proposed to overcome the low level of accuracy from which these architectures suffer, and to increase their reliability. Optical matrix-vector multipliers, which are a subclass of optical linear algebra processors, are usually designed to perform the following matrix-vector multiplication:

$$\mathbf{y} = \mathbf{Ax} \tag{1}$$

where \mathbf{y} is an $m \times 1$ vector, \mathbf{A} is an $m \times n$ matrix and \mathbf{x} is an $n \times 1$ vector. In order to apply error-correction to this multiplication, the above equation must be encoded so as to obtain a new, coded \mathbf{y} vector which is dimensionally larger than the original result of this multiplication. The redundancy added to the \mathbf{y} vector will help us to correct errors in the result, if any occur.

In order to understand the encoding process better we will proceed in reverse order through the algorithm. If we wanted to directly encode the resultant \mathbf{y} vector without dealing with the multiplication process, we would use the generator matrix approach, as described in the following equation

$$\mathbf{y}^c = \mathbf{G}\mathbf{y} \quad (2)$$

where \mathbf{y}^c represents the encoded vector and \mathbf{G} is the generator matrix associated with the code. If we make the substitution in Equation (1) for \mathbf{y} , we get

$$\mathbf{y}^c = \mathbf{G}\mathbf{y} = \mathbf{G}\mathbf{A}\mathbf{x} = \mathbf{A}^c\mathbf{x} \quad (3)$$

where \mathbf{A}^c is the encoded matrix. We note that for the encoding process we need to encode the \mathbf{A} matrix by pre-multiplying it with the appropriate generator matrix. Then the matrix-vector multiplication is carried out in the usual manner and at the end the resultant coded output vector is decoded to correct any errors that have occurred during the multiplication process. This procedure is explained in Figure 1.

In determining the performance improvement of an optical matrix vector multiplier employing some kind of error-correction code, several models for the noise present in the optical processor have been used. In this paper we considered basically four different cases for the noise present in the OMVM: 1) Signal-independent noise present in matrix \mathbf{A}^c only; 2) Signal-independent noise present in vector \mathbf{x} only; 3) Signal-dependent noise present in matrix \mathbf{A}^c only, and 4) Signal-dependent noise present in vector \mathbf{x} only.

For the case of noise present in matrix \mathbf{A}^c , each entry a_{ij} in \mathbf{A}^c is replaced by a noisy entry as follows;

$$\tilde{a}_{ij} = a_{ij}(1 + n_{ij}) + m_{ij} \quad (4)$$

where $i = 1, 2, 3, \dots, r$, and $j = 1, 2, 3, \dots, c$. Here r is the number of rows in the \mathbf{A}^c matrix and c is the number of columns in the same matrix. In the above equation n_{ij} and m_{ij} are zero mean Gaussian random variables with the same standard deviation, σ . These random variables are assumed to be jointly statistically independent. If the noise added is to be signal-independent, then n_{ij} is set to zero. In the case of noise present in vector \mathbf{x} , the same conditions apply to the elements of the vector.

3. BCH Codes

The properties and encoding/decoding procedures associated with BCH codes were presented in Ref. 9 and the results of applying these codes to a modulo-2 OMVM will be reiterated here for a comparison to the Reed-Solomon codes of the next section. In all the simulations reported in this paper, encoding, decoding and error-correction procedures were considered to be noiseless. The dimensions of the \mathbf{A} matrix were different in each simulation depending on the dimensionality of the error-correction code used in that particular simulation. However, since the dimensionality of the error-correcting code affects only the number of rows of the \mathbf{A} matrix, the number of columns in all the simulations was held fixed at five. For example, when (15,7) BCH codes were simulated, the dimensions of the \mathbf{A} matrix were 7x5, and when the (15,5) BCH code was used, those dimensions were 5x5. The dimension of the multiplier vector \mathbf{x} was fixed at 5x1 for compatibility.

The simulations were performed as follows: in the case of signal-independent noise in matrix \mathbf{A} for example, first a random \mathbf{x} vector and a random \mathbf{A} matrix were

formed. Then, noise of a fixed standard deviation was added to each element of the A^c matrix, after which the result was thresholded back to a binary, but noise, matrix. The product $y^c = A^c x$ was formed arithmetically and, after thresholding to binary and decoding, the decoded result was compared to the original result. If all output components matched, that trial was marked as correct, otherwise it was marked as wrong. This procedure was repeated for various standard deviations of the noise. In each case the number of trials was 500 minimum. Finally, the probability of correct detection (PCD) was plotted versus the standard deviation of the noise.

In this part of the research, two different binary BCH codes were simulated. The first was the (15,7) BCH code which is capable of correcting two errors. This code encodes 7 bits of an information vector into a 15-bit code word vector. The second code, a (15,5) binary BCH code, was better than the first in the sense that it can correct three errors instead of two. However, in this case one has to sacrifice the number of information bits that can be encoded. Thus, this code can encode a 5-bit information vector into a 15-bit code vector but can correct three errors. This is the usual trade-off encountered in error-correction coding.

Figure 2 shows the improvement obtained when there is signal-independent noise added to the A matrix. It can be observed that the three-error-correcting code supplied a better improvement than the two-error-correcting case. Figure 3 shows the results for the signal-dependent case. The use of error correction codes still provides improvement in the signal-dependent case when the data processed is binary. However, it will be seen that this is not the case when the data processed is non-binary.

In Figure 4, the results for signal-independent noise added to the \mathbf{x} vector are plotted. Due to the high correlation between the input vector noise and the output vector noise, the use of error correction codes provided almost no improvement. Likewise Figure 5 shows that again no enhancement is obtained when the noise in the system is signal-dependent. Thus, the input vector to an OMVM must be very noise-free for good system performance.

4. Reed-Solomon Codes

Reed-Solomon (RS) codes are non-binary codes; therefore, each code word symbol becomes a string of bits when transmitted across a binary channel. In case of a noise burst, which corrupts several consecutive bits on the channel, these bit errors are trapped within a small number of non-binary symbols. As opposed to correction of a long series of bits, Reed-Solomon codes need to correct only a few symbols for correct detection. These codes have been used extensively in many electronic information systems and have been proposed for use in optical memories.¹⁰

Reed-Solomon codes can be viewed as sets of algebraic curves defined by polynomials with a limited range of degrees. The degree limitation allows recovery of the complete curve even when the graph is assumed to be erased at many points. The relation of this idea to error control and correction in noise-corrupted digital channels is well known. These codes actually are a special subclass of generalized BCH codes. An (n,k) primitive RS code defined in the Galois field $GF(2^m)$ has code words of length

$$n = 2^m - 1 \quad (5)$$

where m is a positive integer, n is the number of code words symbols and k is the number of message symbols.

Because an RS code is, in one sense, a special case of the BCH codes, one can construct its generator polynomial, $g(x)$, in the same way as one constructs the $g(x)$ for any other BCH code. In this case, however, $g(x)$ can be factored completely into *linear* factors. Unlike BCH codes, RS codes have not been tabulated as a special class. The generator polynomial of the code is

$$g(x) = \prod_{i=0}^{n-k-1} (x + \alpha^{h+i}), \quad (6)$$

where α is a primitive element in $GF(2^m)$ and h is an integer constant. Different generating polynomials are formed with different values for h ; in practical applications by carefully choosing the constant h , the circuit complexity of the encoder and decoder can be reduced.¹¹ In the rest of the discussion presented here, however, only the $h = 1$ case is considered. In this case the generator polynomial $g(x)$ is

$$\begin{aligned} g(x) &= \prod_{i=0}^{n-k-1} (x + \alpha^{1+i}) \\ &= (x + \alpha)(x + \alpha^2)(x + \alpha^3) \dots (x + \alpha^{2^{t-1}})(x + \alpha^{2^t}). \end{aligned} \quad (7)$$

Expressed in another way

$$g(x) = g_0 + g_1x + g_2x^2 + \dots + g_{n-k-1}x^{n-k-1} + g_{n-k}x^{n-k}. \quad (8)$$

The above equation can be obtained from Equation (7) by first expanding it and then reducing it by using the arithmetic rules defined by the primitive polynomial over $GF(2^m)$.

A. Encoding

Encoding of RS codes can be done in many ways, such as by polynomial division, encoding in the frequency domain, and encoding using a Cauchy matrix or encoding using a generator matrix. Here only two of these encoding algorithms will be discussed, namely encoding by polynomial division and encoding using a generator matrix.

In the polynomial division method, a code word can be obtained in systematic form by adding $n-k$ ($=2t$) parity-check symbols to the data symbols, where t is the number of symbols which can be corrected. Using polynomial notation, we can write the code word, $v(x)$, as

$$v(x) = p(x) + x^{n-k}i(x), \quad (9)$$

where

$$p(x) = \sum_{i=0}^{2t-1} p_i x^i \quad (10)$$

is a polynomial over $GF(2^m)$ of degree $2t-1$ or less and $i(x)$ is the data word. The parity symbols are chosen such that $v(x)$ is divisible by the generator polynomial $g(x)$, i.e.,

$$p(x) = R_{g(x)}[x^{n-k}i(x)], \quad (11)$$

where $R_{g(x)}[\cdot]$ denotes the remainder after division by $g(x)$.

Thus the encoding of an RS code can be performed using the following algorithm; pre-multiply data polynomial $i(x)$ by x^{n-k} , obtain $p(x)$ as defined in (11), combine $p(x)$ and $x^{n-k}i(x)$ to obtain code word $v(x)$ as indicated in (9).

In the generator matrix method, the procedure is the same as that for BCH codes.¹² First we need the generator polynomial for the code. Previously it has been shown that the generator polynomial for an RS code can be obtained as

$$g(x) = \prod_{i=0}^{n-k-1} (x + \alpha^{1+i}) \quad (12)$$

$$= (x - \alpha)(x - \alpha^2)(x - \alpha^3) \dots (x - \alpha^{2^t-1})(x - \alpha^{2^t})$$

which can also be expressed as

$$g(x) = g_0 + g_1x + g_2x^2 + \dots + g_{n-k-1}x^{n-k-1} + g_{n-k}x^{n-k}. \quad (22)$$

In this case the generator matrix can again be constructed as in the BCH code case

as follows:

$$G_{k \times n} = \begin{bmatrix} g_{n-k} & g_{n-k-1} & \cdot & \cdot & \cdot & \cdot & g_3 & g_2 & g_1 & g_0 & 0 & 0 & 0 & 0 & 0 \\ 0 & g_{n-k} & g_{n-k-1} & \cdot & \cdot & \cdot & \cdot & g_3 & g_2 & g_1 & g_0 & 0 & 0 & 0 & 0 \\ 0 & 0 & g_{n-k} & g_{n-k-1} & \cdot & \cdot & \cdot & \cdot & g_3 & g_2 & g_1 & g_0 & 0 & 0 & 0 \\ \cdot & \cdot & \cdot & \cdot & \cdot & \cdot & \cdot & \cdot & \cdot & \cdot & \cdot & \cdot & \cdot & 0 & 0 \\ \cdot & \cdot & \cdot & \cdot & \cdot & \cdot & \cdot & \cdot & \cdot & \cdot & \cdot & \cdot & \cdot & 0 & 0 \\ \cdot & \cdot & \cdot & \cdot & \cdot & \cdot & \cdot & \cdot & \cdot & \cdot & \cdot & \cdot & \cdot & \cdot & 0 \\ 0 & 0 & 0 & 0 & 0 & g_{n-k} & g_{n-k-1} & \cdot & \cdot & \cdot & \cdot & g_3 & g_2 & g_1 & g_0 \end{bmatrix}$$

B. Decoding

There are many decoding algorithms developed for RS codes such as syndrome based decoding, algebraic decoding and transform decoding. Here we will only be interested in syndrome-based decoding. For the RS codes it is necessary to compute not only the error locators but also the amount of error; in other words, error values, Y_k , $k = 1, 2, \dots, 2t$. Therefore, decoding of RS codes includes all the steps required to decode BCH codes and another step to find the error values.^{13,14}

C. Computer Simulations

In this part of the research, simulation results obtained for the determination of the performance of Reed-Solomon codes, applied to optical matrix-vector multipliers, will be

presented. The same noise scenarios discussed in the previous section for BCH code simulations apply here also, with computations being performed modulo-16.

In this work, we simulated two RS codes. One was a four-error-correcting (15,7) code, i.e., $(n,k,t) = (15,7,4)$ RS code. Note that the length of the code word vector and that of the message vector are the same as for the (15,7) binary BCH code; however, in this case the code is capable of correcting four errors rather than only two. The other code was a five-error-correcting (15,5) code, i.e., $(15,5,5)$ RS code. Again note that the number of correctable errors in this case is two more than that in the BCH case. This increase in the number of correctable errors comes from switching from a binary code to a non-binary code. Also, in Reed Solomon codes there is much more flexibility in choosing the length of the message and code word vectors. The same matrix and vector dimensions as in the case of the BCH codes were used in these simulations. One additional feature is that the root-mean-square (RMS) error, normalized by the y vector magnitude, was used along with probability of correct detection as a measure of the quality of the decoded result vector.

Figures 6 and 7 show the improvement achieved when there is signal-independent noise added to the matrix A . The perfect right-shift of the curves indicates the success of the code applied over that specific region of standard deviation of noise. Figures 8 and 9 present the results for signal-dependent noise corrupting matrix A . We can still observe the perfect shift of the curves but this time the standard deviation of noise range is almost ten times smaller than in the signal-independent case. This means signal-dependent noise, when working with non-binary data, degrades the performance of the code seriously.

In Figures 10 and 11, the improvement obtained when signal-independent noise is present in the \mathbf{x} vector is shown. Again, there is no gain obtained by the use of error correction codes for this situation, just like the case for binary BCH codes. Figures 12 and 13 show the case for the signal-dependent noise in \mathbf{x} . One can notice that, once again, the standard deviation of noise range is much smaller than that for the signal-independent case.

5. Conclusions

The results presented here show the error performance enhancement that can be obtained in OMVMs by using binary and non-binary multiple-error-correction codes. In both cases it was shown that error-correction codes performed much better with a noiseless input vector and when the noise in the system is signal-independent. Although signal-dependent noise did not degrade performance very much over that of signal-independent noise for binary BCH codes, it was found that in the non-binary case it significantly decreased the enhancement that the code provided. However in the binary BCH code we could not achieve a great flexibility in choosing message and code word lengths. That is, the message vector length was known only after one has decided on the code word length and on the number of errors to be corrected. The performance of the code was directly proportional to the number of correctable errors. These limitations, and the restriction to modulo-2 arithmetic of the binary BCH code, were overcome by switching to a non-binary Reed-Solomon error-correction code.

The main result of using non-binary Reed-Solomon codes was a gain of flexibility in the construction of the dimensions of the matrix and vector and also a gain in the enhancement of error correction performance. From the plots of probability of correct detection and RMS error vs. noise variance, it can be seen that these codes provided much better improvement in a much wider range of standard deviation of noise for the signal-independent case than the BCH codes. However, although these codes performed better than BCH codes, in the signal-dependent noise case the degradation in the efficiency of the code was significant. This was due to the fact that noise inserted into the system was being amplified by the non-binary elements of the signal. This was the major drawback of these codes, since they extensively restricted the range of the standard deviation of the noise for which accuracy improvement was possible in the presence of signal-dependent noise.

Acknowledgments

We gratefully acknowledge the financial support of this research by the Air Force Office of Scientific Research under grant F49620-95-1-0140.

References

1. W.T. Rhodes and P.S. Giulfoyle, "Acoustooptic Algebraic Processing Architectures," *Proc. IEEE*, **72**, 820-830 (1984)
2. H.J. Caulfield and R.S. Putnam, "Fault Tolerance and Self-Healing in Optical Systolic Array Processors," *Opt. Eng.*, **24**, 65-67 (1985)

3. S. Liebowitz and D. Casasent, "Error-correction Coding in an Associative Processor," *Appl. Opt.*, **26**, 999-1004 (1987)
4. R.J. Marks, II and L.E. Atlas, "Composite Matched Filtering With Error Correction," *Opt. Lett.*, **12**, 135-137 (1987)
5. S. Oh, D.C. Park, R.J. Marks, II and L.E. Atlas, "Error Detection and Correction in Multilevel Algebraic Optical Processors," *Opt. Eng.*, **27**, 289-293 (1988)
6. S.A. Ellett, J.F. Walkup and T.F. Krile, "Error-correction Coding for Accuracy Enhancement in Optical Matrix-Vector Multipliers," *Appl. Opt.*, **31**, 5642-5653 (1992)
7. S.A. Ellett, T.F. Krile and J.F. Walkup, "Combining Digital Partitioning and Error-Correcting Codes for High Accuracy Optical Computing," *Optics & Laser Technology*, **26**, 301-311 (1994)
8. S.A. Ellett, T.F. Krile and J.F. Walkup, "Throughput Analysis of Digital Partitioning with Error-Correcting Codes for Optical Matrix-Vector Processors," *Appl. Opt.*, **34**, 6744-6751 (1995)
9. A. T. Caglar, T.F. Krile and J.F. Walkup, "Application of Multiple Error Correcting Binary BCH Codes to Optical Matrix-Vector Multipliers," *SPIE Proc.*, **2754**, 289-299 (1996)
10. M.A. Neifeld and M. McDonald, "Error Correction for Increasing the Useful Capacity of Photorefractive Memories," *Opt. Lett.*, **19**, 1483-1485 (1994)
11. E.R. Berlekamp, "Bit-Serial Reed-Solomon Encoder," *IEEE Trans. On Information Theory*, **28**, 869-874 (1982)

12. D.G. Hoffman, D.A. Leonard, C.C. Linder, K.T. Phelps, C.A. Rodger, J.R. Wall,
Coding Theory: The Essentials, Marcel Dekker, Inc., New York, NY (1991)
13. R.E. Blahut, Theory and Practice of Error Control Codes, Addison-Wesley, Reading,
MA (1984)
14. P. Sweeney, Error Control Coding: An Introduction, Prentice-Hall, Englewood Cliffs,
MA (1991)

List of Figures

- Figure 1. Application of error-correction to optical matrix-vector multipliers.
- Figure 2. PCD performance improvement of (15,7) and (15,5) binary BCH codes in the case of signal-independent noise present in the matrix A only.
- Figure 3. PCD performance improvement of (15,7) and (15,5) binary BCH codes in the case of signal-dependent noise present in the matrix A only.
- Figure 4. PCD performance improvement of (15,7) and (15,5) binary BCH codes in the case of signal-independent noise present in the vector x only.
- Figure 5. PCD performance improvement of (15,7) and (15,5) binary BCH codes in the case of signal-dependent noise present in the vector x only.
- Figure 6. PCD performance improvement of (15,7,4) and (15,5,5) non-binary Reed-Solomon codes in the case of signal-independent noise in matrix A only.
- Figure 7. RMS error improvement of (15,7,4) and (15,5,5) non-binary Reed-

Solomon codes in the case of signal-independent noise in matrix A only.

Figure 8. PCD performance improvement of (15,7,4) and (15,5,5) non-binary Reed-

Solomon codes in the case of signal-dependent noise in matrix A only.

Figure 9. RMS error improvement of (15,7,4) and (15,5,5) non-binary Reed-

Solomon codes in the case of signal-dependent noise in matrix A only.

Figure 10. PCD performance improvement of (15,7,4) and (15,5,5) non-binary Reed-

Solomon codes in the case of signal-independent noise in vector x only.

Figure 11. RMS error improvement of (15,7,4) and (15,5,5) non-binary Reed-

Solomon codes in the case of signal-independent noise in vector x only.

Figure 12. PCD performance improvement of (15,7,4) and (15,5,5) non-binary Reed-

Solomon codes in the case of signal-dependent noise in vector x only.

Figure 13. RMS error improvement of (15,7,4) and (15,5,5) non-binary Reed-

Solomon codes in the case of signal-dependent noise in vector x only.

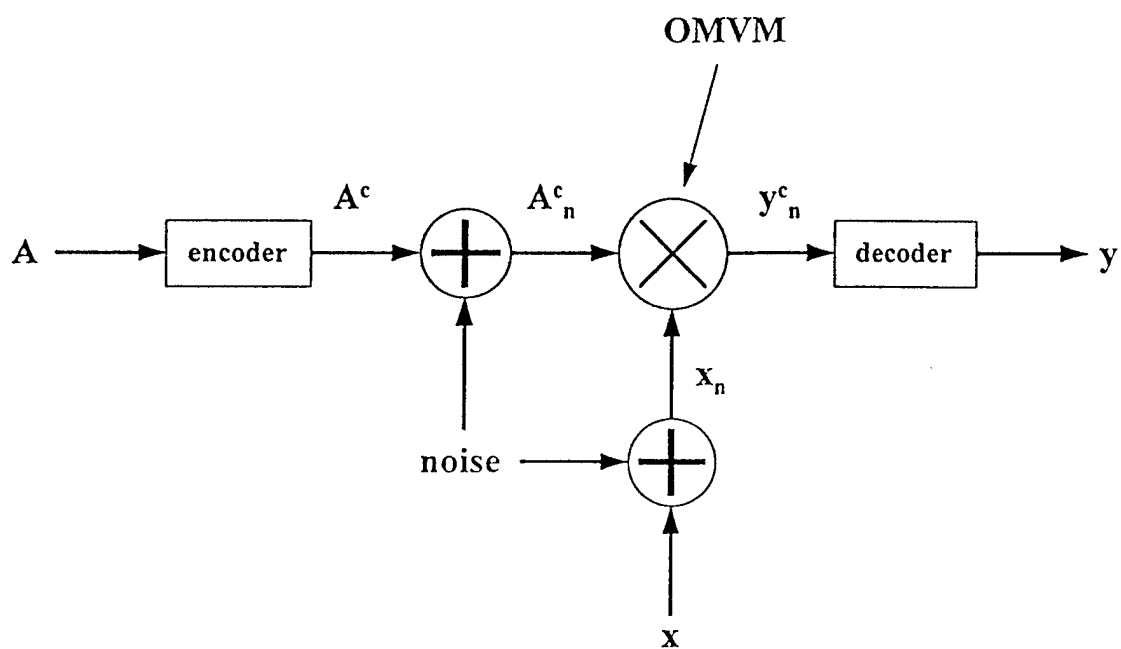


Figure 1 Application of error-correction to optical matrix-vector multipliers.

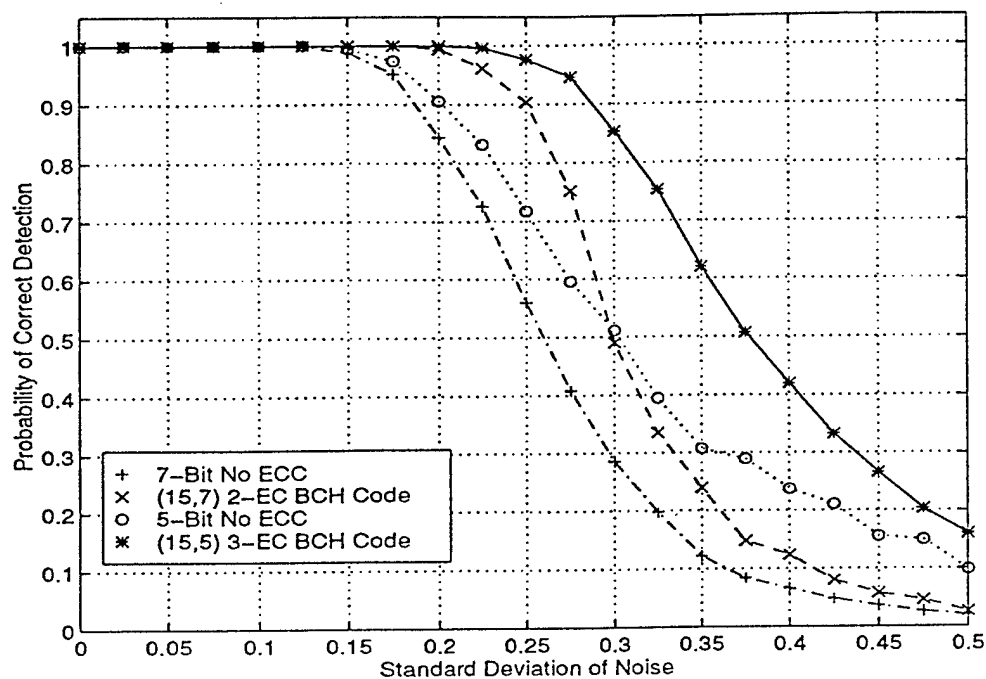


Figure 2. PCD performance improvement of (15,7) and (15,5) binary BCH codes in the case of signal-independent noise present in the matrix A only.

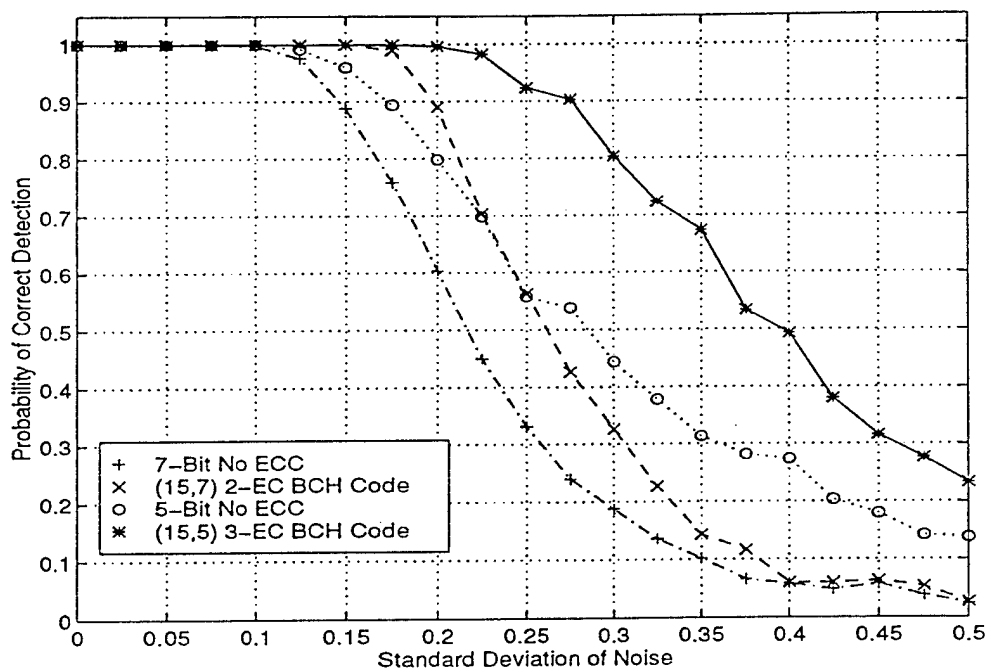


Figure 3. PCD performance improvement of (15,7) and (15,5) binary BCH codes in the case of signal-dependent noise present in the matrix A only.

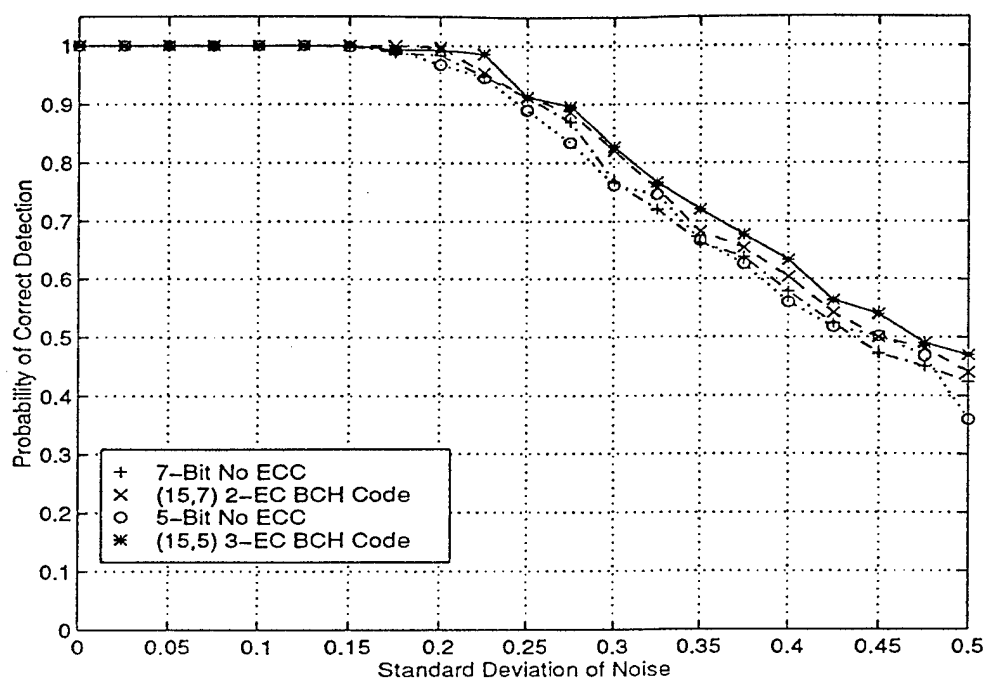


Figure 4. PCD performance improvement of (15,7) and (15,5) binary BCH

codes in the case of signal-independent noise present in the vector x only.

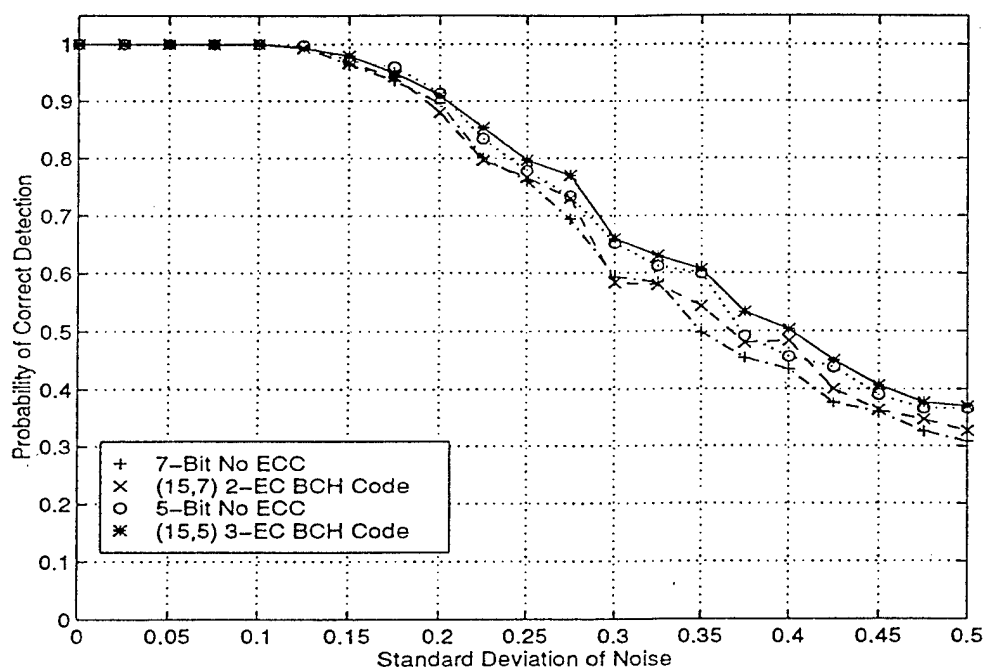


Figure 5. PCD performance improvement of (15,7) and (15,5) binary BCH

codes in the case of signal-dependent noise present in the vector x only.

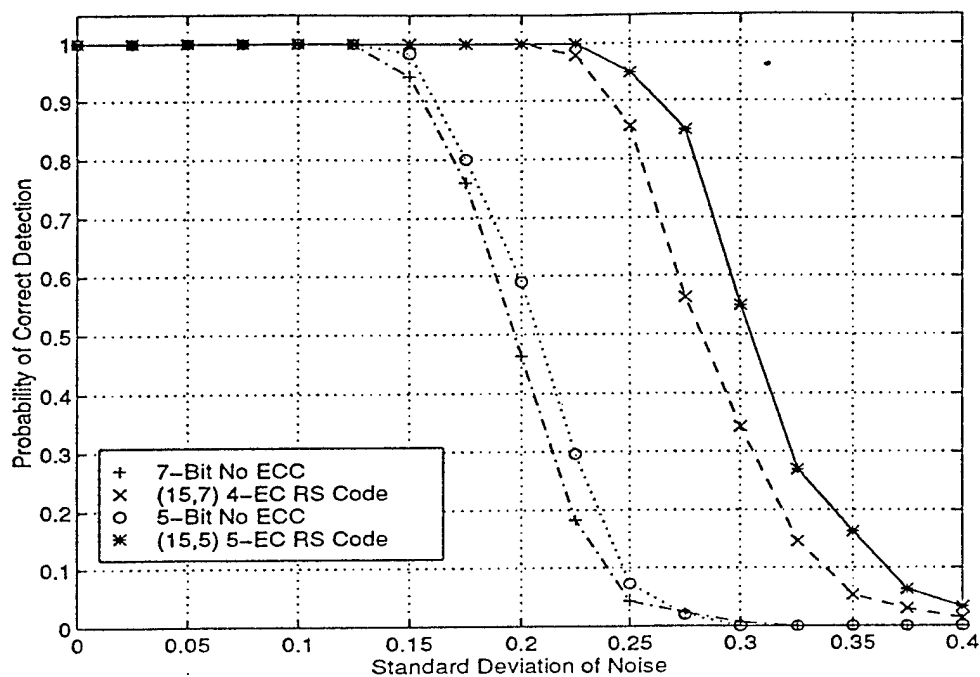


Figure 6. PCD performance improvement of (15,7,4) and (15,5,5) non-binary Reed-Solomon codes in the case of signal-independent noise in matrix A only.

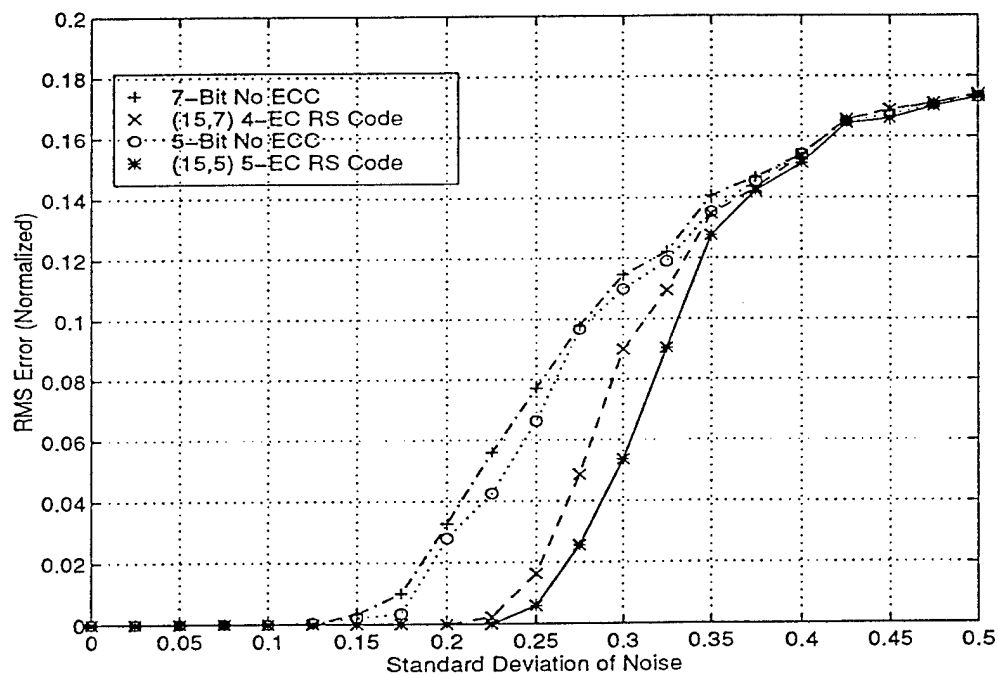


Figure 7. RMS error improvement of (15,7,4) and (15,5,5) non-binary Reed-Solomon codes in the case of signal-independent noise in matrix A only.

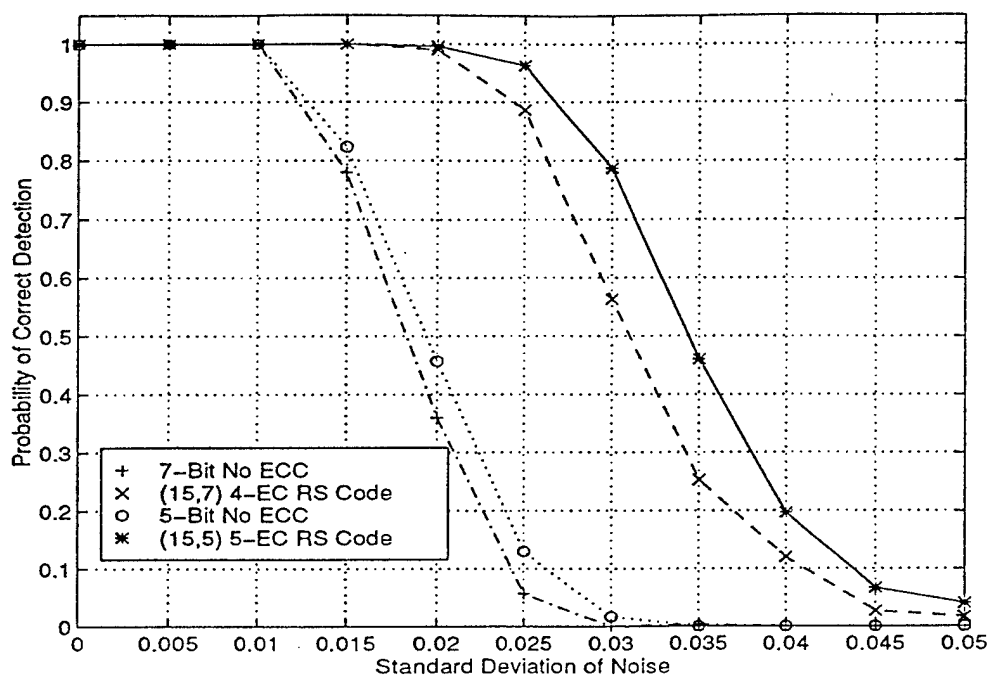


Figure 8. PCD performance improvement of (15,7,4) and (15,5,5) non-binary

Reed-Solomon codes in the case of signal-dependent noise in matrix A only.

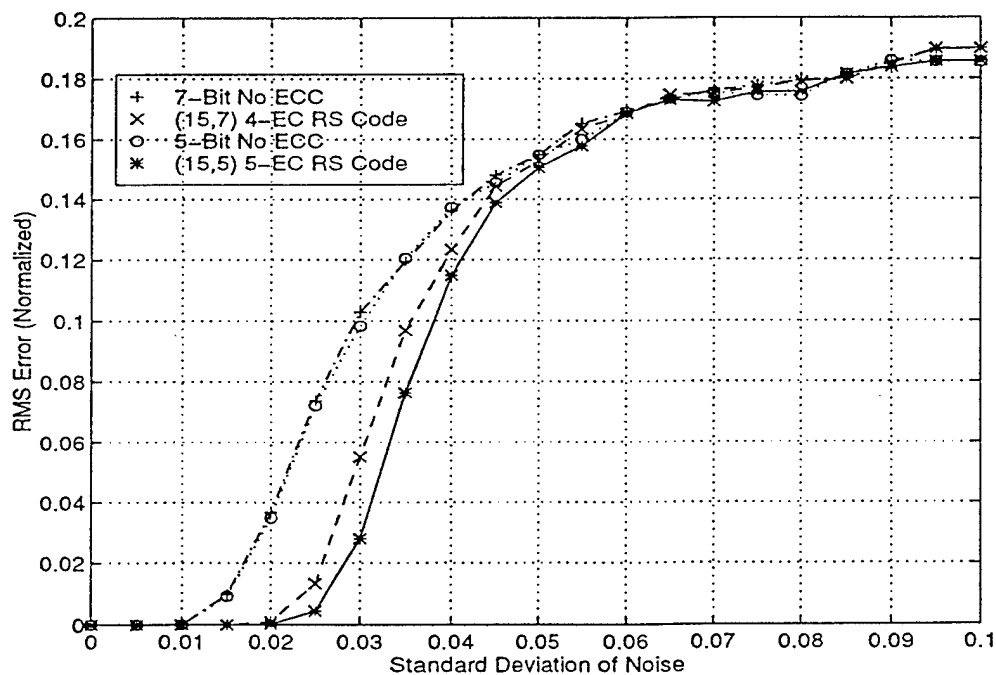


Figure 9. RMS error improvement of (15,7,4) and (15,5,5) non-binary Reed-

Solomon codes in the case of signal-dependent noise in matrix A only.

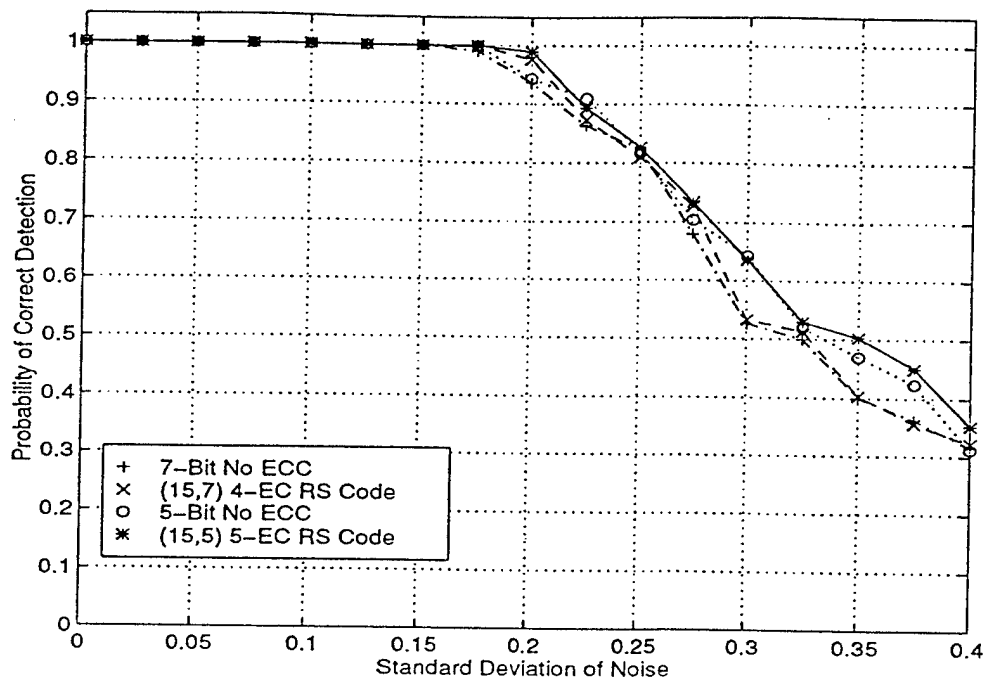


Figure 10. PCD performance improvement of (15,7,4) and (15,5,5) non-binary Reed-Solomon codes in the case of signal-independent noise in vector x only.

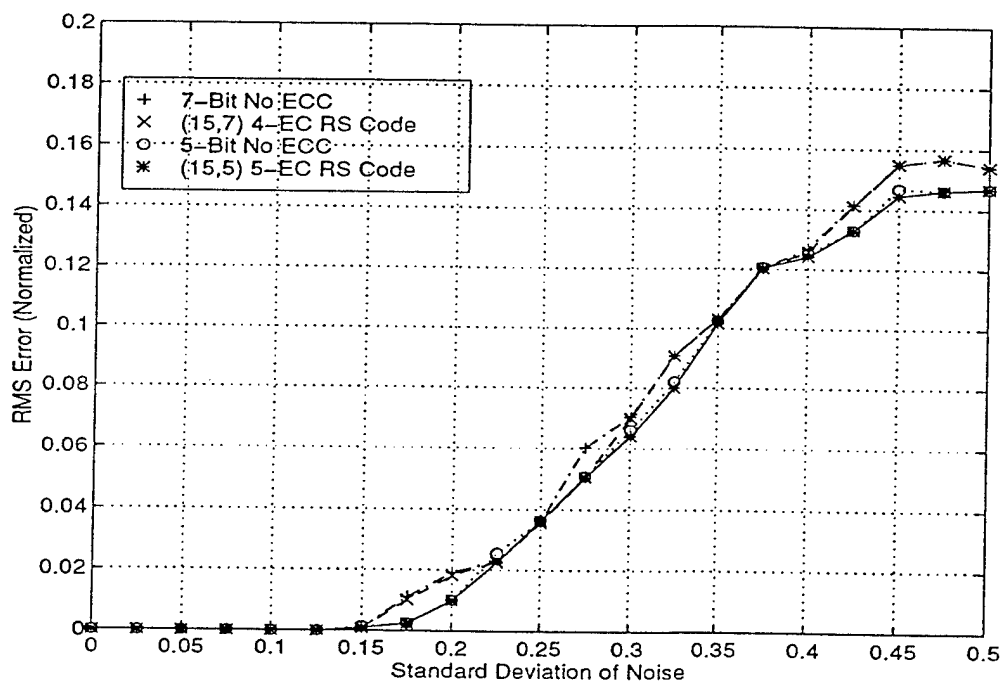


Figure 11. RMS error improvement of (15,7,4) and (15,5,5) non-binary Reed-Solomon codes in the case of signal-independent noise in vector x only.

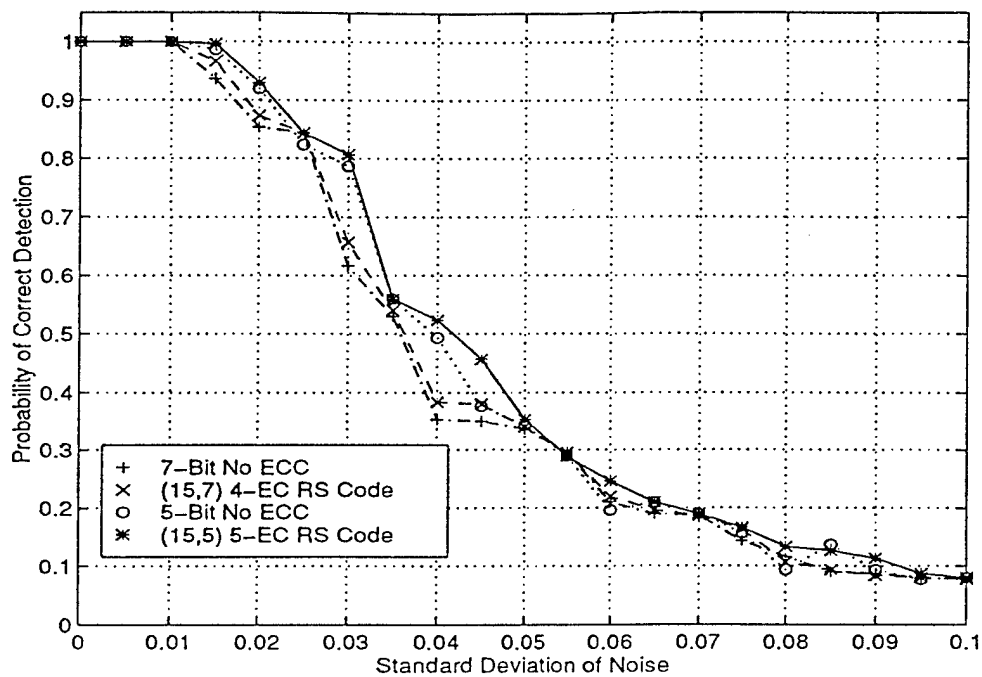


Figure 12. PCD performance improvement of (15,7,4) and (15,5,5) non-binary Reed-Solomon codes in the case of signal-dependent noise in vector x only.

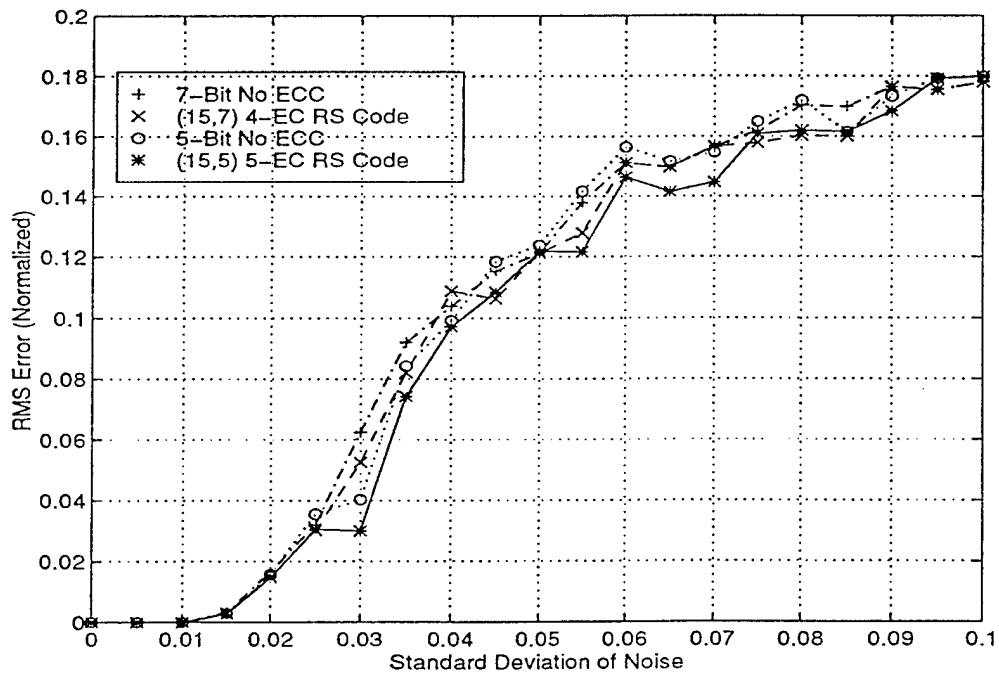


Figure 13. RMS error improvement of (15,7,4) and (15,5,5) non-binary Reed-Solomon codes in the case of signal-dependent noise in vector x only.

The relationship between bandwidth and bit error rate for a photon echo memory with chirped write/read pulses

J. Y. Choi, J. F. Walkup, T. F. Krile, and D. J. Mehrl

Texas Tech University, Lubbock, Texas 79409-3102

The photon echo memory requires a write/read pulse with infinite bandwidth for accurate echo data recovery. The infinite bandwidth implies a delta-function pulse in the time domain, however, which is impossible to achieve experimentally. Instead, several techniques are used. One popular method is to use chirped write/read pulses to generate a pulse with as broad a bandwidth as possible. The chirped write/read pulse has a much larger bandwidth than does an unchirped pulse. However, the bandwidth is still comparable to the data pulse bandwidth and this limits the accuracy of the echo signal recovery. In this paper we formulate a model for the photon echo system which uses a chirped write/read pulse and we analyze the effect of its finite bandwidth on the echo signal using a statistical noise model. We also analyze the effect of echo efficiency on the echo output signal.

Keywords : photon echo memory, frequency chirping, noise model

1. Introduction

Among optical memory techniques, there are two schemes which have received the most attention to date, namely, Frequency Domain Optical Storage(FDOS) and Time Domain Optical Storage(TDOS). A particularly attractive feature of time-domain and frequency-domain optical storage is the ability to store many bits of information in a diffraction-limited spot⁽¹⁾ thereby dramatically increasing the data storage density. In FDOS, the reading and writing are performed in the frequency domain; i.e. a narrowband laser beam is frequency scanned across the sample's inhomogeneous line, spectral holes are

written at those frequencies where “1”s(or “0”s) are desired, and the written data are read out by again scanning a narrowband laser and detecting the changes in the sample’s transmission. The optical frequency or wavelength at which holes are burned is used to encode digital information where, for instance, the presence of a hole at a particular optical frequency may be used to encode a digital “1” and the absence of a hole a digital “0” or vice versa. In FDOS, it has been implicitly assumed that in all cases the writing and reading times for a single bit are longer than the homogeneous dephasing time of the transition, T_2 , so that a rate equation analysis can be used to describe the kinetics of the laser-material interaction. Due to the additional use of the frequency dimension, multiple bits can be stored in one laser focal volume, yielding areal densities several orders of magnitude higher than those obtainable with conventional optical or magnetic storage.

In TDOS, on the contrary, the temporal Fourier transform of the input data sequence is written into the inhomogeneous absorption profile. Data are encoded by means of temporal modulation onto the waveform of a finite duration data beam. A single spatial location is illuminated by this beam together with a reference beam. The two beams act to record the Fourier transform of the data beam’s temporal envelope into the spectral absorption profile. Individual bits are not localized to a specific spectral channel; instead, they are stored throughout a region of spectral-addressing space. Extended spectral storage of bits eliminates the speed limitation intrinsic in FDOS. In TDOS, to store and recall the input data faithfully, the Fourier transform of the input data sequence must be narrower than the inhomogeneous bandwidth. This requirement on the Fourier transform of the input data sequence sets an upper limit for the TDOS read-write data rate that essentially equals the inhomogeneous bandwidth of the transition.

To record and recover data accurately, there are several assumptions to be satisfied⁽²⁾. They are (1) the pulse data obeys the constraint $\theta_{ob}(\omega) \leq 1$ for all ω , where $\theta_{ob}(\omega)$ represents the area of the object

pulse; (2) the write and read pulses are sufficiently short to have uniform spectral components over the region where $\theta_{ob}(\omega)$ is appreciable; and (3) over the same spectral region, the absorption profile is essentially constant (and close to its maximum value). In reality, however, those three conditions cannot be completely satisfied because of technical limitations. For example, to excite the atoms uniformly over the wide spectral region, the write pulse must have a short duration and sufficient power at the same time. These conflicting conditions will be compromised in practice and this creates a non-ideal situation for actual echo experiments. In this paper, we formulate a simple model for the experimental situation including noise and, by analyzing this model, derive the output signal characteristics. Finally, we compare the analytical and simulation results.

2. Photon echo noise model

A conceptual view of the photon echo technique is shown in Fig. 1. The recovered echo signal is expressed as

$$E_{\text{echo}}(t) = \alpha \mathfrak{F}^{-1}\{E_1^*(f)E_2(f)E_3(f)\} \quad (1)$$

where α is the overall attenuation of the photon echo system, \mathfrak{F}^{-1} is the inverse Fourier transform, $E_1^*(f)$ is the complex conjugate of the Fourier transform of the write pulse, $E_2(f)$ is the Fourier transform of the data pulses, and $E_3(f)$ is the Fourier transform of the read pulse, respectively. As described in Fig. 1, the echo signal is the convolution of the data pulses with the correlation of the write and read pulses. To simplify the equation, let's replace $E_1^*(f)E_3(f)$ with $H(f)$, so that

$$E_{\text{echo}}(t) = \alpha \mathfrak{F}^{-1}\{H(f)E_2(f)\} \quad (2)$$

Now, using the transfer function concept, we can represent this system as in Fig.2.

In actual signal recovery, noise is another important factor to be considered. There are several kinds of noise sources in the photon echo experimental environment. These include noise from laser

phase fluctuations, laser intensity fluctuations, material imperfections, electronic circuit noise, etc. Depending on the situation, some noise sources are dominant while others maybe negligible. In our model we assumed that the echo intensity is very low and the dominant noise source is shot noise from the photodetector. The total system including the noise is shown in Fig. 3.

As is well known, shot noise is based on the fundamentally random interaction between light and a detector. By Mandel's formula⁽³⁾, if we know the distribution of integrated intensity⁽⁴⁾ at the input to a photodetector, we can estimate the distribution of the output of the photodetector by

$$P(K) = \int_0^\infty \frac{(\gamma W)^K}{K!} e^{-\gamma W} p_W(W) dW \quad (3)$$

where $P(K)$ is the probability of observing K photoevents in the time interval $(t, t + \tau)$, $\gamma = \eta / h \bar{\nu}$, where h is Planck's constant (6.626196×10^{-34} joule-sec), $\bar{\nu}$ is the mean optical frequency of the radiation, the quantum efficiency, η , represents the average number of photoevents produced by each incident photon, W is the integrated intensity in the time interval $(t, t + \tau)$, and $p_W(W)$ is the probability density function (PDF) of the integrated intensity.

Based on this model, we first find the system transfer function composed of chirped write/read pulses⁽⁵⁾, $H(\omega)$ and using the transfer function and arbitrary input data, we will evaluate the integrated intensity at the input to the detector. Then, using Mandel's formula, we estimate the probability density of the output signal as degraded by shot noise. Finally, by summing the two noise components, we estimate the probability distribution of the echo output signal.

3. The analysis

The transfer function of the system, $H(f)$, is represented by the product of write and read pulse spectra, that is, $E_1^*(f)E_3(f)$. The photon echo memory requires write/read pulses with infinite bandwidth for accurate echo data recovery as can be seen from Eq. (1). In an experimental situation, however, it is

not possible to generate a pulse with infinite bandwidth. Instead, we may use various techniques to generate a pulse with as broad a bandwidth as possible. Frequency chirping is one such technique.

Frequency chirped write and read pulses can be expressed, respectively, as in Eq. (4),

$$E_1(t) = \text{rect}\left(\frac{t-t_1}{T}\right) \cdot \cos(2\pi f_0(t-t_1) + \pi k(t-t_1)^2)$$

$$E_3(t) = \text{rect}\left(\frac{t-t_3}{T}\right) \cdot \cos(2\pi f_0(t-t_3) + \pi k(t-t_3)^2), \quad (4)$$

where $E_1(t)$ is the write pulse, $E_3(t)$ is the read pulse, k is the chirp rate, in Hz/sec, and T is the chirp duration. The instantaneous frequency changes in a linear fashion from $f_0 - kT/2$ to $f_0 + kT/2$. The net frequency sweep, $\Delta = kT$, is the difference in these two values. To find the transfer function, we first find the Fourier transform of each pulse. These are given by,

$$E_1(f) = \frac{1}{2} e^{-j2\pi f t_1} \left[\int_{-T/2}^{T/2} e^{j2\pi \{(f_0-f)t + \frac{1}{2}kt^2\}} dt + \int_{-T/2}^{T/2} e^{-j2\pi \{(f_0+f)t + \frac{1}{2}kt^2\}} dt \right]$$

$$E_3(f) = \frac{1}{2} e^{-j2\pi f t_3} \left[\int_{-T/2}^{T/2} \exp^{j2\pi \{(f_0-f)t + \pi kt^2\}} dt + \int_{-T/2}^{T/2} \exp^{-j2\pi \{(f_0+f)t + \pi kt^2\}} dt \right] \quad (5)$$

The second integral of each pulse essentially defines the spectrum at negative frequencies and has the same distribution for the positive frequencies. Also, if f_0/kt is sufficiently large, the spectrum of each side will not overlap. Therefore, if we have the distribution for positive frequencies, we can obtain the distribution for negative frequencies also. Calculating the first integral, we obtain

$$E_1(f) = \frac{1}{2} e^{-j2\pi f t_1} \sqrt{\frac{1}{2k}} e^{-j\frac{\pi(f_0-f)^2}{k}} \{ C(\sqrt{2k}(\frac{T}{2} + \frac{f_0-f}{k})) + j \cdot S(\sqrt{2k}(\frac{T}{2} + \frac{f_0-f}{k})) + C(\sqrt{2k}(\frac{T}{2} - \frac{f_0-f}{k})) + j \cdot S(\sqrt{2k}(\frac{T}{2} - \frac{f_0-f}{k})) \}, \quad (6.1)$$

$$E_3(f) = \frac{1}{2} e^{-j2\pi f t_3} \sqrt{\frac{1}{2k}} e^{-j\frac{\pi(f_0-f)^2}{k}} \{ C(\sqrt{2k}(\frac{T}{2} + \frac{f_0-f}{k})) + j \cdot S(\sqrt{2k}(\frac{T}{2} + \frac{f_0-f}{k})) + C(\sqrt{2k}(\frac{T}{2} - \frac{f_0-f}{k})) + j \cdot S(\sqrt{2k}(\frac{T}{2} - \frac{f_0-f}{k})) \}, \quad (6.2)$$

where

$$C(x) \equiv \int_0^x \cos \frac{\pi}{2} z^2 dz \text{ and } S(x) \equiv \int_0^x \sin \frac{\pi}{2} z^2 dz \quad (7)$$

are the Fresnel integrals⁽⁶⁾. The transfer function derived from Eq. (6-1) and (6-2) is given by,

$$H(f) = E_1^*(f) E_3(f) = \frac{1}{8k} e^{-j2\pi f(t_3 - t_1)} [\{C(z_2) + C(z_1)\}^2 + \{S(z_2) + S(z_1)\}^2], \quad (8)$$

where

$$Z_2 = \sqrt{2k} \left(\frac{T}{2} + \frac{f_0 - f}{k} \right) \text{ and } Z_1 = \sqrt{2k} \left(\frac{T}{2} - \frac{f_0 - f}{k} \right). \quad (9)$$

Using the fact that the frequency shift is $\Delta f = kT$, the arguments Z_1 and Z_2 will be

$$Z_{1,2} = \sqrt{\frac{\Delta f \cdot T}{2}} \left(1 \pm \frac{2(f_0 - f)}{\Delta f} \right). \quad (10)$$

Inspection of (10) shows that $\Delta f \cdot T$ is the only auxiliary variable present besides the frequency deviation, i.e. $(f_0 - f) / \Delta f$. This product is called the dispersion factor and is denoted by $D^{(7)}$. Figs. 4, 5, and 6 show the system transfer function for several values of the dispersion factor and frequency deviation.

Qualitatively, these curves show that, as the dispersion factor is increased, the spectrum shape becomes more nearly rectangular, with a total bandwidth approaching Δf . In a real experiment we can make D large, generally much greater than 100, so we will assume that the transfer function approximates an ideal bandpass filter, that is,

$$H(f) = \text{rect}\left(\frac{f - f_c}{B}\right), \quad (11)$$

where f_c is the center frequency of the bandpass filter and $B = \Delta f$ is the bandwidth of the filter.

Now, we will find the echo signal characteristics. From Eq. (2), we know that the echo signal is the convolution of the transfer function and data signal. When the data is just a single pulse, the echo signal will be a pulse smoothed by the transfer function. The echo pulse smoothness depends on both the

data pulse width and the transfer function bandwidth. When the data pulse is a string of multiple bits, the echo signal may be described by,

$$|E_{\text{echo}}(t)| = \alpha \sum_{i=1}^N E_i \cdot \text{rect}\left(\frac{t-t_i}{\tau}\right) * \text{sinc}(B(t-t_i)), \quad (12)$$

where α is the attenuation constant, E_i is the amplitude of each pulse, τ is the data pulse width, and $*$ denotes convolution. For the pulse series, we expect interference between adjacent pulses. That interference will depend on the input data distribution. Therefore, when we know the data distribution, we can calculate the integrated intensity of the echo signal exactly.

The integrated intensity $W(t_0)$ at the input of the photodetector can also be calculated from Eq. (12). That is

$$W(t_0) = \alpha^2 \int_{t_0-\tau/2}^{t_0+\tau/2} \sum_{i=1}^N \sum_{j=1}^N E_i E_j \int_{t-t_i-\tau/2}^{t-t_i+\tau/2} \int_{t-t_j-\tau/2}^{t-t_j+\tau/2} \text{sinc}(B(x-t_i)) \text{sinc}(B(y-t_j)) dx dy dt. \quad (13)$$

Using Eq. (13), we can calculate the integrated intensity for each input pulse. From that, we can derive a PDF for the integrated intensity. To find the output distribution caused by shot noise, we use Mandel's formula(3) as described earlier.

In the photon echo detection system, there are many kinds of noise, such as shot noise, dark current noise, thermal noise, etc. Among those noise sources, depending on the detector which is used for the detection, there will be a dominant noise. In general, when *pin* photodiodes are used, the dominating noise currents are those of the detector load resistor (the thermal current) and the active elements of the amplifier circuitry. For avalanche photodiodes the thermal noise is of lesser importance, and the photodetector noise sources usually dominate⁽⁸⁾. The principal noise sources associated with photodetectors are shot noise, dark current noise, and surface leakage current noise. Here, we assume that the shot noise is the dominant noise, and find the relationship between the bandwidth, echo efficiency,

and output characteristics. The number of photoevents, which is related to the bandwidth and echo efficiency of the system, has a different PDF for each combination of bandwidth and echo efficiency. Ideally, if the bandwidth is infinite, the integrated intensity has a Dirac-delta function PDF, and the number of photoevents will be Poisson distributed by Eq. (3). When the bandwidth is finite, the integrated intensity for each data pulse will be different, and the number of photoevents will deviate from the Poisson distribution. Fig. 7 shows a typical distribution of the number of photoevents for a specific bandwidth.

To find the relationship between the bandwidth and the number of photoevents, first we find the relationship between the bandwidth and the integrated intensity. As was mentioned earlier, the integrated intensity for each data will be different from data to data depending on the pulse position and adjacent pulses. Theoretically, the effect on a particular data pulse comes from all other pulses in the pulse train, but in reality, the major effect comes from the adjacent pulses. Here, we analyze the impact of the adjacent pulses only (Fig. 8). For three pulses, the input data is expressed by

$$x(t) = x_0 \cdot \text{rect}\left(\frac{t - (t_0 - \tau)}{\tau}\right) + x_1 \cdot \text{rect}\left(\frac{t - t_0}{\tau}\right) + x_2 \cdot \text{rect}\left(\frac{t - (t_0 + \tau)}{\tau}\right), \quad (14)$$

where x_0 , x_1 , and x_2 can be either “0” or “1” depending on the data sequence. The equations for the relationship between the bandwidth of the system and the integrated intensity for every case can be found in [9]. Table 1 shows the relationship between the bandwidth and the normalized integrated intensity for all eight data cases.

For the analysis of the output, it might be convenient to approximate the PDF by a known distribution. Fig. 9 shows the original distribution and a Gaussian curve approximation for each data (data “0” and data “1”). As we can see in Fig. 9, the Gaussian approximation of data “0” is not particularly good but the approximation of data “1” is very close to the original distribution. The

Gaussian approximation is made for the purpose of calculating the bit error rate for each bandwidth and echo efficiency combination, and we are more interested in whether the tail approximation is good or not. As we can see, the tail of the Gaussian curve for data “0” is slightly lower than the original curve while the tail of the Gaussian curve for data “1” is slightly higher than the original distribution. Therefore, we can assume that errors from the approximations can be compensated and that the calculation of a bit error rate from the approximated Gaussian curve will be accurate enough for the original distribution.

To calculate the mean and variance of the photoevents, we use Eq. (15)⁽⁴⁾.

$$\bar{K} = \gamma \bar{W}, \quad \sigma_K^2 = \gamma \bar{W} + \gamma^2 \sigma_W^2 \quad (15)$$

where \bar{K} is the mean of the number of photoevents, \bar{W} is the mean of the integrated intensity, σ_K^2 is the variance of the number of photoevents, and σ_W^2 is the variance of the integrated intensity. If we assume the equiprobable data cases, we can find the mean and variance of the normalized integrated intensity directly from the relationship between the bandwidth and the normalized integrated intensity using the relationships

$$\begin{aligned} m_0 &= \frac{M_{00} + M_{01} + M_{02} + M_{03}}{4}, \quad \sigma_0^2 = \sum_{i=1}^4 (M_{0i} - m_0)^2 \\ m_1 &= \frac{M_{10} + M_{11} + M_{12} + M_{13}}{4}, \quad \sigma_1^2 = \sum_{i=1}^4 (M_{1i} - m_1)^2 \end{aligned} \quad (16)$$

where m_0 , and m_1 are the means of the normalized integrated intensity for data “0” and data “1”, respectively, M_{ii} is the value from Table 1, while σ_0^2 and σ_1^2 are the variances of the normalized integrated intensity for data “0” and data “1”, respectively.

To calculate the bit error rate for each bandwidth and echo efficiency combination, we first calculate the mean and variance of the integrated intensity for the data “0” and data “1” cases. Because we know the relationship between the bandwidth and the normalized integrated intensity, if we know the

bandwidth of the system and the real power of the output, we can then calculate the mean and variance of the data “0” and data “1”. Fig. 10 shows the changes in the mean and standard deviation of data “0” and data “1” of normalized integrated intensity depending on the bandwidth. The mean and variance of the number of photoevents are related to the integrated intensity by Eq. (15), and since we know the mean and variance of the integrated intensity from Eq. (16), we can then calculate the mean and variance of the number of photoevents. Using a Gaussian approximation, the PDF of the output distribution of photoevents can be expressed as

$$\begin{aligned} P_{\text{data}(0)}(k) &= \frac{1}{\sqrt{2\pi\sigma_{k0}^2}} \exp\left(-\frac{(k - \bar{K}_0)^2}{2\sigma_{k0}^2}\right) \text{ and} \\ P_{\text{data}(1)}(k) &= \frac{1}{\sqrt{2\pi\sigma_{k1}^2}} \exp\left(-\frac{(k - \bar{K}_1)^2}{2\sigma_{k1}^2}\right), \end{aligned} \quad (17)$$

where \bar{K}_0 is the mean of the number of photoevents for data “0”, σ_{k0} is the standard deviation of the number of photoevents for data “0”, \bar{K}_1 is the mean of the number of photoevents for data “1” and σ_{k1} is the standard deviation of data “1”. From Eq. (17), we can estimate the bit error rate for any combination of bandwidth and echo efficiency. Fig. 11 shows the relationship between the bit error rate and the bandwidth and echo efficiency. The solid lines show the analytical results which are based on the bandpass filter and three pulse model while the circles show the simulation results which used a random data pulse train. Figure 11 shows that the bandpass filter and three pulse model is in good agreement with the simulation results. The only big error occurs when the system bandwidth is infinity. In reality, however, the bandwidth of the system is finite, so we can ignore the infinite bandwidth case.

5. Conclusion

In conclusion, we formulated a photon echo noise model and analyzed the relationship between the bit error rate and the bandwidth and echo efficiency for chirped write/read pulses. The analysis

showed that the chirped write/read pulse combination can be simplified as an ideal bandpass filter if the bandwidth of the write/read pulse is much less than the chirp width of the pulses. Use of the ideal bandpass model simplifies the analysis considerably. From the bandpass filter model, we can derive the output characteristics of the shot noise. The analysis shows that the mean, standard deviation of data "0" and the standard deviation of data "1" decrease while the mean of data "1" increases when the bandwidth of the system increases. The mean of each data are exactly proportional to the echo efficiency, that is output power, but the standard deviation is not. The analysis shows that the standard deviation increases a little more slowly than the mean of the data when the output power increases. That explains that the bit error rate of the output signal decreases when the output power increases (Fig. 10(b)). The relationship between the bandwidth and the bit error rate shows that the error probability decreases rapidly when we increase the bandwidth from $1/\tau$ to $4/\tau$, however, increasing the bandwidth beyond that does not give much benefit in terms of bit error rate. Therefore, in terms of the bit error rate, we conclude that a bandwidth of $4/\tau$ is sufficient for accurate echo signal recovery.

The authors gratefully acknowledge the support of this work by the Air Force Office of Scientific Research, USAF, under AFOSR Grant F49620-95-1-0140.

References

1. W. E. Moerner, *Persistent Spectral Hole-Burning: Science and Applications*, (Springer-Verlag, 1988), Chap.7, pp. 251-307.
2. T. W. Mossberg, "Time-domain frequency-selective optical data storage", Optics Letters, Vol.7, No. 2, 1982, 77-79.
3. L. Mandel, Proc. Phys. Soc. (London), 74, 233 (1959).
4. Joseph W. Goodman, *Statistical Optics*, (Wiley, New York, 1985), Chap. 9, pp. 466 - 470.
5. X. A. Shen and R. Kachru, "Coherent saturation removal in time-domain optical memory by storage of frequency-chirped data pulses", Optics Letters, Vol. 18, No. 22, 1993, 1967-1969.
6. Anthony VanderLugt, *Optical Signal Processing*, (John Wiley & Sons, Inc., 1992), Chap. 3, pp.90.
7. J. R. Klauder, A. C. Price, S. Darlington, and W. J. Albersheim, "The theory and design of chirp radars", The Bell System Technical Journal, July 1960.
8. Gerd Keiser, *Optical Fiber Communications*, (McGraw-Hill, Inc., 1991), pp. 248.
9. Jin Youb Choi, *Noise Modeling of a Photon Echo Memory* (Ph. D. dissertation, Texas Tech University, 1997)

Figure Captions

Fig.1 Conceptual view of time-domain optical storage. The write pulse prepares for the storage of the data pulses in the material. The data pulses are stored in the material in a Fourier transform domain. The read pulse recovers the data. Each retrieved data pulse is the convolution of the corresponding input data pulse and the correlation of the write and read pulses.

Fig. 2 System representation of the photon echo memory. $E_2(t)$ represents the data pulses, $H(f)$ represents the correlation between the write pulse and the read pulse and the attenuator represents the system's overall attenuation.

Fig.3 The noise analysis model for the photon echo memory system. $W(t_0)$ is the integrated intensity at the input of the photodetector. The shot noise is from the random interaction between a light and a photodetector.

Fig.4. Spectral amplitude of a chirp signal for $D=12$. The x-axis shows the frequency offset from the center frequency, i.e., $(f-f_0)/\Delta f$. The dispersion factor is relatively small, and the curve is not very rectangular.

Fig.5 Spectral amplitude of a chirp signal for $D=60$. The x-axis again shows the frequency offset from the center frequency, i.e., $(f-f_0)/\Delta f$. This curve is more rectangular than Fig. 4.

Fig. 6 Spectral amplitude of a chirp signal for $D=120$. The x-axis shows the frequency offset from the center frequency, i.e., $(f-f_0)/\Delta f$. This curve is now nearly rectangular.

Fig. 7 The probability density function of the number of photoevents. The x-axis shows the number of photoevents and y-axis shows the probability for each number of photoevents. For the calculation, we used 5 nw output power, 50 nsec pulse width, 527.39 nm wavelength, quantum efficiency of detector of “1”.

Fig. 8 The data pulse sequence for analysis of bandwidth effect

Fig. 9 The Gaussian approximation of data “0” and data “1”. (a) shows the Gaussian approximation of data “0” and (b) shows the Gaussian approximation of data “1”.

Fig. 10 The change of mean and standard deviation of normalized integrated intensity depending on the bandwidth. (1) shows the change of standard deviation of data “0”, (2) shows the change of mean of data “0”, (3) shows the change of standard deviation of data “1”, and (4) shows the mean of data “1”.

Fig. 11 (a) shows the relationship between the bandwidth and the bit error rate for several echo efficiencies(η). (1) is for $\eta=\eta_1$, (2) is for $\eta=2\eta_1$, (3) is for $\eta=3\eta_1$, (4) is for $\eta=4\eta_1$ where η_1 is the echo efficiency which can generated by $1.25e-17$ (Joule) of energy. (b) shows the relationship between the echo efficiency and the bit error rate for several bandwidths(BW). (1) is for $BW=1/\tau$, (2) is for $BW=2/\tau$, (3) is for $BW=3/\tau$, (4) is for $BW=4/\tau$, where τ is the data pulse width. The solid line shows the bit error rate calculated from the 3 pulse model and circles show the simulation results using a random data pulse train.

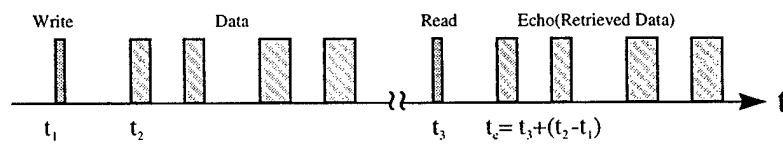


Fig.1 Conceptual view of time-domain optical storage. The write pulse prepares for the storage of the data pulses in the material. The data pulses are stored in the material in a Fourier transform domain. The read pulse recovers the data. Each retrieved data pulse is the convolution of the corresponding input data pulse and the correlation of the write and read pulses.

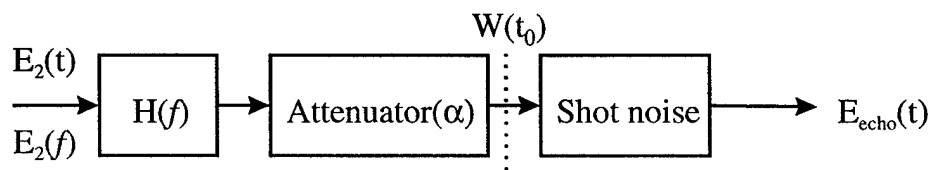


Fig. 2 System representation of the photon echo memory. $E_2(t)$ represents the data pulses, $H(f)$ represents the correlation between the write pulse and the read pulse and the attenuator represents the system's overall attenuation.

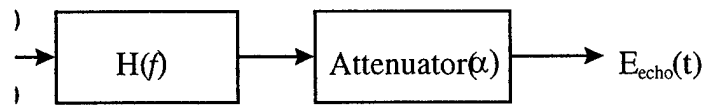


Fig.3 The noise analysis model for the photon echo memory system. $W(t_0)$ is the integrated intensity at the input of the photodetector. The shot noise is from the random interaction between a light and a photodetector.

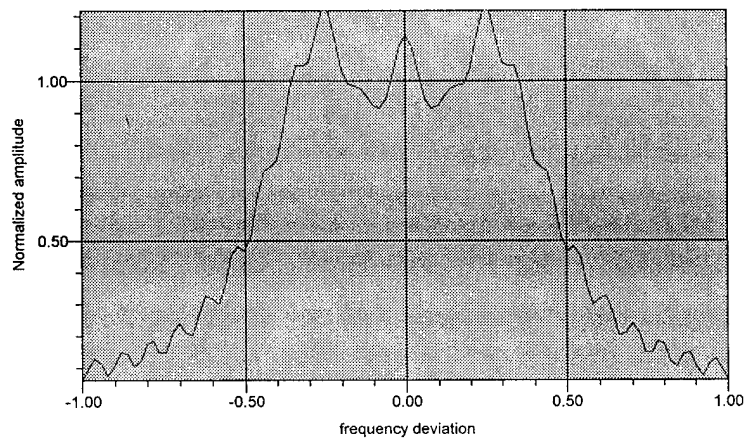


Fig.4. Spectral amplitude of a chirp signal for $D=12$. The x-axis shows the frequency offset from the center frequency, i.e., $(f-f_0)/\Delta f$. The dispersion factor is relatively small, and the curve is not very rectangular.

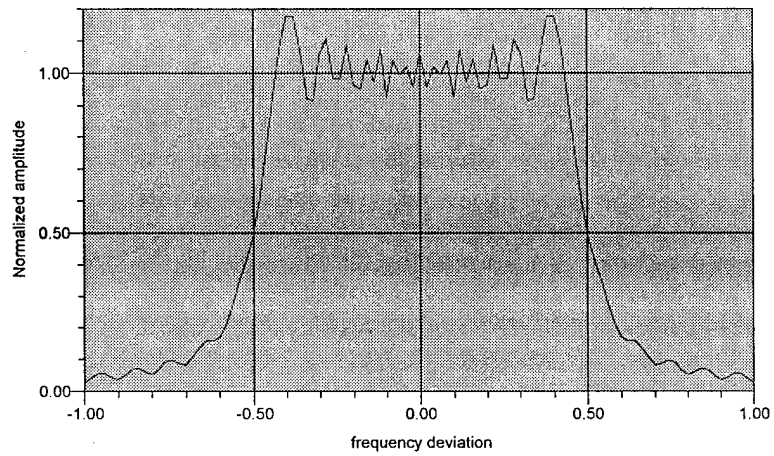


Fig.5 Spectral amplitude of a chirp signal for $D=60$. The x-axis again shows the frequency offset from the center frequency, i.e., $(f-f_0)/\Delta f$. This curve is more rectangular than Fig. 4.

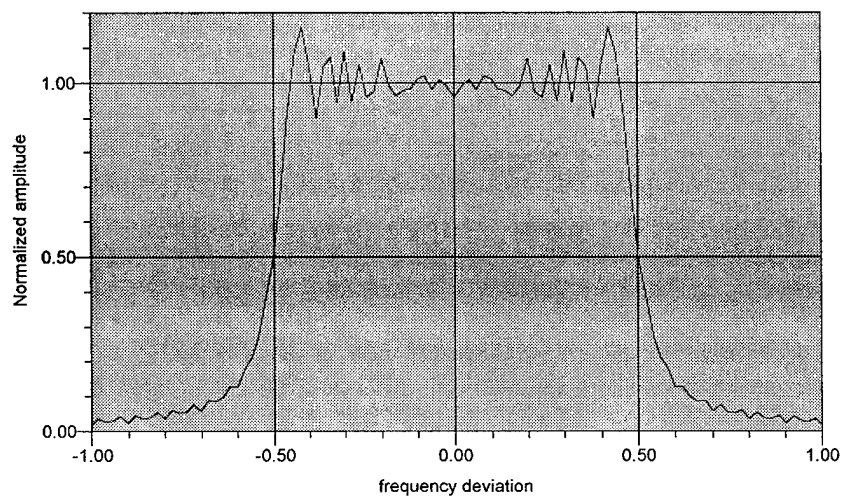


Fig. 6 Spectral amplitude of a chirp signal for $D=120$. The x-axis shows the frequency offset from the center frequency, i.e., $(f-f_0)/\Delta f$. This curve is now nearly rectangular.

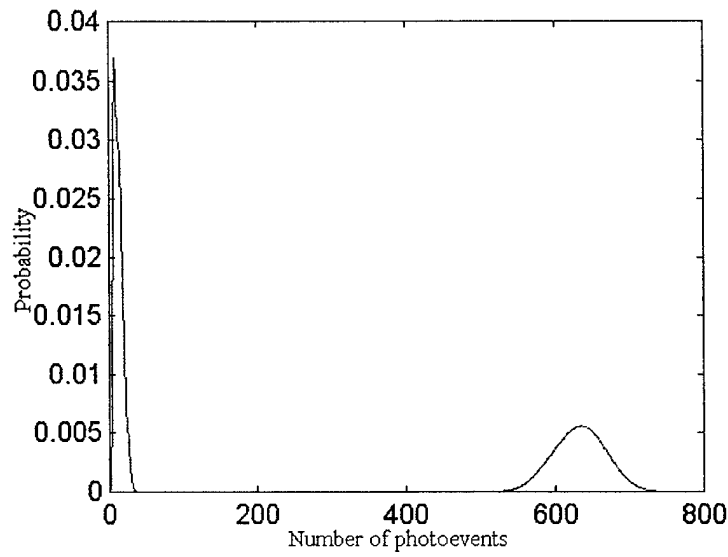


Fig. 7 The probability density function of the number of photoevents. The x-axis shows the number of photoevents and y-axis shows the probability for each number of photoevents. For the calculation, we used 5 nw output power, 50 nsec pulse width, 527.39 nm wavelength, quantum efficiency of detector of “1”.

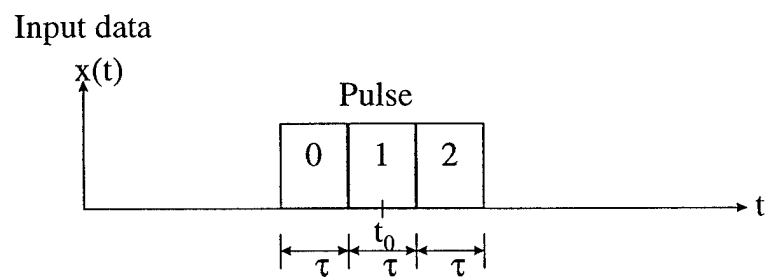
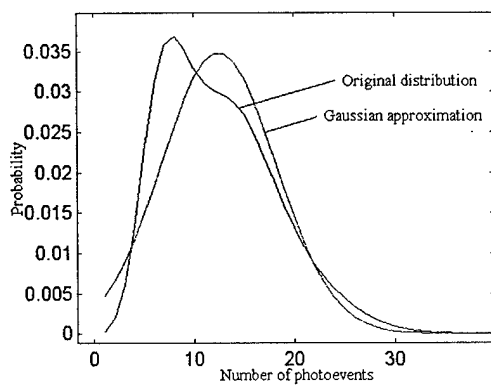


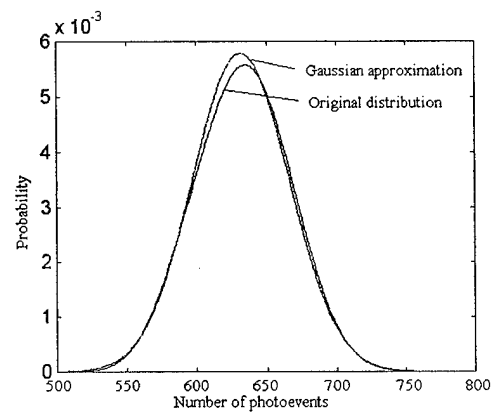
Fig. 8 The data pulse sequence for analysis of bandwidth effect

Table 1 The relationship between the bandwidth and integrated intensity

	000 (M_{00})	100 (M_{01})	001 (M_{02})	101 (M_{03})	010 (M_{10})	110 (M_{11})	011 (M_{12})	111 (M_{13})
$B=1/\tau$	0	0.0689	0.0689	0.0752	0.6060	0.8668	0.8668	1.0650
$B=2/\tau$	0	0.0179	0.0179	0.0410	0.8668	0.9291	0.9291	0.9966
$B=3/\tau$	0	0.0200	0.0200	0.0279	0.8877	0.9517	0.9517	1.0035
$B=4/\tau$	0	0.0104	0.0104	0.0228	0.9291	0.9634	0.9634	0.9997
$B=5/\tau$	0	0.0114	0.0114	0.0177	0.9351	0.9706	0.9706	1.0008
$B=6/\tau$	0	0.0073	0.0073	0.0157	0.9518	0.9754	0.9754	1.0000
$B=7/\tau$	0	0.0080	0.0080	0.0130	0.9545	0.9788	0.9788	1.0003
$B=8/\tau$	0	0.0056	0.0056	0.0119	0.9635	0.9815	0.9815	1.0000
$B=9/\tau$	0	0.0061	0.0061	0.0103	0.9650	0.9835	0.9835	1.0001
$B=\infty$	0	0	0	0	1.0	1.0	1.0	1.0



(a)



(b)

Fig. 9 The Gaussian approximation of data "0" and data "1". (a) shows the Gaussian approximation of data "0" and (b) shows the Gaussian approximation of data "1".

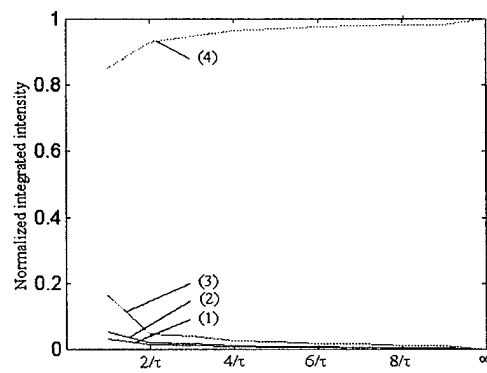
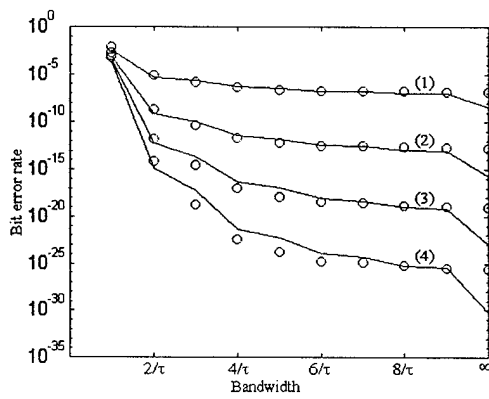
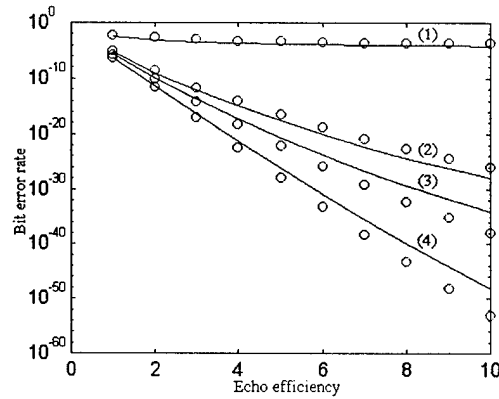


Fig. 10 The change of mean and standard deviation of normalized integrated intensity depending on the bandwidth. (1) shows the change of standard deviation of data "0", (2) shows the change of mean of data "0", (3) shows the change of standard deviation of data "1", and (4) shows the mean of data "1".



(a)



(b)

Fig. 11 (a) shows the relationship between the bandwidth and the bit error rate for several echo efficiencies(η). (1) is for $\eta=\eta_1$, (2) is for $\eta=2\eta_1$, (3) is for $\eta=3\eta_1$, (4) is for $\eta=4\eta_1$ where η_1 is the echo efficiency which can generated by $1.25e-17$ (Joule) of energy. (b) shows the relationship between the echo efficiency and the bit error rate for several bandwidths(BW). (1) is for $BW=1/\tau$, (2) is for $BW=2/\tau$, (3) is for $BW=3/\tau$, (4) is for $BW=4/\tau$, where τ is the data pulse width. The solid line shows the bit error rate calculated from the 3 pulse model and circles show the simulation results using a random data pulse train.

Relationship of laser frequency drift to bit error rate for a photon echo memory

Jin Y. Choi, John F. Walkup, Thomas F. Krile, and David J. Mehrl

*Optical Systems Laboratory, Electrical Engineering Dept.
Texas Tech University, Lubbock, Texas 79409-3102*

Telephone : (806) 742-3575
Fax : (806) 742-1245
E-mail : nus19@ttacs.ttu.edu

Abstract

In a photon echo memory, the temporal Fourier transform of the input data sequence from a light source emitting at a fixed wavelength is written into the recording medium's inhomogeneous absorption profile. To store and recall the input data faithfully, the Fourier transform of the input data sequence must be narrower than the medium's inhomogeneous bandwidth. This requirement sets an upper limit for the read-write data rate. In reality, however, the data storage density and data rates are further limited by errors associated with the storage and retrieval processes. For example, a real laser possesses imperfections such as temporal fluctuations in its spectral bandwidth and intensity. These characteristics produce noise which results in a degradation of the recovered signal. In particular, the frequency drift of a laser in conjunction with the system bandwidth negatively affects the recovery of the echo output signal. In this paper we analyze the relationship between frequency drift, system bandwidth, and the characteristics of the output signal using a statistical model. To characterize the memory's output characteristics, we employ the bit error rate as a performance measurement parameter.

Keywords : photon echo memory, frequency drift, noise model, bit error rate

1. Introduction

For investigating the photon echo memory mechanism, we assume laser pulses which have an electric field of the form¹

$$E_p(t - \eta_p) = \varepsilon_p(t - \eta_p) \cos [\omega_p(t - \eta_p) + \varphi_p] , \quad (1)$$

where $\eta_p = (n k_p \cdot r / c) + t_p$; n is the index of refraction of the material; $k_p \cdot r$ is the wave vector associated with the pulse; c is the speed of light in vacuum; t_p is the time at which the leading edge of the pulse reaches the arbitrary location $r = 0$; and φ_p is a constant phase factor. ε_p is the pulse function and ω_p is the laser's center radian frequency. For the ideal case, we assume that both the amplitude and the laser frequency are invariant. In fact, they are not invariant because of quantum mechanical limitations and experimental noise sources. The quantum mechanical limitations come from the particle nature of light and from spontaneous emission. Spontaneous emission occurs when an atom is in an excited state and is influenced by the vacuum field. This field generally has a random phase and therefore the emitted waves have random phases. In laser amplifiers, spontaneous emission places a lower bound on the amplitudes of signals which can be amplified without getting lost in the noise.

The analysis of the noise and the spectrum of the laser are well described in [2]. In reality, however, we must emphasize that the theoretical limits of the intensity fluctuations and linewidths don't necessarily correspond to the values commonly observed in the laboratory. The output of operational lasers is broadened mostly by thermal and acoustic fluctuations in the optical resonator length, which cause the resonant frequencies to shift about rapidly. The measurement of the actual amplitude fluctuations and frequency drift of the laser used for our photon echo experiments showed

that the amplitude fluctuations were small over the time scale of the writing process. Nevertheless, laser frequency drift can still be harmful when recovering data, as will be developed below.

In this paper, we analyzed the effect of the laser frequency fluctuations on the performance of a photon echo memory. To determine the effect of frequency drift on the recovered data, we first needed to know the distribution of the frequency drift. Previous analyses^{2,3} have shown that the lineshapes of lasers are between Gaussian and Lorentzian depending on the noise spectral density. Here, however, for our analysis we will assume a Gaussian lineshape for simplicity.

2. Frequency drift analysis

We have constructed a model for the analysis of the frequency drift as shown in Fig. 1. In a photon echo memory, the echo output signal is expressed as

$$E_{\text{echo}}(t) \propto \mathcal{F}^{-1}\{E_1^*(f) E_2(f) E_3(f)\} \quad (2)$$

where $E_1^*(f)$ is the complex conjugate of the spectrum of the write pulse, $E_2(f)$ is the spectrum of the data pulse, and $E_3(f)$ is the spectrum of the read pulse. When we consider the recovered data signal, we can simplify Eq. (2) by writing it as

$$E_{\text{echo}}(t) \propto \mathcal{F}^{-1}\{H(f) E_2(f)\} \quad (3)$$

where $H(f) = E_1^*(f)E_3(f)$ which we will call the system transfer function. In Fig. 1, $H(f)$ denotes the system transfer function resulting from the write/read pulses, $I(\xi, t_0)$ indicates the instantaneous intensity at time t_0 , $W(t_0)$ is the integrated intensity of the echo output, $p(W)$ is the probability density of the integrated intensity, and $P(K)$ is the probability of observing K photoevents at the output. In this model, we introduce a frequency drift in the data signal and find the distribution of the integrated intensity of the output signal. By comparing the amount of frequency drift and the distribution of the output signal, we can determine the effect of the frequency drift on the output characteristics such as

the bit error rate. The transfer function $H(f)$ is determined by the combination of write/read pulses. The transfer function was analyzed for the case where the write/read pulses were frequency chirped⁴. As far as the dispersion factor⁵ is large, usually greater than 100, the spectrum shape becomes nearly rectangular and we can assume that the transfer function is that of an ideal bandpass filter, that is

$$H(f) = \text{rect}\left(\frac{f - f_c}{B}\right) + \text{rect}\left(\frac{f + f_c}{B}\right), \quad (4)$$

where f_c is the center frequency of the filter and B is its bandwidth.

The echo output signal is integrated for the pulse interval in the second part of the system. Also, from the relationship between the frequency drift and the integrated intensity, we find the probability density function for the case where the frequency drift has certain distribution characteristics. In the third part, to consider the stochastic effect of the detector, we use Mandel's formula⁶ and find the probability density function of the number of photoevents.

Consider first the input data, which is a train of data pulses. The input data may be expressed as

$$x(t) = \sum_{i=1}^N x_i \cdot \text{rect}\left(\frac{t - t_i}{\tau}\right) \cdot \cos(2\pi f_i t). \quad (5)$$

Here N is the number of data pulses in the pulse train, x_i can be either "0" or "1", t_i shows the position of each data pulse, τ is the data pulse width, and f_i is the instantaneous laser frequency for the i^{th} data pulse. Here we assumed the frequency of the laser does not vary within the duration of a single data pulse, but may "drift" in frequency from pulse to pulse.

Now consider the rectangular input pulse. The spectrum of a rectangular input pulse has an infinite bandwidth, but the system has a finite bandwidth and the output signal thus has an infinite duration. This means that interference occurs between adjacent data pulses, i.e. we experience intersymbol interference⁷. Theoretically, the effect on an arbitrary pulse comes from all other pulses in the pulse train. In reality, the major effect comes from the adjacent pulses. We will concentrate here

only on the impact of the adjacent pulses (Fig. 2). We divide this into 4 cases for each kind of data (“0” and “1”). Table 1 shows the 8 cases for calculating the integrated intensity.

We will now find the relationship between frequency drift and integrated intensity for each case. We will then evaluate the probability density function (PDF) of the integrated intensity. For a sequence of three pulses, the input data sequence is expressed by

$$x(t) = x_0 \cdot \text{rect}\left(\frac{t - (t_0 - \tau)}{\tau}\right) \cdot \cos(2\pi f_0 t) + x_1 \cdot \text{rect}\left(\frac{t - t_0}{\tau}\right) \cdot \cos(2\pi f_1 t) \\ + x_2 \cdot \text{rect}\left(\frac{t - (t_0 + \tau)}{\tau}\right) \cdot \cos(2\pi f_2 t), \quad (6)$$

where x_0 , x_1 , and x_2 can individually be either “0” or “1” while f_0 , f_1 , and f_2 are the instantaneous frequencies for the 0, 1, and 2 data pulses, respectively.

For Case 1, the data pulse is expressed as

$$x(t) = \text{rect}\left(\frac{t - t_0}{\tau}\right) \cdot \cos(2\pi f_1 t), \text{ so that} \\ X(f) = \frac{1}{2} \tau \cdot \text{sinc}(\tau(f - f_1)) e^{-j2\pi(f - f_1)t_0} + \frac{1}{2} \tau \cdot \text{sinc}(\tau(f + f_1)) e^{-j2\pi(f + f_1)t_0}, \quad (7)$$

where $X(f)$ is the Fourier transform of the input data pulse. We assumed here that the system transfer function is an ideal bandpass filter, that is,

$$H(f) = \text{rect}\left(\frac{f - f_c}{B}\right) + \text{rect}\left(\frac{f + f_c}{B}\right), \quad (8)$$

where f_c is the center frequency, and B is the filter’s bandwidth.

From the input data and system transfer function, we now find the output given by

$$y(t) = \int_{-\infty}^{\infty} X(f) H(f) e^{j2\pi f t} df = \frac{1}{2} \left[\int_{\tau(f_c - f_1 - \frac{B}{2})}^{\tau(f_c - f_1 + \frac{B}{2})} \text{sinc}(u) e^{j2\pi \frac{u}{\tau}(t - t_0)} du + \int_{\tau(f_c - f_1 - \frac{B}{2})}^{\tau(f_c - f_1 + \frac{B}{2})} \text{sinc}(u) e^{-j2\pi \frac{u}{\tau}(t - t_0)} du \right]. \quad (9)$$

We ignore the phase of $y(t)$ because we are interested in the intensity. From the amplitude, we can calculate the integrated intensity by using the relationship

$$W(t_0) = \int_{t_0 - \frac{\tau}{2}}^{t_0 + \frac{\tau}{2}} y(t) y^*(t) dt, \quad (10)$$

where $y^*(t)$ denotes the complex conjugate of $y(t)$. By plugging Eq. (7) into Eq. (8), we obtain

$$W(t_0) = \frac{\tau}{2} \left[\int_{-L}^U \int_{-L}^U \text{sinc}(u) \text{sinc}(u') \text{sinc}(u + u') du' du + \int_{-L}^U \int_{-L}^U \text{sinc}(u) \text{sinc}(u') \text{sinc}(u - u') du' du \right], \quad (11)$$

where $L = \tau(f_c - f_1 - B/2)$ and $U = \tau(f_c - f_1 + B/2)$.

From Eq. (11), we can obtain the relationship between the frequency drift and the integrated intensity. Fig. 3 shows the relationship between the frequency drift and the integrated intensity for Case 1. The x-axis shows the frequency offset drift from the center frequency, i.e., $(f - f_c)/B$, and the y-axis shows the integrated intensity distribution normalized by the input pulse area.

By the same token, we can evaluate the integrated intensity for all cases in Table 1. Those results are summarized mathematically in the Appendix. For Case 2, the frequency drift has 2 arguments, $\Delta f_0 = f_c - f_0$, and $\Delta f_1 = f_c - f_1$. Fig. 4 shows the relationship between the frequency drift and the integrated intensity.

Figure 4 shows that the integrated intensity changes rapidly due to a frequency drift of pulse 1 but changes less due to a frequency drift of pulse 0. Case 3 has the same relationship between frequency drift and integrated intensity as Case 2 because the frequency drift of pulse 0 in Case 2 and pulse 2 in Case 3 contributes the same amount of integrated intensity to the pulse 1. Fig. 5 shows the relationship between frequency drift and integrated intensity for Case 6. The relationship between frequency drift and integrated intensity for Case 7 is the same as Case 6 because they have the same symmetry.

Now we know the relationship between integrated intensity and the frequency drift for each of the eight cases. If we know the distribution characteristics of the frequency drift, then, since we know the relationship between the frequency drift and the integrated intensity, we can find the distribution characteristics for the integrated intensity. The composite probability density of the integrated intensity can be calculated as:

$$P_w(w) = \sum_{i=1}^8 p(w|\text{case } i) \cdot p(\text{case } i) \quad (12)$$

If we assume all eight data sequence cases are equiprobable, then

$$P_w(w) = \frac{1}{8} \sum_{i=1}^8 p_i(w), \quad (13)$$

where $p_i(w)$ represents the probability density of the integrated intensity for the i^{th} case. We further assumed that the frequency drift obeys a Gaussian distribution. Thus, if we know the relationship between the frequency drift and the integrated intensity, we can calculate the probability density of the integrated intensity for each case. Now for Case 1, from Fig. (3), we can approximate the calculated value using a Gaussian curve. Fig. 6 shows the original data and the curve fitted using a Gaussian equation. In Fig. 6, frequency drift scale (x-axis) is normalized by $B/2$ where B denotes the bandwidth of the system. The integrated intensity is normalized by the input pulse area.

The circles in Fig. 6 indicate the real computation results and the approximation to the “data” curve fitted based on the model

$$W(t_0) = 0.8656 \cdot \exp\left(-\frac{\Delta f^2}{0.2129}\right). \quad (14)$$

Since earlier we assumed a Gaussian frequency drift, the probability density function of Δf is expressed by

$$p(\Delta f) = \frac{1}{\sqrt{2\pi}\sigma} \exp\left(-\frac{\Delta f^2}{2\sigma^2}\right). \quad (15)$$

Using a transformation of random variables⁸, we can show that the PDF of the integrated intensity corresponding to Eq. (14) is given by

$$p(w) = \frac{0.0981}{\sigma} \frac{\left(\frac{w}{0.8656}\right)^{\frac{0.2129}{2\sigma^2}-1}}{\sqrt{-0.2129 \cdot \ln\left(\frac{w}{0.8656}\right)}}, \quad 0 \leq w \leq 0.8656. \quad (16)$$

Using the same method, we can find the relationship between the frequency drift and the resulting integrated intensity for the other cases. Unfortunately, except for Cases 1 and 5, we could not determine a simple equation to represent the relationship between the frequency drift and the integrated intensity. For those cases, we numerically estimated the PDF relationship between the frequency drift and the integrated intensity. Based on those relationships, we can find the PDF of the total integrated intensity for a specific frequency drift. Fig. 7 presents an one example of PDF of integrated intensity for a frequency drift of $\sigma=0.05B$. The integrated intensity, as usual, is normalized by the input data pulse area.

In Fig. 7, the arrow at the “0” intensity indicates the PDF of a “0” integrated intensity and it came from the case in which all data pulses are “0”. The probability of “0” integrated intensity is 0.125 if we assume that all eight cases are equiprobable. Fig. 7 also shows that each data value has 3 peaks in its distribution. As was discussed earlier, Cases 2 and 3 for data “1” are symmetrical and Cases 6 and 7 for data “0” are symmetrical. These cases produce the peak probability for each data value and the other two cases (Cases 1 and 4 for data “1” and Cases 5 and 8 for data “0”) produce the smaller PDF peaks for each data value. That is why there are three peaks for each data value. If the frequency drift becomes smaller than the $\sigma=0.05B$ case shown in Fig. 7, the integrated intensity variation will become

smaller. On the other hand, if the frequency drift becomes larger, the integrated intensity variation will become larger and the PDF peaks for each data case will overlap.

3. Shot noise analysis

We now find the probability distribution of the photoevents, which is the output of the photodetector. When light having a deterministic variation of intensity over space and time is incident on a photodetector, the fluctuations of the photoevents obey Poisson statistics⁹. In this analysis, however, the light waves incident on the photosurface are random, and the probability of observing K detected photoevents can be expressed as

$$P(K) = \int_0^{\infty} P(K|W)p_w(W)dW = \int_0^{\infty} \frac{(\alpha W)^K}{K!} e^{-\alpha W} p_w(W)dW, \quad (17)$$

where $p_w(W)$ is the probability density function of the integrated intensity and α is the proportionality constant given by

$$\alpha = \frac{\gamma}{\hbar \bar{\nu}}. \quad (18)$$

Here γ is the quantum efficiency ($\gamma \leq 1$) which represents the average number of photoevents produced by each incident photon, \hbar is Planck's constant (6.626196×10^{-34} joule-sec), and $\bar{\nu}$ is the mean optical frequency of the radiation. This equation will serve as the basis for our calculations of photoevent statistics. It is called Mandel's formula after the individual who first derived it. The mean and variance of K are given by⁹

$$\bar{K} = \alpha \bar{W}, \quad \sigma_K^2 = \alpha \bar{W} + \alpha^2 \sigma_w^2 \quad (19)$$

Thus, if we know the probability of the integrated intensity, we can evaluate the probability of the photocounts at the detector.

As we can see from the previous analysis, the integrated intensity depends on the frequency drift and on the bandwidth of the system. In addition to those factors, the integrated intensity also depends on the echo efficiency of the system. Depending on the value of the echo efficiency, the characteristics and the number of detected photoevents can change significantly. To illustrate, we choose a minimum output power of 0.5 nW and assume an echo efficiency of η_1 which produces that amount of power at the output. Fig. 8 shows the typical distribution of the number of detected photoevents for various drifts, bandwidth, and echo efficiencies.

For the analysis of the output, it might be convenient to approximate the PDF by a known distribution. As we can see from Fig. 8, the distribution of the number of photoevents is different for each frequency drift, bandwidth and echo efficiency combination. In general, however, the data “0” distribution remains close to a Poisson distribution and the data “1” distribution remains close to a Gaussian distribution. To calculate the bit error rate, we used the Gaussian approximation to the Poisson distribution because it is more convenient and the inaccuracy resulting from the Gaussian approximation is small¹⁰. Fig. 9 shows the change of the mean and variance for specific values of frequency drift and various system bandwidth. The average number of photoevents for data “0” decreases as the system bandwidth increases and the standard deviation for data “0” also decreases with the increase of system bandwidth. For data “1”, the average number of photoevents increases as the system bandwidth increases but the standard deviation decreases with the increase of system bandwidth. Therefore, the bit error rate will decrease as the system bandwidth increase as we expect.

4. Bit error rate calculation

To calculate the bit error rate for each frequency drift, bandwidth and echo efficiency combination, we first calculate the mean and variance of the integrated intensity for the data “0” and data “1” cases. Because we know the relationship between the frequency drift, bandwidth and normalized integrated

intensity, if we know the frequency drift characteristics, bandwidth of the system and the real power of the output, we can then calculate the mean and variance of the data "0" and data "1" cases. Using a Gaussian approximation, the PDFs of the output distribution of detected photoevents can be expressed as

$$p_{\text{data}(0)}(k) = \frac{1}{\sqrt{2\pi\sigma_{k0}^2}} \exp\left(-\frac{(k - \bar{K}_0)^2}{2\sigma_{k0}^2}\right)$$

$$\text{and } p_{\text{data}(1)}(k) = \frac{1}{\sqrt{2\pi\sigma_{k1}^2}} \exp\left(-\frac{(k - \bar{K}_1)^2}{2\sigma_{k1}^2}\right), k = 0, 1, 2, \dots \quad (20)$$

where \bar{K}_0 is the mean of the number of photoevents for data "0", σ_{k0} is the standard deviation of the number of photoevents for data "0", \bar{K}_1 is the mean of the number of photoevents for data "1" and σ_{k1} is the standard deviation of data "1".

From Eq. (20), we can estimate the bit error rate for any combination of frequency drift, bandwidth and echo efficiency. Fig 10 shows the results of bit error rate calculations for several cases of frequency drift, system bandwidth, and echo efficiency. The solid line shows the bit error rate calculated from the three adjacent pulse model and the circles show the simulation results using a random data pulse train. Fig. 10 shows that the bit error rate is more dependent on the bandwidth than the frequency drift when the output signal is relatively small. With a relatively large output signal, the amount of frequency drift can affect the bit error rate considerably. Generally, the effect of the frequency drift on bit error rate is less than that of the bandwidth of the system.

5. Conclusion

In conclusion, we have formulated a laser frequency drift noise model and analyzed the relationship between the frequency drift, system bandwidth, and output noise characteristics. When the echo efficiency is small, the output is shot noise-limited. This means that the distribution is smoothed by the Poisson transformation (i.e. Mandel's formula). When the echo efficiency is large, the output is no

longer shot noise limited and its PDF resembles the original probability of the integrated intensity. Therefore, we can say that the effect of the Poisson transform on the probability density $p_W(W)$ is more significant when the number of photoevents is small and the effect decreases when the number of photoevents becomes larger. The average number of photoevents is directly related to the integrated intensity and is linearly proportional to the echo efficiency. The standard deviation increases more slowly than the average number of photoevents for both data values. When the echo efficiency is small, the distribution for data “0” is close to a Poisson distribution and the distribution for data “1” is close to a Gaussian distribution.

When we increase the echo efficiency, η , the analysis shows that the mean numbers of detected photoevents for both data values increase exactly at the same rate (for example, if we increase the echo efficiency 10 times, the means of both data values increase exactly 10 times), but the standard deviation increases with a lower rate. That means if we have a high echo efficiency system, we can obtain an improved system performance over the low echo efficiency system in terms of the bit error rate.

The authors gratefully acknowledge the support of this work by the Air Force Office of Scientific Research, USAF, under AFOSR Grant F49620-95-1-0140.

References

1. T. W. Mossberg, "Time-domain frequency-selective optical data storage", Optics Letters, Vol.7, No. 2, 1982, 77-79.
2. A. Yariv, Quantum Electronics, John Wiley & Sons, New York, 1989.
3. M. Zhu and J. L. Hall, "Stabilization of optical phase/frequency of a laser system: application to a commercial dye laser with an external stabilizer", J. Opt. Soc. Am., Vol. 10, No.5, 1993, 802-816.
4. J. Y. Choi, *Noise Modeling of a Photon Echo Memory* (Ph. D. dissertation, Texas Tech University, 1997)
5. J. R. Klauder, A. C. Price, S. Darlington, and W. J. Albersheim, "The theory and design of chirp radars," The Bell System Technical Journal, July 1960.
6. L. Mandel, Proc. Phys. Soc. (London), 74, 233 (1959).
7. F. G. Stremler, Introduction to Communication Systems, Addison Wesley, Reading, MA, 1990.
8. P. Z. Peebles, Jr., Probability, Random Variables, and Random Signal Principles, McGraw-Hill, Inc. New York, 1987.
9. J. W. Goodman, Statistical Optics, Wiley, New York, 1985.
10. G. Keiser, Optical Fiber Communications, McGraw-Hill, Inc. New York, 1991.

Appendix

In this appendix, we show the relationship between bandwidth, frequency drift and integrated intensity for all cases in Table 1.

For case 1,

$$W(t_0) = \frac{\tau}{2} \left[\int_{-L}^U \int_{-L}^U \text{sinc}(u) \text{sinc}(u') \text{sinc}(u + u') du' du + \int_{-L}^U \int_{-L}^U \text{sinc}(u) \text{sinc}(u') \text{sinc}(u - u') du' du \right], \quad (\text{A-1})$$

where $L = \tau(f_c - f_1 - B/2)$ and $U = \tau(f_c - f_1 + B/2)$.

For Case 2,

$$\begin{aligned} W(t_0) = & \frac{\tau}{2} \left\{ \text{Re} \int_{L_0}^{U_0} \int_{L_0}^{U_0} \text{sinc}(u) \text{sinc}(u') \text{sinc}(u + u') e^{j2\pi(u+u')} du' du \right. \\ & + \text{Re} \int_{L_1}^{U_1} \int_{L_1}^{U_1} \text{sinc}(v) \text{sinc}(v') \text{sinc}(v + v') e^{j2\pi(v+v')} dv' dv + \int_{L_0}^{U_0} \int_{L_0}^{U_0} \text{sinc}(u) \text{sinc}(u') \text{sinc}(u - u') e^{j2\pi(u-u')} du' du \\ & + \int_{L_1}^{U_1} \int_{L_1}^{U_1} \text{sinc}(v) \text{sinc}(v') \text{sinc}(v - v') e^{j2\pi(v-v')} dv' dv + 2 \cdot \text{Re} \int_{L_1}^{U_1} \int_{L_0}^{U_0} \text{sinc}(v) \text{sinc}(u') \text{sinc}(v + u') e^{-j2\pi u'} du' dv \\ & \left. + 2 \cdot \text{Re} \int_{L_0}^{U_0} \int_{L_1}^{U_1} \text{sinc}(u) \text{sinc}(v) \text{sinc}(u + v) e^{j2\pi u} dv du \right\} \end{aligned} \quad (\text{A-2})$$

where $L_0 = \tau(f_c - f_0 - B/2)$, $U_0 = \tau(f_c - f_0 + B/2)$, $L_1 = \tau(f_c - f_1 - B/2)$, $U_1 = \tau(f_c - f_1 + B/2)$ and Re denotes the real part of the integral.

For Case 3, one obtains

$$\begin{aligned} W(t_0) = & \frac{\tau}{2} \left\{ \text{Re} \int_{L_1}^{U_1} \int_{L_1}^{U_1} \text{sinc}(u) \text{sinc}(u') \text{sinc}(u + u') du' du \right. \\ & + \text{Re} \int_{L_2}^{U_2} \int_{L_2}^{U_2} \text{sinc}(v) \text{sinc}(v') \text{sinc}(v + v') e^{-j2\pi(v+v')} dv' dv + \int_{L_1}^{U_1} \int_{L_1}^{U_1} \text{sinc}(u) \text{sinc}(u') \text{sinc}(u - u') du' du \\ & + \int_{L_2}^{U_2} \int_{L_2}^{U_2} \text{sinc}(v) \text{sinc}(v') \text{sinc}(v - v') e^{-j2\pi(v-v')} dv' dv + 2 \cdot \text{Re} \int_{L_1}^{U_1} \int_{L_2}^{U_2} \text{sinc}(u) \text{sinc}(v') \text{sinc}(u - v') e^{j2\pi v'} dv' du \\ & \left. + 2 \cdot \text{Re} \int_{L_1}^{U_1} \int_{L_2}^{U_2} \text{sinc}(u) \text{sinc}(v) \text{sinc}(u + v) e^{-j2\pi u} dv du \right\} \end{aligned} \quad (\text{A-3})$$

where $L_1 = \tau(f_c - f_1 - B/2)$, $U_1 = \tau(f_c - f_1 + B/2)$, $L_2 = \tau(f_c - f_2 - B/2)$, $U_2 = \tau(f_c - f_2 + B/2)$.

For Case 4,

$$\begin{aligned}
W(t_0) = & \frac{\tau}{2} \left\{ \text{Re} \int_{L_0}^{U_0} \int \text{sinc}(u) \text{sinc}(u') \text{sinc}(u + u') e^{j2\pi(u+u')} du' du \right. \\
& + \text{Re} \int_{L_1}^{U_1} \int \text{sinc}(v) \text{sinc}(v') \text{sinc}(v + v') dv' dv + \text{Re} \int_{L_2}^{U_2} \int \text{sinc}(w) \text{sinc}(w') \text{sinc}(w + w') e^{-j2\pi(w+w')} dw' dw \\
& + \int_{L_0}^{U_0} \int \text{sinc}(u) \text{sinc}(u') \text{sinc}(u - u') e^{j2\pi(u-u')} du' du + \int_{L_1}^{U_1} \int \text{sinc}(v) \text{sinc}(v') \text{sinc}(v - v') dv' dv \\
& + \int_{L_2}^{U_2} \int \text{sinc}(w) \text{sinc}(w') \text{sinc}(w - w') e^{-j2\pi(w-w')} dw' dw + 2 \cdot \text{Re} \int_{L_0}^{U_0} \int_{L_1}^{U_1} \text{sinc}(u) \text{sinc}(v) \text{sinc}(u + v) e^{j2\pi uv} dv du \\
& + 2 \cdot \text{Re} \int_{L_0}^{U_0} \int_{L_2}^{U_2} \text{sinc}(u) \text{sinc}(w) \text{sinc}(u + w) e^{j2\pi(u-w)} dw du + 2 \cdot \text{Re} \int_{L_1}^{U_1} \int_{L_2}^{U_2} \text{sinc}(v) \text{sinc}(w) \text{sinc}(v + w) e^{-j2\pi vw} dw dv \\
& + 2 \cdot \text{Re} \int_{L_0}^{U_0} \int_{L_1}^{U_1} \text{sinc}(u) \text{sinc}(v') \text{sinc}(u - v') e^{j2\pi u} dv' du + 2 \cdot \text{Re} \int_{L_0}^{U_0} \int_{L_2}^{U_2} \text{sinc}(u) \text{sinc}(w') \text{sinc}(u - w') e^{j2\pi(u+w')} dw' dv \\
& \left. + 2 \cdot \text{Re} \int_{L_1}^{U_1} \int_{L_2}^{U_2} \text{sinc}(v) \text{sinc}(w') \text{sinc}(v - w') e^{j2\pi w'} dw' dv \right\} \quad (A-4)
\end{aligned}$$

where $L_0 = \tau(f_c - f_0 - B/2)$, $U_0 = \tau(f_c - f_0 + B/2)$, $L_1 = \tau(f_c - f_1 - B/2)$, $U_1 = \tau(f_c - f_1 + B/2)$, $L_2 = \tau(f_c - f_2 - B/2)$, $U_2 = \tau(f_c - f_2 + B/2)$.

For Case 5, because the data are all "0", the output is all "0". That is,

$$W(t_0) = 0 \quad (A-5)$$

For Case 6,

$$W(t_0) = \frac{\tau}{2} \left[\text{Re} \int_{L_0}^{U_0} \int \text{sinc}(u) \text{sinc}(u') \text{sinc}(u + u') e^{j2\pi(u+u')} du' du + \int_{L_0}^{U_0} \int \text{sinc}(u) \text{sinc}(u') \text{sinc}(u - u') e^{j2\pi(u-u')} du' du \right] \quad (A-6)$$

For Case 7,

$$\begin{aligned}
W(t_0) = & \frac{\tau}{2} \left[\text{Re} \int_{L_2}^{U_2} \int \text{sinc}(u) \text{sinc}(u') \text{sinc}(u + u') e^{-j2\pi(u+u')} du' du \right. \\
& \left. + \int_{L_2}^{U_2} \int \text{sinc}(u) \text{sinc}(u') \text{sinc}(u - u') e^{-j2\pi(u-u')} du' du \right]. \quad (A-7)
\end{aligned}$$

For Case 8,

$$\begin{aligned}
W(t_0) = & \frac{\tau}{2} \left\{ \operatorname{Re} \int_{L_0}^{U_0} \int_{L_0}^{U_0} \operatorname{sinc}(u) \operatorname{sinc}(u') \operatorname{sinc}(u + u') e^{j2\pi(u+u')} du' du \right. \\
& + \int_{L_2}^{U_2} \int_{L_2}^{U_2} \operatorname{sinc}(w) \operatorname{sinc}(w') \operatorname{sinc}(w + w') e^{-j2\pi(w+w')} dw' dw + \int_{L_0}^{U_0} \int_{L_0}^{U_0} \operatorname{sinc}(u) \operatorname{sinc}(u') \operatorname{sinc}(u - u') e^{j2\pi(u-u')} du' du \\
& + \int_{L_2}^{U_2} \int_{L_2}^{U_2} \operatorname{sinc}(w) \operatorname{sinc}(w') \operatorname{sinc}(w - w') e^{-j2\pi(w-w')} dw' dw + 2 \cdot \operatorname{Re} \int_{L_0}^{U_0} \int_{L_2}^{U_2} \operatorname{sinc}(u) \operatorname{sinc}(w') \operatorname{sinc}(u - w') e^{j2\pi(u+w')} dw' du \\
& \left. + 2 \cdot \operatorname{Re} \int_{L_0}^{U_0} \int_{L_2}^{U_2} \operatorname{sinc}(u) \operatorname{sinc}(w) \operatorname{sinc}(u + w) e^{j2\pi(u-w)} dw du \right\}.
\end{aligned} \tag{A-8}$$

Figure Captions

Fig. 1 Noise model due to laser frequency drift.

Fig. 2 The data pulse sequence for analysis of frequency drift noise

Table 1. The eight input pulse permutations for 3 adjacent pulses

Fig. 3 Relationship between integrated intensity and frequency drift for Case 1.

Fig. 4 Relationship between integrated intensity and frequency drift for Case 2.

Fig. 5 Relationship between integrated intensity and frequency drift for Case 6

Fig. 6 Curve fitting for Case 1.

Fig. 7 Probability density function of the integrated intensity for a specific frequency drift ($\sigma=0.05B$ where B is the bandwidth).

Fig. 8 Some typical distributions for the number of detected photoevents.

Fig. 9 The variation of the mean and standard deviation of the detected photoevents for several bandwidths (standard deviation of frequency drift=2 MHz).

Fig. 10 (a) Relationship between the frequency drift and BER for several bandwidths, (b) relationship between the frequency drift and BER for several echo efficiencies. (1) is for bandwidth= $1/\tau$, (2) is for bandwidth= $2/\tau$, (3) is for bandwidth= $3/\tau$, (4) is for bandwidth= $4/\tau$, where τ is the pulse width, which is 50 nsec (1) $\eta=\eta_1$, (2) $\eta=2\eta_1$, (3) $\eta=3\eta_1$, (4) $\eta=4\eta_1$, where η_1 is the echo efficiency which can generated by $2.5e-17$ (Joule) of energy.

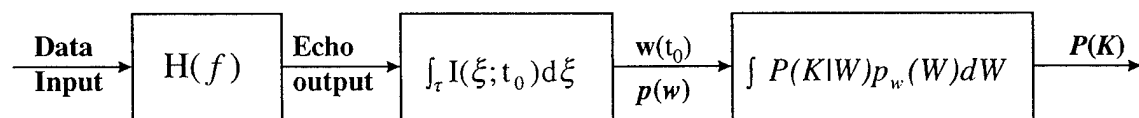


Fig. 1 Noise model due to laser frequency drift.

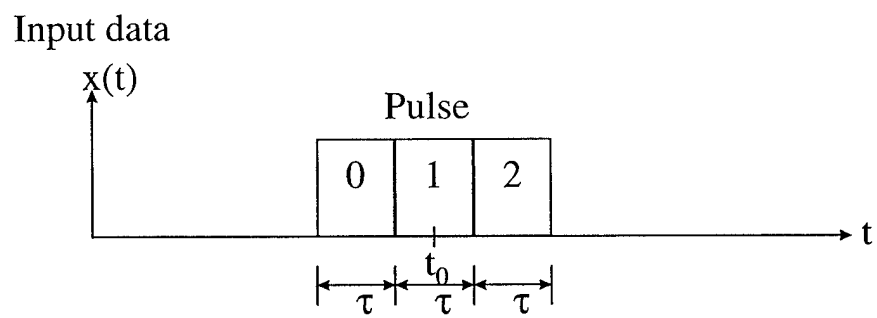


Fig. 2 The data pulse sequence for analysis of frequency drift noise

Case	Pulse 0	Pulse 1	Pulse 2	Case	Pulse 0	Pulse 1	Pulse 2
1	0	1	0	5	0	0	0
2	1	1	0	6	1	0	0
3	0	1	1	7	0	0	1
4	1	1	1	8	1	0	1

Table 1. The eight input pulse permutations for 3 adjacent pulses

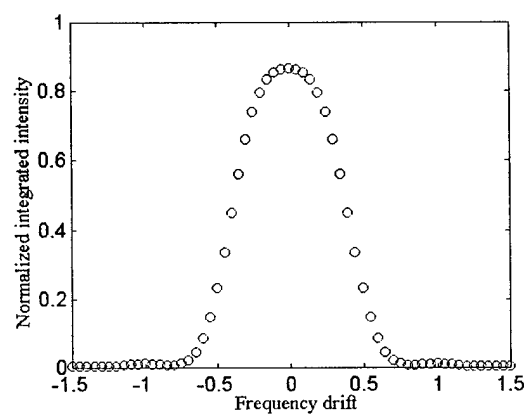


Fig. 3 Relationship between integrated intensity and frequency drift for Case 1.

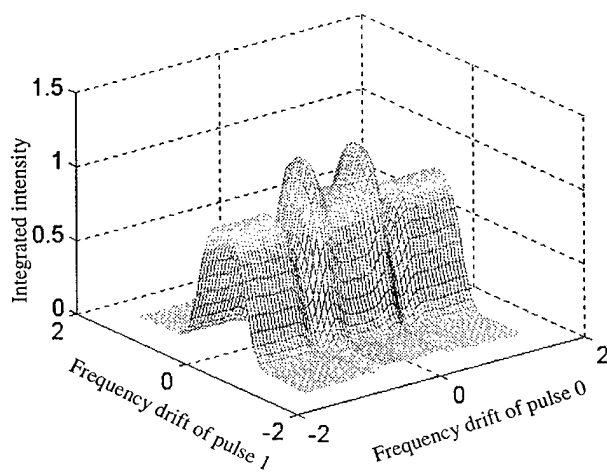


Fig. 4 Relationship between integrated intensity and frequency drift for Case 2.

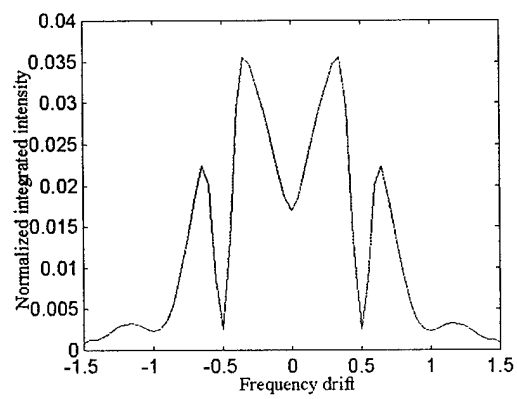


Fig. 5 Relationship between integrated intensity and frequency drift for Case 6

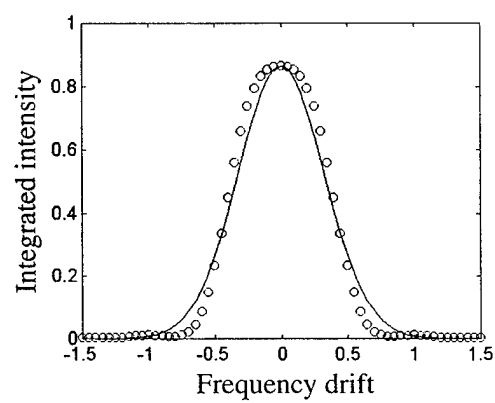


Fig. 6 Curve fitting for Case 1.

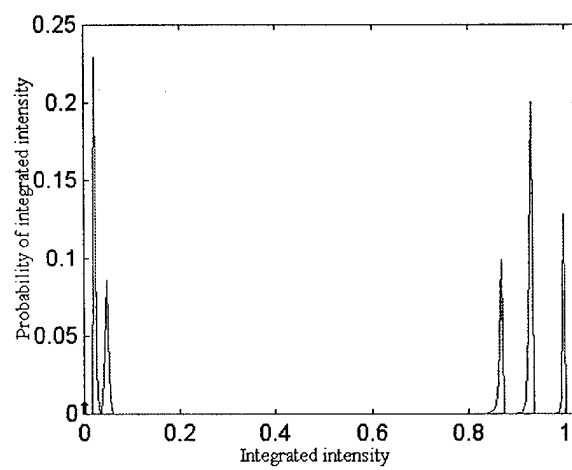
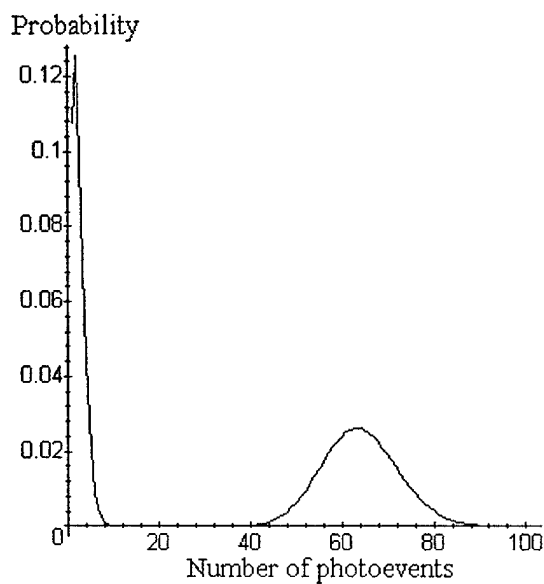
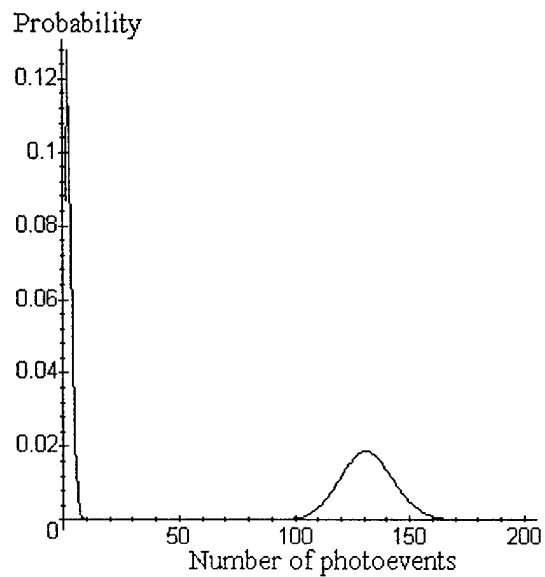


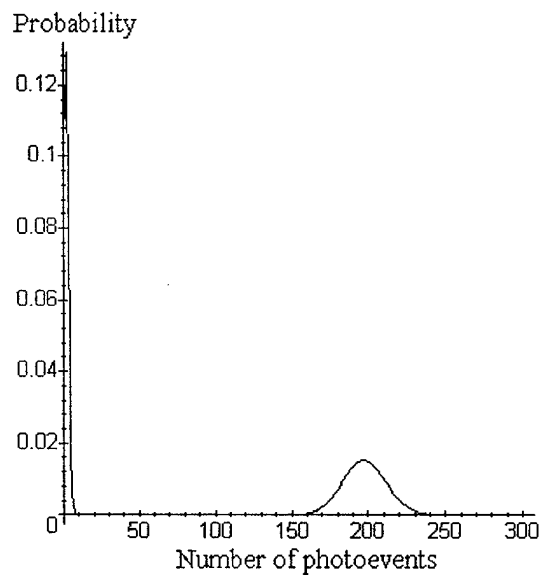
Fig. 7 Probability density function of the integrated intensity for a specific frequency drift
 $(\sigma=0.05B$ where B is the bandwidth).



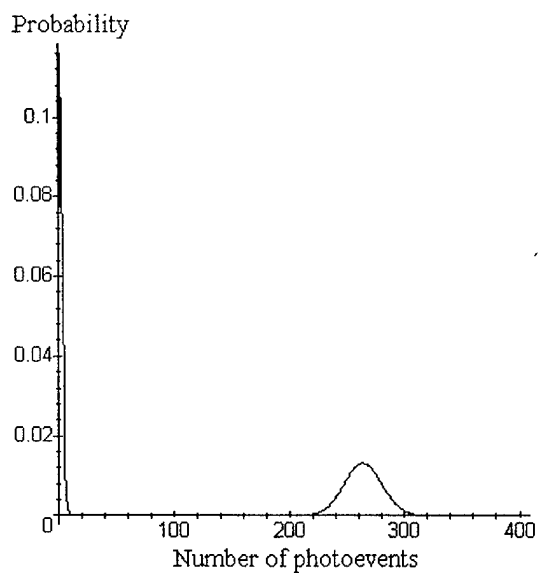
(a) Drift=1.5 Mhz, B=40 MHz, $\eta=\eta_1$



(b) Drift=2 MHz, B=60MHz, $\eta=2\eta_1$

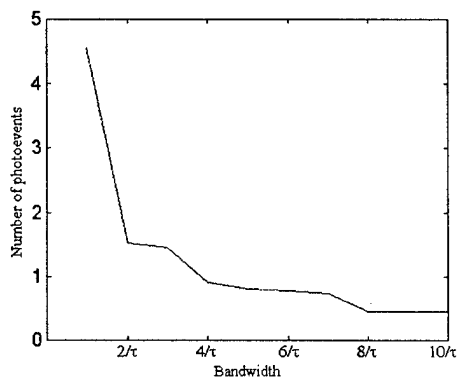


(c) Drift=2.5 Mhz, B=80MHz, $\eta=3\eta_1$

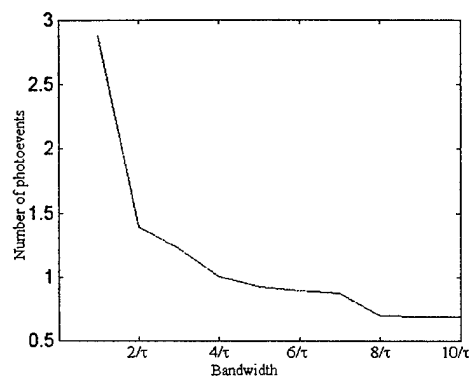


(d) Drift=3 MHz, B=100 MHz, $\eta=4\eta_1$

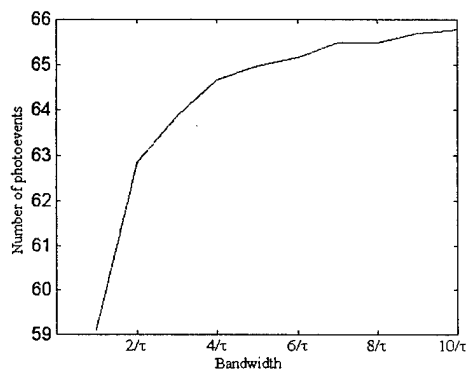
Fig. 8 Some typical distributions for the number of detected photoevents.



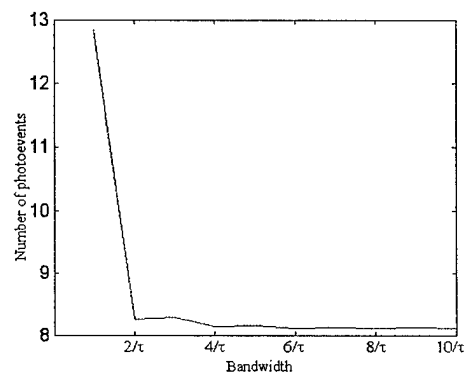
(a) Mean of data "0"



(b) Standard deviation of data "0"

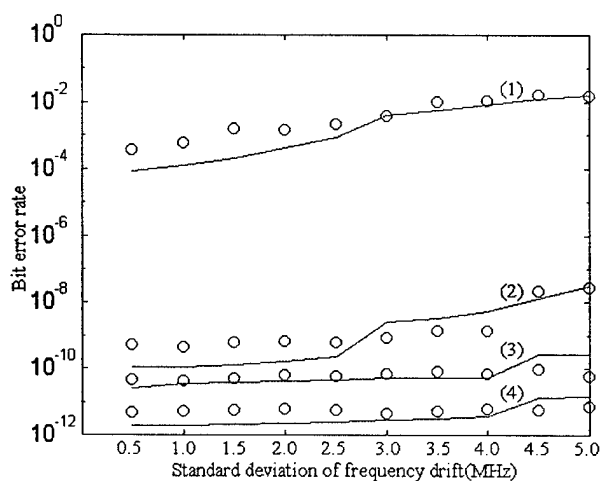


(c) Mean of data "1"

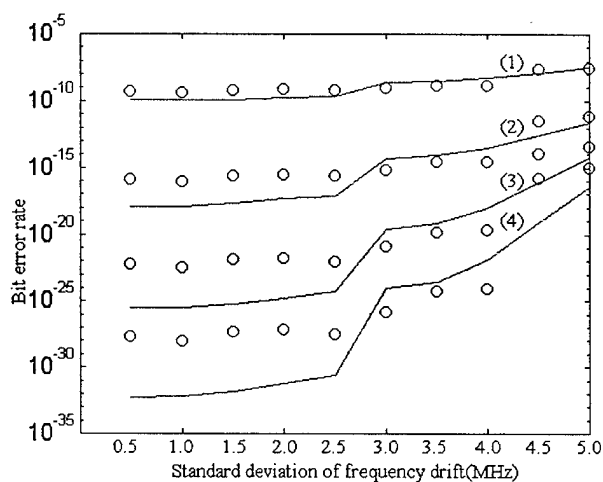


(d) Standard deviation of data "1"

Fig. 9 The variation of the mean and standard deviation of the detected photoevents for several bandwidths (standard deviation of frequency drift=2 MHz).



(a)



(b)

Fig. 10 (a) Relationship between the frequency drift and BER for several bandwidths, (b) relationship between the frequency drift and BER for several echo efficiencies. (1) is for bandwidth= $1/\tau$, (2) is for bandwidth= $2/\tau$, (3) is for bandwidth= $3/\tau$, (4) is for bandwidth= $4/\tau$, where τ is the pulse width, which is 50 nsec (1) $\eta=\eta_1$, (2) $\eta=2\eta_1$, (3) $\eta=3\eta_1$, (4) $\eta=4\eta_1$, where η_1 is the echo efficiency which can be generated by $2.5e-17$ (Joule) of energy.

Bit error rates for a photon echo memory

J. Y. Choi, J. F. Walkup, T. F. Krile, and D. J. Mehrl

Texas Tech University, Department of Electrical Engineering, Lubbock, Texas 79409

ABSTRACT

The noise characteristics of the photon echo memory have been investigated. The photon echo memory has the ability to store many bits of information in a diffraction-limited spot, thereby dramatically increasing the storage density. The temporal Fourier transform of the input data sequence is written into the inhomogeneous absorption profile of the recording medium. Data are encoded by means of temporal modulation onto the waveform of a finite duration data beam. Individual bits are not localized to a specific spectral channel; instead, they are stored throughout a region of spectral-addressing space. In order to store and recall the input data accurately, the Fourier transform of the input data sequence must be narrower than the inhomogeneous bandwidth.

In the photon echo memory mechanism, there are several factors affecting the system bit error rate such as finite-width write/read pulses, echo efficiency, shot noise, thermal noise, etc. The accuracy of the echo output depends on those system factors. In this paper we formulate a simple model of the photon echo system, and by analyzing this model we derive the relationship between the characteristics of the echo output signal and several factors such as the bandwidth of the system, echo efficiency, atom excited state population fluctuations, shot noise, and thermal noise.

Keywords: photon echo memory, optical data storage, atom population fluctuation, shot noise, thermal noise, bit error rate

1. INTRODUCTION

A photon echo memory¹, also known as TDOS(Time Domain Optical Storage)², time-domain FSDS(Frequency Selective Data Storage)¹, CTDOM(Coherent Time-Domain Optical Memory)³, and TDOM(Time Domain Optical Memory)⁴, offers the potential of ultrahigh storage density and ultrahigh data throughput rates³. A photon echo memory stores information in the spectral domain of an inhomogeneously broadened absorbing material in addition to the spatial addresses used in conventional two-dimensional optical memories. In a photon echo memory, the temporal Fourier transform of the input data sequence from a light source emitting at a fixed frequency is written into the inhomogeneous absorption profile. To store and recall the input data faithfully, the bandwidth of the input data sequence must, therefore, be narrower than the inhomogeneous bandwidth. This requirement on the Fourier transform of the input data sequence sets an upper limit for the photon echo memory read-write data rate that essentially equals the inhomogeneous bandwidth of the material.

In the photon echo process, various noise sources and distortions will unavoidably be introduced which can lead to errors in the interpretation of the received signal. Some of them come from the limitation of current technology and others come from fundamental limitations in the photon echo process. In the photon echo process, the most important factors which affect the echo output signal are system bandwidth (which arises from the write/read pulses), echo efficiency (which is defined by the ratio of the power of the output echo signal to that of the input signal), statistical excited state population fluctuations⁵ (defined as the variations in the local environment of the atom storage centers), shot noise (fundamental detector noise), and thermal noise (post-detector electronics noise). In this paper, we analyze the effect of each of these factors on the bit error rate of the output signal.

2. ANALYSIS

2.1 Photon echo process

The ideal noiseless echo output signal is expressed as

$$E_{\text{echo}}(t) \propto \mathcal{F}^{-1}\{E_1^*(\omega) E_2(\omega) E_3(\omega)\}, \quad (1)$$

where $E_{\text{echo}}(t)$ represents the echo output signal, \mathcal{F}^{-1} represents the inverse Fourier transform, $E_1^*(\omega)$ represents the complex conjugate of the Fourier transform of the write pulse, $E_2(\omega)$ represents the Fourier transform of the data pulses, and $E_3(\omega)$ represents the Fourier transform of the read pulse.

In reality, this ideal echo output signal is contaminated with noise which is generated by the statistical excited state population fluctuations. In the photon echo process, when the material is exposed to laser pulses, the excited state population of atoms is modulated according to the Fourier spectrum of the pulses and the information about the pulses is stored in a population grating. As we described before, under ideal conditions the population grating is exactly proportional to the Fourier transform of the input pulses. However, such an ideal condition does not exist, and there will be fluctuations in the atom population. This fundamental source of noise imposes a limit on the achievable storage density for a given concentration of storage centers. The photon echo process including the noise source from the atom fluctuations is shown in Fig. 1.

Thus, when we include the noise component from the atom fluctuations, the echo output will be

$$E_{\text{echo}}(t) = \mathcal{F}^{-1}\{E_1^*(\omega)E_2(\omega)E_3(\omega)\} + \mathcal{F}^{-1}\{N(\omega)\} \\ = E_1(t) \oplus E_2(t) * E_3(t) + X(t) + j Y(t), \quad (2)$$

where \oplus denotes correlation, $*$ denotes convolution, $N(\omega)$ denotes the noise component from the atom fluctuations, $X(t)$ represents the real noise component in the time domain, j represents the imaginary operator, and $Y(t)$ represents the imaginary noise component in the time domain. The effects of convolution and correlation on the data signal are to 1) smooth the output signal, and 2) increase the pulse width. When the pulse widths of the write/read and data pulses are all the same, say τ , the output pulse will be 3τ in width. This means the output signal will cause intersymbol interference to the two adjacent pulses on each side.

On the other hand, if the write/read pulse widths are $\frac{1}{2}\tau$, where τ is the data pulse width, then the intersymbol interference will affect only the adjacent pulses. Generally, in the photon echo process, we assume that the write/read pulses are very short compared to the data pulse, so we will assume that the intersymbol interference only affects the adjacent output signals. Fig. 2 shows the effects of convolution and correlation on the output signal.

Now consider the data pulse train which is stored using the photon echo process. When we think about the data pulse which is "0" or "1", there are, effectively, three situations. That is, (1) both adjacent data pulses are "0", (2) one of adjacent data pulses is "1", (3) both of the adjacent data pulses are "1". For each case, the first term of Eq. (3) will have different values. The noise component in the time domain is the inverse Fourier transform of $N(\omega)$. Analysis⁶ has shown that when the atom fluctuation is Gaussian, or uniform-distributed, the noise components in the time domain for the echo output signal are each infinite sums of Gaussian noises with different variances. From the Central Limit Theorem⁷, we can say that $X(t)$ and $Y(t)$ are also Gaussian distributed with zero mean. The variance of the noise in the time domain will be determined by the atom fluctuations and the read pulse width. Therefore, the output is composed of a constant plus Gaussian noise. The constant value is dependent on the data position and its adjacent data.

$$\begin{aligned} E_{\text{echo}}(t) &= \mathcal{F}^{-1}\{N(\omega)\} = X(t) + j Y(t) && \text{or} \\ E_{\text{echo}}(t) &= a(t) + \mathcal{F}^{-1}\{N(\omega)\} = a(t) + X(t) + j Y(t) && \text{or} \\ E_{\text{echo}}(t) &= b(t) + \mathcal{F}^{-1}\{N(\omega)\} = b(t) + X(t) + j Y(t) && \text{when the data}=0, \text{ and} \\ E_{\text{echo}}(t) &= c(t) + \mathcal{F}^{-1}\{N(\omega)\} = c(t) + X(t) + j Y(t) && \text{or} \\ E_{\text{echo}}(t) &= d(t) + \mathcal{F}^{-1}\{N(\omega)\} = d(t) + X(t) + j Y(t) && \text{or} \\ E_{\text{echo}}(t) &= 1 + \mathcal{F}^{-1}\{N(\omega)\} = 1 + X(t) + j Y(t) && \text{when the data}=1, \end{aligned} \quad (3)$$

where a , b , c , and d are determined by the relationship between the pulse width of the data and that of the read/write pulses. "a" is for data "0" when one of the adjacent pulses is "1", "b" is for data "0" when both of the adjacent pulses are "1", "c" is for data "1" when both of the adjacent pulses are "0", and "d" is for data "1" when one of the adjacent pulses is "0". Those values are determined by the system bandwidth and echo efficiency. The one thing we need to mention is the probability of occurrence of each special case. The probability of having one adjacent "1" is twice as large as the probability of having no adjacent "1"s or all adjacent "1"s. Therefore, we have to take into account these probabilities when we calculate the PDF of the power distribution.

The echo output signal is detected by using a photodetector and related post-detector electronics. For the detection of the echo output signal, we assume the case of using IM/DD(Intensity Modulation/Direct Detection). When the variance of the real

and imaginary time domain noise components are $\sigma^2/2$, the PDF of the power is calculated as in Eq. (5). Here we assumed that the value "a" is related to the case of having one adjacent "1" for data "0" and the value "d" is related to the case of having one adjacent "1" for data "1". Again, the relationship between the frequency domain noise and the time domain noise variance is determined by the pulse width.

$$f_P(p) = \frac{1}{4\sigma^2} \left\{ e^{-\frac{p}{\sigma^2}} + 2e^{-\frac{p+a^2}{\sigma^2}} I_0\left(\frac{2a\sqrt{p}}{\sigma^2}\right) + e^{-\frac{p+b^2}{\sigma^2}} I_0\left(\frac{2b\sqrt{p}}{\sigma^2}\right) \right\} \{P \geq 0\} \quad \text{for data="0",}$$

$$f_P(p) = \frac{1}{4\sigma^2} \left\{ e^{-\frac{p+c^2}{\sigma^2}} I_0\left(\frac{2c\sqrt{p}}{\sigma^2}\right) + 2e^{-\frac{p+d^2}{\sigma^2}} I_0\left(\frac{2d\sqrt{p}}{\sigma^2}\right) + e^{-\frac{p+1}{\sigma^2}} I_0\left(\frac{2\sqrt{p}}{\sigma^2}\right) \right\}, \{P \geq 0\} \text{ for data="1".} \quad (5)$$

where $F_P(p)$ is the PDF of the echo output signal and I_0 is a Modified Bessel function of order zero. The mean and variance for the data "0" and data "1" cases are, respectively,

$$E[P_0] = \frac{a^2}{2} + \frac{b^2}{4} + \sigma^2 \quad \text{for data=0,}$$

$$E[P_1] = \frac{1}{4} + \frac{c^2}{4} + \frac{d^2}{2} + \sigma^2 \quad \text{for data=1.} \quad (6)$$

Therefore, the average power at time t is a function of a , b , and σ for data "0", and c , d and σ for data "1". The constants "a", "b", "c" and "d" are determined by the system bandwidth and echo efficiency and σ is determined by the atom fluctuations.

2.2 Optical receiver

The echo output signal is detected by an optical receiver. A typical optical receiver, whose schematic diagram includes the noise components, is shown in Fig. 3. The three basic stages of the receiver are a photodetector, amplifier, and equalizer. The photodetector can be either an avalanche photodiode with a mean gain M or a *pin* photodiode for which $M=1$. The photodiode has quantum efficiency η and capacitance C_d . The detector has a bias resistor (resistance R_b) which generates a thermal noise current $i_b(t)$.

The amplifier has an input impedance represented by the parallel combination of a resistance R_A and a shunt capacitance C_A . Voltages appearing across this impedance cause current to flow in the amplifier output. This amplifying function is represented by the voltage-controlled current source which is characterized by a *transconductance* g_m . There are two amplifier noise sources. The input noise current source $i_A(t)$ arises from the thermal noise of the amplifier input resistance R_A , whereas the noise voltage source $e_A(t)$ represents the thermal noise of the amplifier channel. These noise sources are assumed Gaussian in their statistics, flat in spectrum (which characterizes white noise), and uncorrelated (statistically independent). They are thus completely described by their noise spectral densities⁹. The equalizer that follows the amplifier is normally a linear frequency-shaping filter that is used to mitigate the effects of signal distortion and intersymbol interference.

At time t the mean output current from the photodiode resulting from the echo output signal is

$$\langle i(t) \rangle = \frac{\eta q}{h\nu} M \langle P(t) \rangle = R_0 M \langle P(t) \rangle, \quad (7)$$

where η is the quantum efficiency (i.e. the number of electron-hole carrier pairs generated per incident photon of energy $h\nu$), and R_0 is the photodiode responsivity. This current is then amplified and filtered to produce a mean voltage at the output of the equalizer given by the convolution of the current with the amplifier impulse response

$$\langle v_{out}(t) \rangle = AR_0 M \langle P(t) \rangle * h_B(t) * h_{eq}(t) = R_0 G \langle P(t) \rangle * h_B(t) * h_{eq}(t). \quad (8)$$

Here A is the amplifier gain, we define $G=AM$ for brevity, $h_B(t)$ is the impulse response of the bias circuit, $h_{eq}(t)$ is the equalizer impulse response, and $*$ denotes convolution.

We now calculate the noise voltages or, equivalently, the noise currents. If $v_M(t)$ is the noise voltage causing $v_{out}(t)$ to deviate from its average value, then the actual equalizer output voltage is of the form

$$v_{out}(t) = \langle v_{out}(t) \rangle + v_M(t). \quad (9)$$

The noise voltage at the equalizer output can be represented by

$$v_N^2(t) = v_s^2(t) + v_R^2(t) + v_f^2(t) + v_E^2(t), \quad (10)$$

where $v_s(t)$ is the quantum (or shot) noise resulting from the random Poisson nature of the photocurrent $i_s(t)$ produced by the photodetector, $v_R(t)$ is the thermal (or Johnson) noise associated with the bias resistor R_b , $v_A(t)$ results from the amplifier input noise current source $i_A(t)$, and $v_E(t)$ results from the amplifier input voltage noise source $e_A(t)$. Here, we are interested in the mean square voltage $\langle v_N^2 \rangle$, which is given by

$$\begin{aligned} \langle v_N^2 \rangle &= \langle [v_{out}(t) - \langle v_{out}(t) \rangle]^2 \rangle = \langle v_{out}^2(t) \rangle - \langle v_{out}(t) \rangle^2 \\ &= \langle v_s^2(t) \rangle + \langle v_R^2(t) \rangle + \langle v_A^2(t) \rangle + \langle v_E^2(t) \rangle. \end{aligned} \quad (11)$$

Personick⁹ carried out a detailed analysis that evaluated the shot noise as a function of time within the bit slot. This results in an accurate estimate of the shot noise contribution to the equalizer output noise voltage, but at the expense of computational difficulty. Smith and Garrett¹⁰ subsequently proposed a simplification of Personick's expressions by relating the mean square shot noise voltage $\langle v_s^2(t) \rangle$ at the decision time to the average unit gain photocurrent $\langle i_0 \rangle$ over the bit time T_b through the shot noise expression¹¹

$$\langle v_s^2(t) \rangle = 2q \langle i_0 \rangle \langle m^2 \rangle B_N R^2 A^2, \quad (12)$$

where $\langle m^2 \rangle$ is the mean square avalanche gain, which has the form M^{2+x} with $0 < x \leq 1.0$, B_N is the noise equivalent bandwidth of the bias circuit, amplifier, and equalizer defined for positive frequencies only¹², A is the amplifier gain and R is the total resistance of the parallel combination of R_b and R_A , that is

$$R = \frac{R_A R_b}{R_A + R_b}. \quad (13)$$

We now calculate the mean unity-gain photocurrent $\langle i_0 \rangle$ over the bit-time. In Eq. (6), we found the average power at time t for pulse "0" and pulse "1". Because constants a , b , c , and d are directly related to the ratio of write/read pulse and data pulse widths and echo efficiency, and σ is related to the atom fluctuations, we see that the mean unity-gain photocurrent $\langle i_0 \rangle$ is also related to the system bandwidth, echo efficiency, and atom fluctuations. From Eq. (6), we can calculate the mean unity-gain photocurrent as

$$\begin{aligned} \langle i_0 \rangle_0 &= \frac{\eta q}{h\nu} \frac{1}{T_b} \int_{-T_b/2}^{T_b/2} E[P_0] dt \quad \text{for data=0, and} \\ \langle i_0 \rangle_1 &= \frac{\eta q}{h\nu} \frac{1}{T_b} \int_{-T_b/2}^{T_b/2} E[P_1] dt \quad \text{for data=1.} \end{aligned} \quad (14)$$

B_N is calculated from the bias circuit, amplifier, and equalizer as¹²

$$B_N = \frac{1}{|H_B(0)H_{eq}(0)|^2} \int_0^\infty |H_B(f)H_{eq}(f)|^2 df. \quad (15)$$

Therefore, once we know the system bandwidth and echo efficiency, we can estimate the mean unity-gain photocurrent $\langle i_0 \rangle$ and the shot noise component for the data = "0" and data = "1" cases.

The first thermal noise term of Eq. (11) at the output of the equalizer is¹²,

$$\langle v_R^2(t) \rangle = \frac{4k_B T}{R_b} B_N R^2 A^2, \quad (16)$$

where $k_B T$ is Boltzmann's constant times the absolute temperature. Since the thermal noise contributions from the amplifier input noise current source $i_A(t)$ and from the amplifier input noise voltage source $e_A(t)$ are assumed to be Gaussian and independent, they are completely characterized by their noise spectral densities¹². Thus, the last two noise terms are

$$\langle v_A^2(t) \rangle = S_I B_N R^2 A^2 \quad (17)$$

and

$$\langle v_E^2(t) \rangle = S_E B_e A^2 \quad (18)$$

where S_I is the spectral density of the amplifier input noise current source, S_E is the spectral density of the amplifier noise voltage source, and

$$B_e = \frac{1}{|H_{eq}(0)|^2} \int_0^\infty |H_{eq}(f)|^2 df \quad (19)$$

is the noise equivalent bandwidth of the equalizer. Therefore, the total mean square noise voltage becomes

$$\begin{aligned}
\langle v_N^2 \rangle_0 &= 2 \frac{\eta q^2}{h\nu} \frac{1}{T_b} \int_{-T_b/2}^{T_b/2} E[P_0] dt \langle m^2 \rangle B_N R^2 A^2 + \frac{4k_B T}{R_b} B_N R^2 A^2 + S_I B_N R^2 A^2 + S_E B_e A^2 \text{ for data=0 and} \\
\langle v_N^2 \rangle_1 &= 2 \frac{\eta q^2}{h\nu} \frac{1}{T_b} \int_{-T_b/2}^{T_b/2} E[P_1] dt \langle m^2 \rangle B_N R^2 A^2 + \frac{4k_B T}{R_b} B_N R^2 A^2 + S_I B_N R^2 A^2 + S_E B_e A^2 \text{ for data=1.} \quad (20)
\end{aligned}$$

2.3 Bit error rate analysis

2.3.1 Shot noise

Our task now is to find the bit error rate caused by each noise component. From Eq. (8), if we assume ideal conditions for the bias circuit and the equalizer, the average output voltage during the time interval T_b can be calculated from Eq. (6). Thus

$$\begin{aligned}
\langle v_{out} \rangle_0 &= AR_0 M \frac{1}{T_b} \int_{-T_b/2}^{T_b/2} E[P_0] dt && \text{for data=0, and} \\
\langle v_{out} \rangle_1 &= AR_0 M \frac{1}{T_b} \int_{-T_b/2}^{T_b/2} E[P_1] dt && \text{for data=1.} \quad (21)
\end{aligned}$$

Also, the variances of the shot noise components can be calculated from the first terms of Eq. (20). Thus

$$\begin{aligned}
\sigma_0^2 &= 2 \frac{\eta q^2}{h\nu} \frac{1}{T_b} \int_{-T_b/2}^{T_b/2} E[P_0] dt \langle m^2 \rangle B_N R^2 A^2 && \text{for data=0, and} \\
\sigma_1^2 &= 2 \frac{\eta q^2}{h\nu} \frac{1}{T_b} \int_{-T_b/2}^{T_b/2} E[P_1] dt \langle m^2 \rangle B_N R^2 A^2 && \text{for data=1.} \quad (22)
\end{aligned}$$

Although the shot noise has a Poisson distribution, the inaccuracy resulting from use of a Gaussian approximation is small¹³. If we assume that the voltage at the equalizer output is Gaussian distributed, and if the decision threshold voltage v_{th} is set so that there is an equal error probability for 0 and 1 pulses and if we assume that the 0 and 1 pulses are equally distributed, then the error probability P_e is given by

$$P_e = \frac{1}{\sqrt{2\pi}\sigma_0} \int_{v_{th}}^{\infty} \exp\left[-\frac{(v - \langle v_{out} \rangle_0)^2}{2\sigma_0^2}\right] dv = \frac{1}{\sqrt{2\pi}\sigma_1} \int_{-\infty}^{v_{th}} \exp\left[-\frac{(-v + \langle v_{out} \rangle_1)^2}{2\sigma_1^2}\right] dv. \quad (23)$$

The error probability contribution from the shot noise is determined by several parameters. Most of the parameters such as amplifier gain, photodiode responsivity, noise equivalent bandwidth, etc., are determined by the receiver configuration. Therefore, when we choose a specific optical receiver, we can determine those parameters which are related with the optical receiver. The parameter which is related to the photon echo process is the average power at the input of the optical detector and it is determined by the system bandwidth, echo efficiency, and atom population fluctuations. Therefore, if we can analyze the relationship between those parameters and the average power, then we can estimate the effect of these parameters on the error probability. Fig. 4 shows the relationship between system bandwidth and average power integrated over the pulse interval for the data "0" and data "1" cases.

From Fig. 4, we see that the integrated average power for data "0" is increased with write/read pulses bandwidth decrease, whereas the integrated average power for data "1" is decreased with a write/read pulses bandwidth decrease. This means that the mean and variance for data "0" will increase but the mean and variance for data "1" will decrease with a decreasing system bandwidth. When we consider the distribution for both data components, the two distributions will become closer and the distribution of data "0" will become wider when write/read pulse bandwidth decreases. Only the distribution for data "1" will become narrower. Therefore, we can expect the error probability to increase when the write/read pulses bandwidth decreases. Also, from Eq. (6) the average powers for both data components have a common term which is related to atom population fluctuations. Therefore, we can say that when the atom population fluctuations become larger, the means and variances for both data components will increase, so we can expect that the error probability will also increase. Fig. 5 shows the error probability variations for several cases of bandwidth, echo efficiency, and atom fluctuations. In general, the bit error rate increases with decreasing bandwidth, decreasing efficiency and increasing atom population fluctuations.

2.3.2 Thermal noise

When we assume that the thermal noise is dominant at the output, the total thermal noise can be calculated from three thermal noise components which are the second, third, and fourth terms of Eq. (20) for each data case. The thermal noise component is the same for data "0" and data "1", compared to the shot noise component which is different for data "0" and data "1". We know that the thermal noise is Gaussian distributed with mean=0, so if we denote the variance of each thermal noise term as σ_{th1} for the first thermal noise, σ_{th2} for the second thermal noise, and σ_{th3} for the third thermal noise, then the total thermal noise is also Gaussian distributed and the mean and variance of the output data are

$$\begin{aligned}\langle v_{out} \rangle_0 &= AR_0 M \frac{1}{T_b} \int_{-T_b/2}^{T_b/2} E[P_0] dt && \text{for data=0,} \\ \langle v_{out} \rangle_1 &= AR_0 M \frac{1}{T_b} \int_{-T_b/2}^{T_b/2} E[P_1] dt && \text{for data=1, and} \\ \sigma_{tot}^2 &= \sigma_{th1}^2 + \sigma_{th2}^2 + \sigma_{th3}^2 && \text{for data=0 and data=1.}\end{aligned}\quad (24)$$

If the decision threshold voltage v_{th} is set so that there is an equal error probability for 0 and 1 pulses and if we assume that the 0 and 1 pulses are equally likely, then the error probability P_e is given by

$$P_e = \frac{1}{\sqrt{2\pi}\sigma_{tot}} \int_{v_{th}}^{\infty} \exp\left[-\frac{(v - \langle v_{out} \rangle_0)^2}{2\sigma_{tot}^2}\right] dv = \frac{1}{\sqrt{2\pi}\sigma_{tot}} \int_{-\infty}^{v_{th}} \exp\left[-\frac{(-v + \langle v_{out} \rangle_1)^2}{2\sigma_{tot}^2}\right] dv. \quad (25)$$

Generally, when the photodiode is without internal avalanche gain, thermal noise from the detector load resistor and from the active elements in the amplifier tends to dominate¹⁴. As in the shot noise case, the mean of data "0" will increase but the mean of data "1" will decrease when the write/read pulses' bandwidth decreases. The variances of both data components are independent of the write/read pulses bandwidth. Therefore, we can expect that the error probability for thermal noise will increase as write/read pulses bandwidth decreases. However, we expect no effect on error probability from atom population fluctuations because the distance between the means of both data components is not changed and neither the variances are changed.

2.3.3 Total noise

The above analysis shows that the bit error rate for one of the two kinds of noise dominates the other kind of noise. When they are comparable, the bit error rate calculation needs to include both noise sources. From the shot noise analysis, we approximate the output distribution as Gaussian. Using this approximation and the same approach which we used in the thermal noise analysis, we can calculate the average value and the variance of each data components as

$$\begin{aligned}\langle v_{out} \rangle_0 &= AR_0 M \frac{1}{T_b} \int_{-T_b/2}^{T_b/2} E[P_0] dt && \text{for data=0,} \\ \langle v_{out} \rangle_1 &= AR_0 M \frac{1}{T_b} \int_{-T_b/2}^{T_b/2} E[P_1] dt && \text{for data=1,} \\ \sigma_0^2 &= 2q \frac{\eta q}{h\nu} \frac{1}{T_b} \int_{-T_b/2}^{T_b/2} E[P_0] dt \langle m^2 \rangle B_N R^2 A^2 + \sigma_{tot}^2 && \text{for data=0, and} \\ \sigma_1^2 &= 2q \frac{\eta q}{h\nu} \frac{1}{T_b} \int_{-T_b/2}^{T_b/2} E[P_1] dt \langle m^2 \rangle B_N R^2 A^2 + \sigma_{tot}^2 && \text{for data=1.}\end{aligned}\quad (26)$$

If the decision threshold voltage v_{th} is set so that there is an equal error probability for 0 and 1 pulses and if we assume that the 0 and 1 pulses are equally likely, then the error probability P_e is given by

$$P_e = \frac{1}{\sqrt{2\pi}\sigma_0} \int_{v_{th}}^{\infty} \exp\left[-\frac{(v - \langle v_{out} \rangle_0)^2}{2\sigma_0^2}\right] dv = \frac{1}{\sqrt{2\pi}\sigma_1} \int_{-\infty}^{v_{th}} \exp\left[-\frac{(-v + \langle v_{out} \rangle_1)^2}{2\sigma_1^2}\right] dv. \quad (27)$$

3. CONCLUSION

We derived the bit error rate expressions for the shot noise and thermal noise in the photon echo memory. We showed how the write/read pulses width, echo efficiencies, and atom population fluctuations are related to the error probability of the output signal. Actual bit error rates are also related to the detector circuit parameters, such as the responsivity of the photodetector, amplifier gain, gain of the photodetector, noise bandwidth, and resistor values. However, those parameters are actually related to the optical receiver, and many people have analyzed the relationship between those parameters and the bit error rate. That is why we only concentrated on the effects of system bandwidth, echo efficiency, and atom population fluctuations. As expected, the relationship between the system bandwidth(write/read pulses width) and the bit error rate shows that when the system bandwidth decreases, the bit error rate is increased. When the echo efficiency is increased, the bit error rate is decreased. When the atom population fluctuation is increased, the bit error rate is also increased, expected. The thermal noise analysis, however, shows that the error probability due to the thermal noise is not changed with changes in system bandwidth, echo efficiency, and atom population fluctuations. That is reasonable because the thermal noise is generated from the optical receiver circuit and is not directly related to the photon echo process.

4. ACKNOWLEDGMENTS

The authors gratefully acknowledge the support of this work by the Air Force Office of Scientific Research, USAF, under AFOSR Grant F49620-95-1-0140.

5. REFERENCES

1. T. W. Mossberg, "Time-domain frequency-selective optical data storage", Optics Letters, Vol.7, No. 2, 1982, 77-79.
2. W. E. Moerner, *Persistent Spectral Hole-Burning: Science and Applications*, Springer-Verlag, 1988.
3. Y. S. Bai, and R. Kachru, "Coherent time-domain data storage with a spread spectrum generated by random biphase shifting", Optics Letters, Vol.18, No. 14, 1993, 1189-1191.
4. X. A. Shen, R. Hartman, and R. Kachru, "Impulse-equivalent time-domain optical memory", Optics Letters, Vol.21, No. 11, 1996, 833-835.
5. W. E. Moerner and T. P. Carter, "Statistical fine structure of inhomogeneously broadened absorption lines", Physical Review Letters, Vol. 59, No. 23, 1987, pp.2705-2708.
6. J. Y. Choi, *Noise Modeling of a Photon Echo Memory* (Ph. D. dissertation, Electrical Engineering Dept. Texas Tech University, 1997)
7. Peyton Z. Peebles, Jr., *Probability, Random Variables, and Random Signal Principles*, 2nd ed., McGraw-Hill, New York, 1987.
8. J. G. Proakis, *Digital Communications*, 2nd ed., McGraw-Hill, New York, 1989.
9. S. D. Personick, "Receiver design for digital fiber optic communication systems", Bell Sys. Tech. J., Vol. 52, pp.843-886, July-Aug. 1973.
10. D. R. Smith and I. Garrett, "A simplified approach to digital optical receiver design", Opt. Quantum Electron., Vol. 10, pp.211-221, 1978.
11. H. Taub and D. L. Schilling, *Principles of Communication Systems*, 2nd ed., McGraw-Hill, New York, 1986.
12. A. B. Carlson, *Communication Systems*, 3rd ed., McGraw-Hill, New York, 1986.
13. P. Balaban, "Statistical evaluation of the bit error rate of the fiberguide repeater using importance sampling", Bell Sys. Tech. J., Vol. 55, pp. 745-766, July-Aug. 1976.
14. John M. Senior, *Optical Fiber Communications*, 2nd ed., Prentice Hall, New York, 1992.

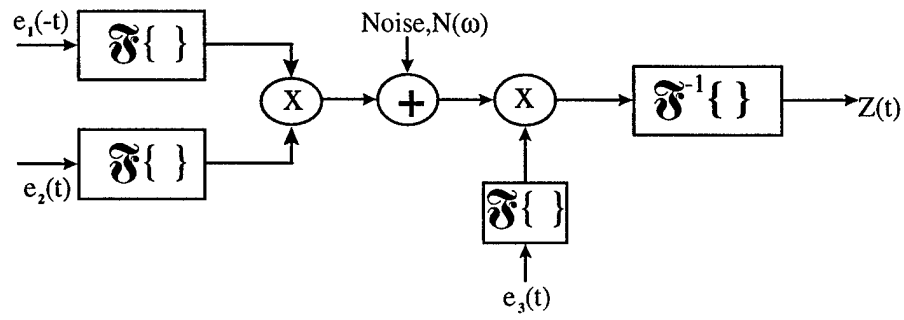


Fig. 1 The photon echo process including the noise source from the atom fluctuation

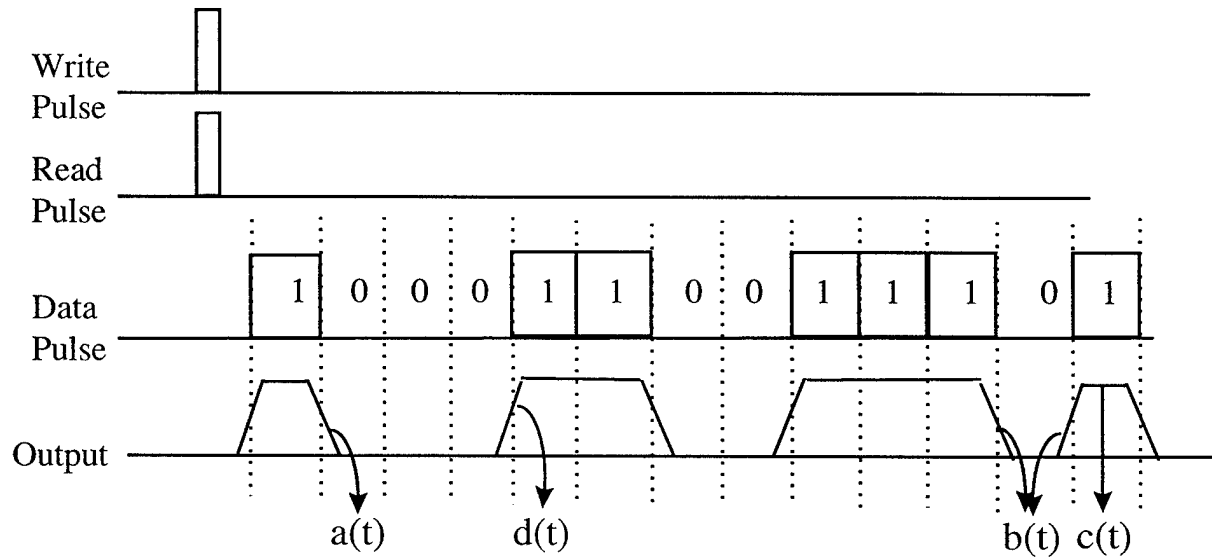


Fig. 2 The effects of convolution and correlation of the write/read pulses on the data signal

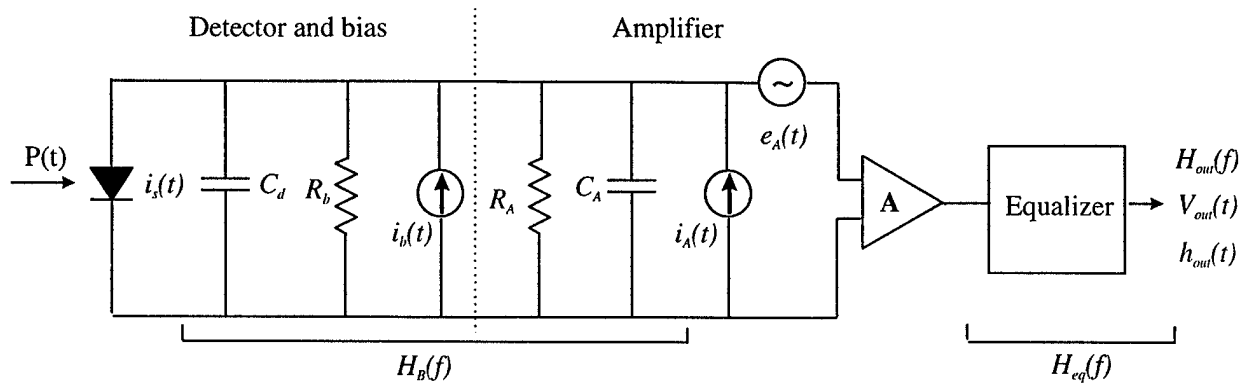
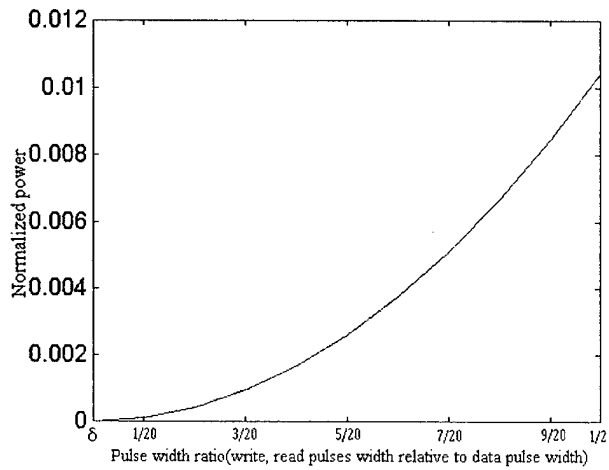
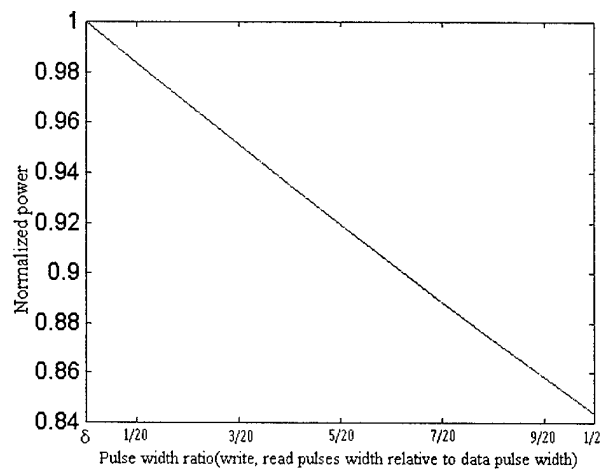


Fig. 3 Schematic diagram of a typical optical receiver



(a)



(b)

Fig. 4 The relationship between system bandwidth and average power integrated over the data pulse interval (a) shows the power increase for data "0" with system bandwidth decrease(write/read pulses width increase) (b) shows the power decrease for data "1" with system bandwidth decrease(write/read pulses width increase).

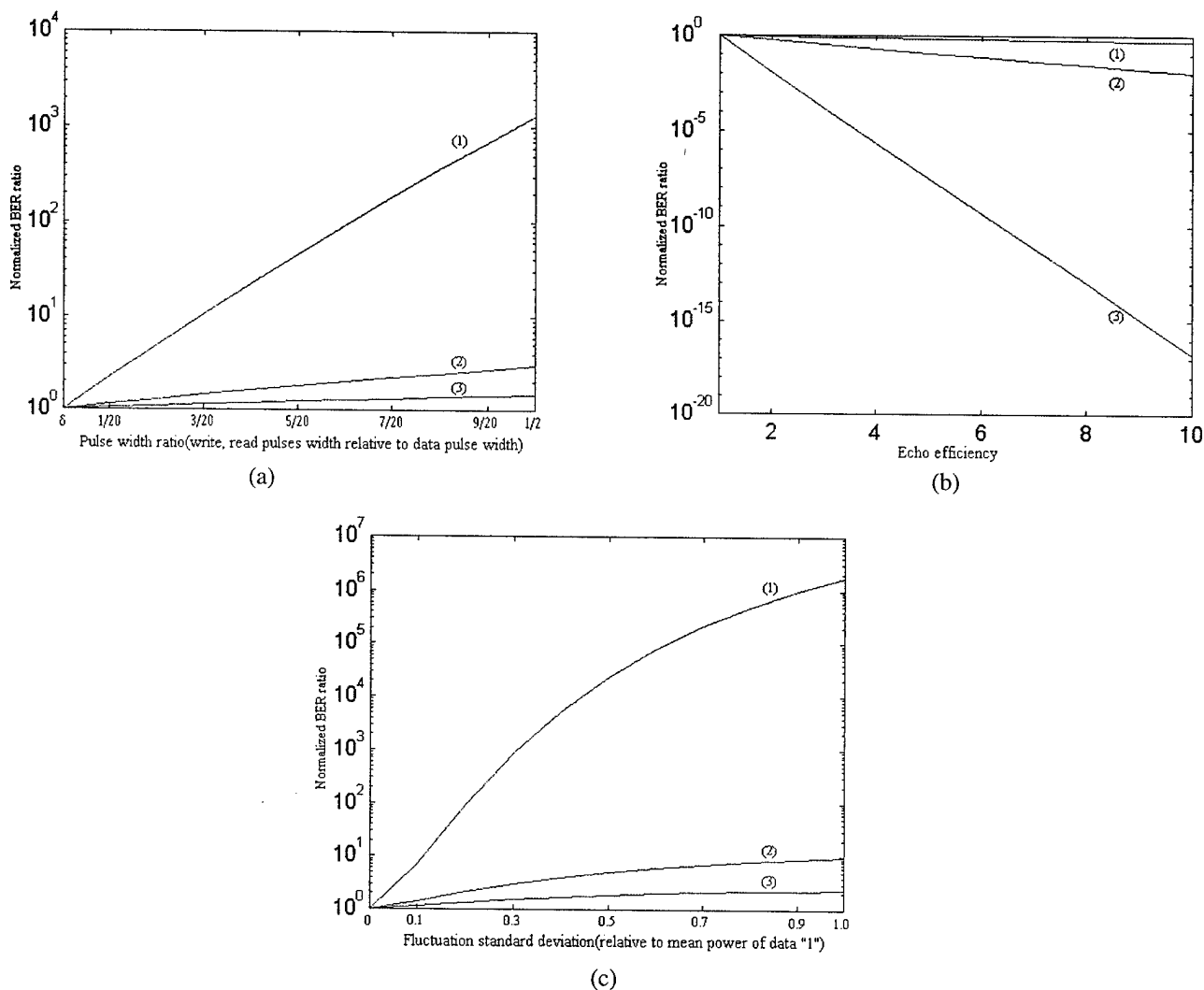


Fig. 5 The bit error rate variations with bandwidth, echo efficiency, and atom population fluctuations. (a) shows the BER change when we increase the write/read pulses width. (1) is for $\langle v_{out} \rangle_0 \gg \sigma_0^2$, and $\langle v_{out} \rangle_1 \gg \sigma_1^2$, (2) is for $\langle v_{out} \rangle_0 \approx \sigma_0^2$, and $\langle v_{out} \rangle_1 \approx \sigma_1^2$, (3) is for $\langle v_{out} \rangle_0 \ll \sigma_0^2$, and $\langle v_{out} \rangle_1 \ll \sigma_1^2$. (b) shows the BER changes with an echo efficiency increase. (1) is for $\langle v_{out} \rangle_0 \ll \sigma_0^2$, and $\langle v_{out} \rangle_1 \ll \sigma_1^2$, (2) is for $\langle v_{out} \rangle_0 \approx \sigma_0^2$, and $\langle v_{out} \rangle_1 \approx \sigma_1^2$, (3) is for $\langle v_{out} \rangle_0 \gg \sigma_0^2$, and $\langle v_{out} \rangle_1 \gg \sigma_1^2$. (c) shows the BER change with atom population increase. (1) is for $\langle v_{out} \rangle_0 \gg \sigma_0^2$, and $\langle v_{out} \rangle_1 \gg \sigma_1^2$, (2) is for $\langle v_{out} \rangle_0 \approx \sigma_0^2$, and $\langle v_{out} \rangle_1 \approx \sigma_1^2$, (3) is for $\langle v_{out} \rangle_0 \ll \sigma_0^2$, and $\langle v_{out} \rangle_1 \ll \sigma_1^2$.

M-type thick holograms in bacteriorhodopsin films with a high-divergence reference beam

Arkady S. Bablumian, Thomas F. Krile, David J. Mehrl, and John F. Walkup

The capacity to use differing read and write wavelengths for reconstructing volume holograms recorded in a shift-multiplexing geometry is analyzed and realized for M-type volume holograms recorded on bacteriorhodopsin films. The intensity distribution in the reconstructed wave is calculated as a function of the parameters of the recording and readout beams. Optimal recording and retrieving geometries, as well as a precise method for tuning the readout setup, are suggested. © 1998 Optical Society of America

OCIS codes: 090.0090, 090.7330.

1. Introduction

High-capacity storage of optical information can be achieved by holographic recording throughout the volume of a thick medium.¹ The strong sensitivity of thick holograms to the parameters of the reconstruction beam allows one to multiplex many holograms in the same volume and then read them out selectively. The simplest way to retrieve any desired hologram is to use a readout beam identical in all respects to the reference beam used for recording. At the same time, for nondestructive retrieval of stored holograms it is necessary either to fix them or to reconstruct them at wavelengths to which the material is insensitive. (The latter is of particular interest in the general area of real-time optical data processing.) In general, changing the readout wavelength will change not only the output's orientation (in accordance with the Bragg condition) but also the shape of the wave front. This leads to both a loss of information in the object beam and difficulties associated with the synthesis of a readout beam with a complicated wave-front shape.

Hologram reconstruction with different wavelengths that employs distortion compensation during reconstruction by means of changing the curvature of the readout wave front was described in Ref. 2. In the paraxial approximation using the coupled-wave

theory, the authors calculated the optimal parameters for the readout beam (focal length) and assessed the width of the reconstructed spherical beam. Unfortunately, under the approximations used in Ref. 2 this approach cannot be applied for analyzing several interesting hologram-multiplexing geometries for situations in which recording beams are highly divergent spherical waves. Such a geometry was investigated in Ref. 3, which described a hologram of an information-bearing signal considered to be a superposition of plane-wave elemental holograms with the same spherical reference beam. The plane-wave object beam of each elemental hologram represented a single component of the signal. This approach allowed the authors to calculate the optimal parameters of the reconstructing beam—a shift parameter characterizing hologram selectivity—and an assessment of maximal resolution in the reconstructed image.

In this paper we apply another approach in which we consider the relative change of the intensity distribution in the frequency plane of the signal. For an arbitrary wavelength we calculate the reconstruction of the points of the Fourier transform of a signal by considering the hologram as a superposition of elemental holograms, each being formed by two point sources. We show that, besides the parameters mentioned above, such an approach allows one to assess distributions of both relative intensity and resolution along the reconstructed image. These parameters are then compared with values derived experimentally.

It is necessary to note that the readout beam has to be calculated and oriented with respect to the hologram with high accuracy, according to the shift se-

The authors are with the Department of Electrical Engineering, Texas Tech University, Lubbock, Texas 79409.

Received 9 May 1997; revised manuscript received 7 October 1997.

0003-6935/98/081350-06\$10.00/0

© 1998 Optical Society of America

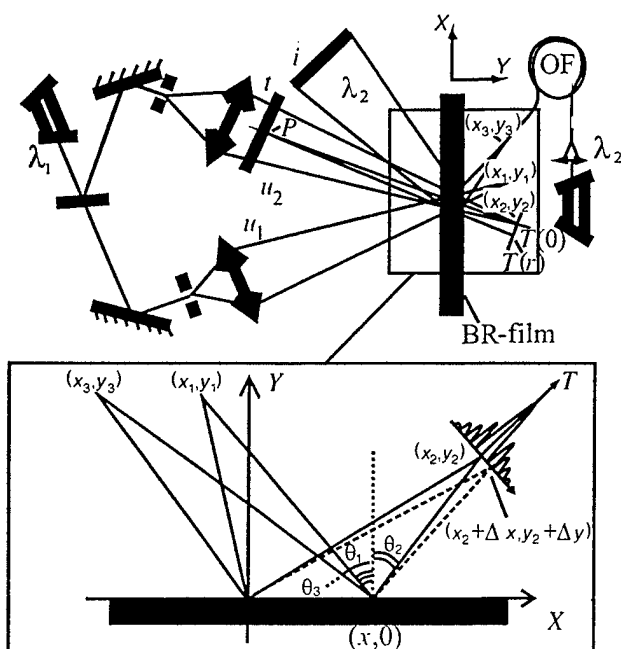


Fig. 1. Geometry of the recording and readout rays. Here t and T denote the transparency and its scaled Fourier transform, respectively, i represents the reconstructed image, and OF denotes the optical fiber.

lectivity of a chosen setup.³ Since the orientation has three degrees of freedom and recording beams have to be measured with the above-mentioned accuracy, it becomes clear that the results cannot be applied easily without some practical method of finding the optimal location of the readout beam. So our next step was to develop a method for tuning the readout setup. Finally, experimental verification of the theory is demonstrated by use of M-type holograms in bacteriorhodopsin (BR) films.

2. Theory

Let the hologram be recorded by the reference u_1 and object u_2 waves, as shown in Fig. 1. In both recording arms the laser beams are expanded and then point focused. This allows both the formation of a spherical reference beam and the insertion of the information into the object arm by use of a transparency with transmittance t . The scaled Fourier transform of t is produced at the plane of the beam focus $[(x_2, y_2)$ in Fig. 1]. Here we let (x_1, y_1) designate the coordinates of the spherical reference source and (x_2, y_2) designate the coordinates of the zeroth-order component of the Fourier spectrum of transparency t .

The hologram of transparency t can itself be regarded as the superposition of an array of elemental holograms, each being formed by a pair of spherical beams whose sources are located at the point (x_1, y_1) and one of the points of the Fourier plane $[(x_2 + \Delta x, y_2 + \Delta y)$ in Fig. 1]. The hologram of the zeroth-order component of the Fourier spectrum T [$H(\Delta x, \Delta y) = H(0, 0)$] will determine the background in the reconstructed image I , whereas the holograms of higher-

order components $[H(\Delta x, \Delta y)]$ will determine its resolution. It is evident that each elemental hologram can be reconstructed by the beam whose parameters coincide with those of one of the recording beams. The existence of reconstructed beams whose wavelengths differ from the recording wavelength becomes clear from the following: Each elemental hologram is recorded by point-source beams; therefore any of its small parts is described by the constant grating vector K . This means that, for an arbitrary wavelength λ in every point (x, y) of the elemental hologram, two rays (incident and diffracted) oriented at the Bragg angle to the grating vector K are determined unambiguously. The lattice of rays combines to form only two beams that can be diffracted by this hologram and that, generally speaking, for an arbitrary wavelength λ are not spherical.

Let us consider hologram reconstruction by a spherical wave u_3 with coordinates (x_3, y_3) and determine the Bragg mismatch angle δ for its rays at every point of their crossing within the hologram. Let us also consider the cone of rays emanating from (x_3, y_3) with an average spatial frequency β_k . The angular aperture of this cone of rays we choose is small enough to consider it to be a plane wave. Our purpose is to define the conditions under which (1) the intensity change along the cone in hologram H is equivalent to (2) the intensity change of a plane wave incident on a plane diffraction grating. Such an analogy will allow us to assess the diffraction in the case 1 by calculation of the diffraction in case 2 in accordance with the coupled-wave theory.⁴ Under suitable approximations, described below, the intensity of the plane wave in the output plane of the equivalent diffraction grating will be equal to the output intensity of the cone of rays. Continuing this procedure for all β_k , we can calculate the output intensity arising from the source u_3 . Then one can calculate the intensity distribution of the diffracted beam for each elemental hologram H , considering the sum of the incident and diffracted beams to be constant. The sum of the elemental holograms corresponds to the Fourier spectrum of the transparency T , by which we can estimate the resolution in the reconstructed beam.

First, let us consider the main arguments supporting the proposed approximation, as well as the limits of its applicability. The diffraction process is determined mostly by the direct energy diverted from the incident into the diffracted beam when the values of the diffraction efficiency (DE) are low (typically the case for BR). It follows from the fact that the amplitude change of the incident wave is proportional to the amplitude of the diffracted wave, and vice versa, that the amplitude change of the diffracted wave is proportional to the amplitude of the incident wave.⁴ Therefore the diverted energy proceeds mainly in one direction when the difference between the amplitudes of the interacting waves is large. Let us neglect the influence of the parameters of the diffracted beam on the intensity change of the incident beam. This assumption and the fact that the incident rays

from u_3 intersect one and only one conical region of the hologram allow one to consider the diffraction in such conical regions independently of each other. It means that the diffraction of the beam u_3 within a region determined by β_k will not be changed after the arbitrary changing of the hologram's structure, as well as the shape of the beam u_3 outside the region. In particular, diffraction by hologram H within a region will be equivalent to the diffraction of the plane wave with spatial frequency β_k on a hologram whose grating vector K varies as a function of y in the same manner as that in the given region of hologram H and is independent of x .

Let us now break this new holographic structure into parallel layers $y_{k-1} < y < y_k$. We choose the thickness of each layer to be thin enough to consider $K(y)$ to be constant within the layer. In this case the intensity change of the incident plane wave within each layer can be calculated in accordance with the coupled-wave theory. We can see from Eq. (2.5) below that the equation describing the diffraction depends on only the Bragg mismatch angle δ if we use a first-order Taylor approximation for δ and K . It means that changing the value of K in any layer without changing δ does not change the intensity of the incident beam in the output plane of the hologram. This, in turn, means that the grating vector K can be chosen to have the same value for all layers with the condition that δ is constant. Thus, assuming δ is not changed along the propagation path of the cone of rays constituting u_3 , we can calculate the output intensity by calculating the diffraction of the plane wave on the equivalent diffraction grating. The spatial frequency of the plane wave and the absolute value of the grating vector K have to be chosen to be equal to β_k and $K(x, 0)$, respectively.

As indicated in Fig. 1, rays from the recording (x_1, y_1) , (x_2, y_2) and reconstructing (x_3, y_3) sources traveling to an arbitrary point $(x, 0)$ on the recording medium make an angle θ_i , where

$$\theta_i(x, y) = \arctan\left(\frac{x_i - x}{y_i - y}\right), \quad i = 1, 2, 3. \quad (2.1)$$

The Bragg angle at the same point is

$$\theta_{\text{Bragg}}(x, y) = \arcsin\left\{\frac{\lambda_1}{\lambda_2} \sin\left[\frac{\theta_1(x, y) - \theta_2(x, y)}{2}\right] + \frac{\theta_1(x, y) + \theta_2(x, y)}{2}\right\}, \quad (2.2)$$

which follows directly from the Bragg law written in common form² for readout λ_2 and recording λ_1 wavelengths. Consequently, the Bragg mismatch angle δ_{Bragg} is

$$\delta_{\text{Bragg}}(x, y) = \theta_{\text{Bragg}}(x, y) - \theta_3(x, y). \quad (2.3)$$

We choose the coordinates of the point-source reconstruction beam (x_3, y_3) in such a way that two of its rays crossing the hologram at input $(0, 0)$ and $(c, 0)$ make Bragg angles with the input plane [Eq.

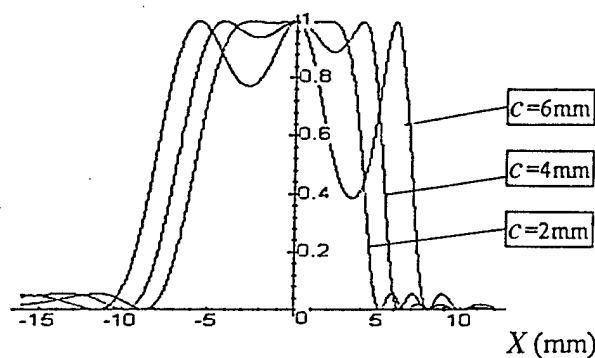


Fig. 2. Normalized DE of $H(0, 0)$ versus the hologram plane position for various values of the parameter c .

(2.2)]. Using geometric construction we can show that

$$y_3 = c \frac{\cos[\theta_{\text{Bragg}}(0, 0)] \cos[\theta_{\text{Bragg}}(c, 0)]}{\sin[\theta_{\text{Bragg}}(0, 0)] - \theta_{\text{Bragg}}(c, 0)],$$

$$x_3 = y_3 \tan[\theta_{\text{Bragg}}(0, 0)]. \quad (2.4)$$

We then determine the mismatch angle δ_{Bragg} for the rest of the rays of the reconstructed beam and insert it into the relation that expresses the angular sensitivity of a thick hologram:

$$\eta = \left| \exp\left[-\frac{\alpha d}{c_s}\right] \times \exp[-i\xi] \frac{\exp[i(\xi^2 + \nu^2)^{0.5}] - \exp[-i(\xi^2 + \nu^2)^{0.5}]}{2\left(1 + \frac{\xi^2}{\nu^2}\right)^{0.5}} \right|^2, \quad (2.5)$$

where $\xi = (2\pi n/\lambda_2)\delta_{\text{Bragg}} d \sin[(\theta_1 - \theta_2)/2]$, with $\nu = \chi d/c_s$, $c_s = \cos[(\theta_1 - \theta_2)/2]$, d is the thickness of the hologram, and χ is the coupling constant.⁴

Expression (2.5) describes, in the exit plane of the hologram, the profile of the intensity of the diffracted wave that attains its maximum at points $x = 0$ and $x = c$. Note that we are interested in the relative DE of diffracted rays versus only δ_{Bragg} for each of them, so we can simplify Eq. (2.5) to obtain

$$\frac{\eta}{\eta_0} = \nu^2 \text{sinc}^2\{\pi^{-1}[\nu^2 + k\delta_{\text{Bragg}}^2(x, y)]^{0.5}\}. \quad (2.6)$$

Here we took into account the fact that the presence of loss has very little influence on the angular sensitivity⁴ and used Eq. (2.5) as written for lossless gratings with real χ . The constant ν was measured experimentally.

Figure 2 represents the relative-intensity distribution profile (equivalent to the normalized DE) of diffracted beams in the exit plane of the hologram calculated for the elemental hologram $H(0, 0)$ (corresponding to the zeroth-order component of the Fou-

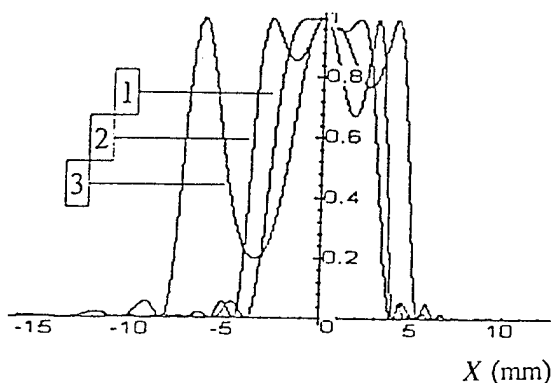


Fig. 3. Normalized DE for cases $(x_1, y_1) = (7, 10)$, $(x_2, y_2) = (6.5, 10)$ (plot 1), $(8, 10)$ (plot 2), $(5, 10)$ (plot 3).

rier spectrum T of transparency t) for reconstructed beams with different values of the parameter c . Values of $\lambda_1 = 458$ nm and $\lambda_2 = 633$ nm were used for this and subsequent plots. The X axis is in the hologram recording plane, and the different values of c are obtained by the changing of the location of the reconstruction point source (x_3, y_3) . Optimized readout parameters correspond to the portion of the hologram where the curves of Fig. 2 have sufficient DE, say not less than $1/e$ (as for the definition of the width of a Gaussian-shaped signal), and are as flat as possible. In our experiments (Section 3) the hologram was approximately 3 mm in extent, so $c = 2$ mm would be optimal from Fig. 2.

Profiles of diffracted beams with the optimized parameter c , calculated for several recording setups of $H(0, 0)$ holograms (with different orientations and average spatial frequencies of their recording beams), are shown in Fig. 3. The diffraction of the beam optimized for the reconstruction of hologram $H(0, 0)$ from holograms $H(\Delta x, \Delta y)$, which correspond to the higher-order components of the Fourier spectrum T , is shown in Fig. 4. These plots represent the sum intensity distribution of beams diffracted by elemental holograms $H(\Delta x, \Delta y)$ and $H(-\Delta x, -\Delta y)$, where we use the fact that symmetric components of the Fourier spectrum contain the same information. From Fig. 4 we can see that the relative DE decreases with increasing values of r , corresponding to holograms of higher components of the Fourier spectrum T . Thus the reconstruction system acts like a low-pass filter,

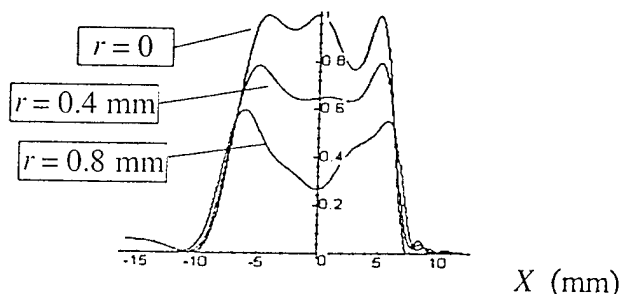


Fig. 4. Normalized DE of elemental holograms with various values of r versus the hologram plane position.

and one can use this curve to define an effective spatial cutoff frequency at some particular value of the relative DE ($1/e$ in this paper).

Let us now consider in more detail how the intensity profiles of beams diffracted by elemental holograms (Figs. 2–4) can be utilized to determine the resolution and intensity distribution in the reconstructed image t . Each point P of the recording transparency t is formed by a cone of rays connecting it with points of the Fourier spectrum (Fig. 1), each of which we took as an elementary point-source object beam of the elemental hologram. The part of the transparency t in the vicinity of the point P will be reconstructed with a resolution h if all rays of a cone with a base radius of

$$r = \frac{0.61\lambda_1 D}{h} \quad (2.7)$$

have enough DE ($\eta > \eta_0/e$), where $r = (\Delta x^2 + \Delta y^2)^{0.5}$ is one of the coordinates of the Fourier plane of the transparency t and D is the distance between the plane of transparency t and its Fourier transform plane T .⁵ If the behavior of the plots in Fig. 4 is taken into account, the proper DE of only edge cone rays corresponding to the maximum-order components of the Fourier spectrum will provide the required resolution. Then it is easy to see that the intensity distribution of the reconstructed beam at the image plane corresponds to a profile of the beam diffracted by the $H(0, 0)$ hologram at its exit plane, reduced in size by $D_2 \cos \theta_{\text{aver}}/D_1$, where D_1 and D_2 are the distances between the Fourier plane of image i and, accordingly, the hologram and the plane of the image, respectively, and θ_{aver} is the average incident angle of the reconstructing beam. Thus the intensity and resolution in an arbitrary part of the reconstructed image T can be estimated by the profiles of two beams diffracted by elemental holograms $H(0, 0)$ and $H(\Delta x, \Delta y)$, where Δx and Δy obey the condition of Eq. (2.7).

Let us also consider the limits that the assumptions defined above place on the thickness of the hologram (more exactly, on the Klein parameter Q , which characterizes thick gratings⁵ for which the theory is valid). Calculations [Eqs. (2.1)–(2.6)] showed that, for a thickness of approximately 0.5 mm and values of the Q factor of the order of 10^4 , the values of δ variations along the propagation path of the reconstructing beam do not exceed 10^{-4} rad, which corresponds to a percent error in the intensity calculation of not more than 5%–7%.

3. Experimental Results

To investigate the different wavelength regimes of recording and reconstructing volume holograms we used a thick BR film. This material exhibits excellent properties for real-time optical processing applications, as well as for permanent high-density data storage.⁶ Hologram recording in BR films was carried out in the M-type regime, in which red readout light provided at the same time excitation for the BR

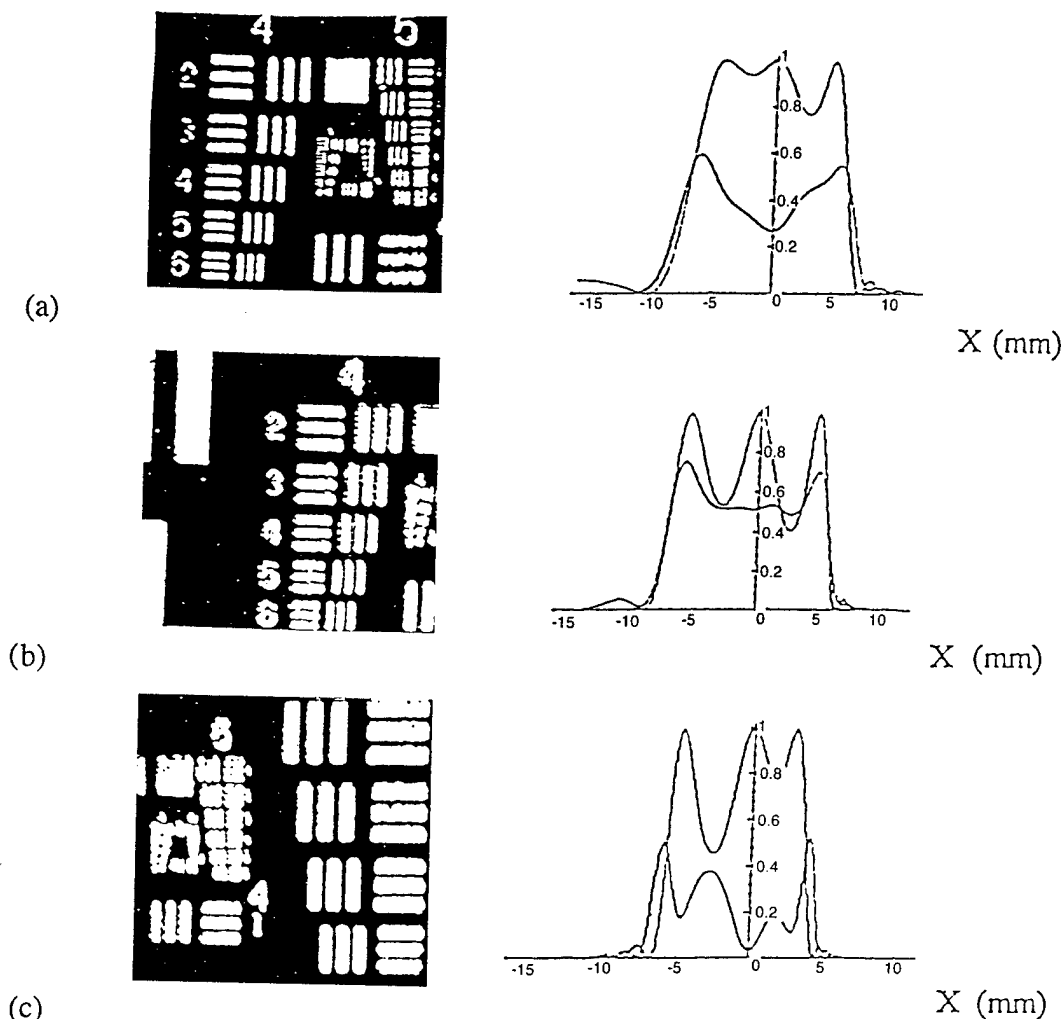


Fig. 5. Photographs of transparency t from hologram H and the corresponding plots of reconstructed beams from two elemental holograms, $H(r = 0)$ (upper traces) and $H(r = 1 \text{ mm})$ (lower traces), in the exit plane of hologram H for (a) $Q = 100$, (b) $Q = 300$, and (c) $Q = 750$.

molecules, transforming them into the M-state ready for recording with blue light. Using M-type holograms allowed us to investigate the two-lambda method³ of constructing the holographic memory and, simultaneously, to change and compare in real-time the recording and readout parameters.

Mutant variant BR_{D96N} films with a thickness of 100 μm were used. A hologram of a standard U.S. Air Force test pattern was recorded at $\lambda = 458 \text{ nm}$ and reconstructed at $\lambda = 633 \text{ nm}$. The setup geometry for recording and reconstruction was chosen according to the theory described in Section 2, enabling us to compare the experimental results with the results derived theoretically (see Figs. 2–4).

As was pointed out above, in a recording regime with a high sensitivity to shift the process of finding the location of the readout beam with the given parameters becomes a difficult problem practically. This is particularly true for high values of the Klein parameter Q . For optimally tuning the readout setup the following method was suggested and utilized: The thick recording medium was first re-

placed by a structure consisting of two separated thin films. A hologram recorded in such a structure, in contrast to a common thick hologram, can be reconstructed by readout beams of any orientation. This forms two images that are propagated, in general, in different directions. On optimal orientation of the readout beam these directions coincide, and interferometric fringes of overlapped images coalesce into one fringe. From the maximal size of this fringe one can judge the accuracy of the reconstruction source location.

For modeling the volume medium a 1-mm glass plate with photoresist layers on both surfaces was used. The readout beam was formed by use of a piece of optical fiber to facilitate precise positioning of the point source. After finding the optimal position for the reconstruction source, we then replace the model medium with the BR film. We also devised a technique (not discussed here for the sake of brevity) to compensate for the fact that the overall thickness of the model medium and the BR film are not the same.

Figure 5 presents photographs of the U.S. Air Force test-pattern image reconstructed from the BR film with different values of the Q factor. For comparison, next to each photograph we show plots of the intensity profiles of beams diffracted from two elemental holograms, $H(0, 0)$ and $H(r = 1 \text{ mm})$, recorded in the corresponding geometry. As was pointed out above, a sufficient DE for these two elemental holograms automatically ensures a sufficient DE for all elemental holograms $H(|r| \leq 1 \text{ mm})$ (remember that r is the coordinate in the frequency domain). With the parameters of the beam u_2 taken into account, it is easy to calculate that the reconstruction of a 1-mm-extent u_2 in the frequency plane provides a 30- μm resolution in the reconstructed image [Eq. (2.7)]. As one can see, this resolution (the width of the first element in the fourth group of the test pattern), which conforms to the lower traces in Figs. 5(a)–5(c), is provided over all the field of the reconstructed image for $Q = 100, 300$ but is reduced for $Q = 750$. These results are supported by analysis of the corresponding photos. The experimental sensitivity of the setup with $Q = 750$ to the shift of the readout beam was approximately 20 μm , deviating by 5%–6% from the theoretical prediction. The measured DE of the reconstructed images was approximately 4%–5%.

4. Conclusions

We have demonstrated a relatively simple method of calculating critical parameters for the processes of reading and writing volume holograms using highly divergent beams of differing wavelengths. The experimental results were shown to agree with the theoretical results. We have considered the resolution and relative-intensity distribution of the reconstructed image stored in a thick hologram by a high-divergence reference beam that is arbitrarily oriented relative to the object beam. These param-

eters, as well as the optimal parameters of the readout beam, can be estimated from the intensity profiles of beams diffracted by two elemental holograms (recorded by a pair of spherical beams), whose simple calculation method has been presented above.

A method for modeling a volume hologram by use of a medium consisting of two separated thin layers has also been suggested. This approach allows one to find experimentally the precise optimal position of the readout beam. Also, the method makes accessible the modeling and direct visualization of the process of diffraction by thick holograms with arbitrary recording parameters. These procedures could be difficult or impossible as a result of the characteristics of commonly used volume recording media (e.g., short lifetimes, low DE, destructive readout, etc.).

We thank Bend Research, Inc., for BR-film preparation. This study was supported by the NASA Ames Research Center, whose support is sincerely appreciated.

References

1. G. Barbastathis, M. Levene, and D. Psaltis, "Shift multiplexing with a spherical reference beam," *Appl. Opt.* **35**, 2403–2417 (1996).
2. H. C. Kulich, "Reconstructing volume holograms without image field losses," *Appl. Opt.* **30**, 2850–2857 (1991).
3. G. Barbastathis and D. Psaltis, "Shift multiplexed holographic memory using the two-lambda method," *Opt. Lett.* **21**, 4432–4434 (1996).
4. H. Kogelnik, "Coupled wave theory for thick hologram gratings," *Bell. Syst. Tech. J.* **48**, 2909–2947 (1969).
5. R. J. Collier, C. B. Burckhardt, and L. H. Lin, *Optical Holography* (Academic, New York, 1971), p. 271.
6. D. T. Smithey, W. C. Babcock, and J. Millerd, "Holographic data storage using thick bacteriorhodopsin recording materials," in *International Symposium on Optical Memory and Optical Data Storage*, Vol. 12 of OSA Technical Digest Series (Optical Society of America, Washington, D.C., 1996), pp. 407–409.